Source: Electronic Materials and Processes Handbook

Chapter

3

Ceramics and Glasses

Alex E. Bailey
Northrop Grumman
Linthicum, Maryland

3.1 Introduction

Ceramics and glasses are among the enabling technologies in nearly all electronics markets. Electronic data transmission with low signal attenuation is quite common using low-permittivity ceramics or glass matrix media in digital or analog modes throughout the radio and microwave frequency ranges. High-quality glass fibers have enabled high-volume data transmission at optical frequencies over long distances with minimal distortion of the original signal. Today, most long-distance telecommunication occurs through optical fibers in which data is transmitted via light through a glass fiber rather than electrons through a metal wire.

High-permittivity, electrically insulating ceramics are the necessary ingredient for the largest market segment of energy-storing capacitors. High-permittivity ceramics, which undergo a lattice distortion with applied field or output an electrical signal when stressed, are under active element for sonar technology and sonic imaging in medical applications. The development of processing techniques to form optically transparent, high-permittivity ceramics whose index of refraction can be modified by an applied electric field allows the creation of devices that are capable of modulating optical signals.

Applications for ferrite ceramics have expanded with the rapid growth of the electronics industry, and they include inductors, transformers, permanent magnets, magneto-optical devices, electromechanical devices, and microwave electronics devices. Superconducting ceramics, which allow conduction at virtually zero resistance, provide the opportunity to eliminate energy dissipation in power lines and generation of large magnetic fields for unique medical applications and zero-friction magnetic levitation devices and transportation systems.

Downloaded from Digital Engineering Library @ McGraw-Hill (www.digitalengineeringlibrary.com)
Copyright © 2004 The McGraw-Hill Companies. All rights reserved.
Any use is subject to the Terms of Use as given at the website.

3.2 Ceramic Interconnections for Microelectronics

Ceramic interconnect technology offers significant benefits in terms of design flexibility, density, and reliability. These advantages, inherent in the ceramic materials themselves, often make this material the preferred alternative for high-density, high-reliability applications. Ceramic packaging can be categorized as thin film, thick film, or multilayer.

Table 3.1a shows a comparison of various ceramic substrate materials. If one were to design the ultimate substrate material, a thermal expansion matched to that of the semiconductor chips (3.5 ppm/°C for Si, 7.5 ppm/°C for GaAs) would be desirable to improve reliability, particularly as chip sizes continue to grow. Low dielectric loss is desirable, because it has a direct impact on the transmission losses of the thin or thick film circuits. Typically, high ther-

TABLE 3.1a Electrical and Thermal Properties of Various Electronic Materials

	Electrical resistivity (Ω-cm)	Thermal conductivity (W/m-K)
Conductors		
Copper	1.7×10^{-6}	395
Gold	2.3×10^{-6}	298
Molybdenum	5.2×10^{-6}	138
Tungsten	5.5×10^{-6}	174
Platinum	10.5×10^{-6}	72
Palladium	11×10^{-6}	72
Semiconductors (pure)		
Silicon	$>10^{2}$	118
Germanium	40	60
Silicon carbide (SiC)	10	270
Insulators		
Low-voltage porcelain	$10^{12} \times 10^{-14}$	2–4
SiO_2 glass	$>10^{14}$	2
Al_2O_3	$>10^{15}$	25
Soda-lime-silica glass	10^{5}	2–3
Aluminum nitride (AlN)	$>10^{15}$	230
Diamond	$>10^{15}$	2000

Downloaded from Digital Engineering Library @ McGraw-Hill (www.digitalengineeringlibrary.com)
Copyright © 2004 The McGraw-Hill Companies. All rights reserved.
Any use is subject to the Terms of Use as given at the website.

Ceramics and Glasses

mal conductivity is desired, particularly in power devices, to conduct heat away from the chips. Thermal management is a key element in the mechanical design of today's advanced electronics. The trend to high circuit densities within ICs and packaging leads to higher heat densities. Component failure rates increase exponentially as temperature is increased. High mechanical strength is desirable for mechanical stability and reliability. Low-density materials are typically desired for lightweight systems. The desired dielectric constant may vary, depending on the application. A lower dielectric constant generally allows closer spacing of signal lines and higher transmission speeds. In some devices, such as resonators or filters, higher dielectric constants result in reduced feature dimensions.

The speed of data transmission in semiconductor devices has been the focal point of development; however, the levels of packaging materials through which the signals must eventually pass have not kept pace, and packaging has become one of the limiting factor in the transmission speed of microelectronic devices. The transmission time delay is related to the dielectric constant of the packaging material by

$$\tau_d = K^{1/2}\, l/c \tag{3.1}$$

where l = length of the circuit
c = speed of light
K = dielectric constant of the transmission media

Therefore, it is desirable to design in low-dielectric constant media, such as that of the silicates. For instance, silica with a relative permittivity of ≈4 would yield a transmission delay about twice that of pure vacuum ($\varepsilon_r = 1$), whereas alumina with a relative permittivity of ≈10 would yield about three times the delay.

3.2.1 Thin film

Thin film metallization on ceramic substrates was developed to take advantage of high circuit density and tight dimensional tolerances of deposited and etched metals and the high thermal conduction and mechanical stability of ceramic substrates. Typically, the substrate used is high-purity alumina (99.5 to 99.6 percent), polished to a fine surface finish and good flatness. However, thin film circuitry has been used on a wide variety of ceramics, including glasses, multilayer ceramics, and magnetic ceramics, as a method of forming surface features with tight dimensional control and fine line resolution (≈0.5- to 1-mil lines and spaces). Standard grain size for the 99.5 percent alumina is about 2 to 2.5 μm, yielding a surface finish of <0.15 μm (<6 μin) The more expensive 99.6 percent alumina substrates are used in applications for very fine line depositions, because they are generally more defect free and have a finer surface finish. Thin film metallization is applied to a suitable substrate by a variety of deposition methods such as evaporation, sputtering, plating, and chemical vapor deposition (CVD). The metallization is generally deposited

Downloaded from Digital Engineering Library @ McGraw-Hill (www.digitalengineeringlibrary.com)
Copyright © 2004 The McGraw-Hill Companies. All rights reserved.
Any use is subject to the Terms of Use as given at the website.

over the entire substrate surface and then photoimaged and etched to produce the desired circuit pattern.

All of the desirable high-conductivity metallizations, Au, Cu, Ag, Al, can be deposited as thin films. Additionally, thin film resistors of materials such as tantalum nitride (TaN or Ta_2N) and nickel chrome (NiCr) are used. Materials such a silicon oxides or nitrides have been deposited to serve as passivation and capacitor dielectrics. The evaporation method is a vacuum deposition process whereby a source metal is heated to its vaporization temperature under high vacuum (10^{-5} to 10^{-6} torr). Figure 3.1 shows the schematic for a typical vacuum evaporator. Sputtering involves bombardment of a metal target with an ion plasma. The metal target is used as the cathode, and the substrate to

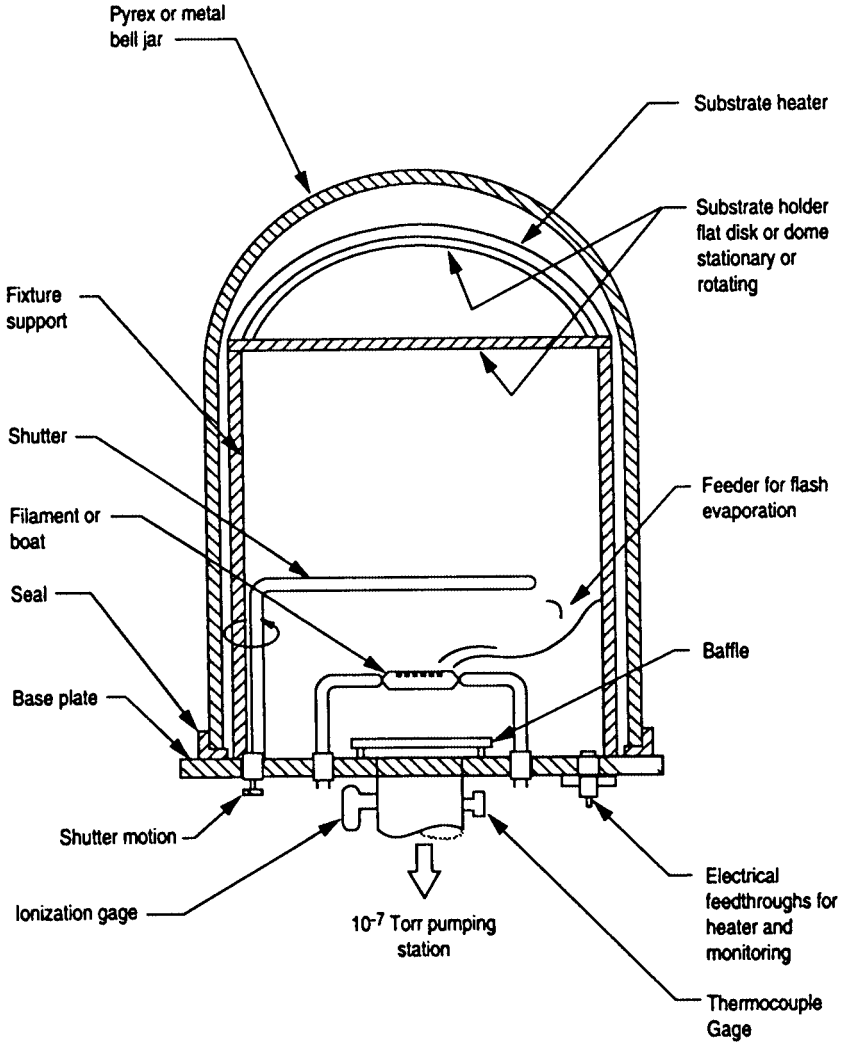

Figure 3.1 Schematic for vacuum evaporator.[12]

Downloaded from Digital Engineering Library @ McGraw-Hill (www.digitalengineeringlibrary.com)
Copyright © 2004 The McGraw-Hill Companies. All rights reserved.
Any use is subject to the Terms of Use as given at the website.

be plated is the anode. When a high electric field is applied between the electrodes in an evacuated chamber, argon purge gas is ionized. The Ar^+ ion is then accelerated by the electric field into the metal cathode. The high-energy collisions sputter ions of the target metal, forming a plasma that then deposits on the substrates at the anode. Figure 3.2 shows a schematic of a sputtering system. Because the material is depositing at a high kinetic energy level, the sputtered film is typically better adhered and more dense than evaporated films.

The properties of deposited films are highly dependent on the processing conditions and substrate properties such as surface chemistry and finish. Typically, a thin adhesion layer, such as Cr, Ti, NiCr, or TaN, is first deposited onto the substrate. This is followed by the high-conductivity metallization layer. Sometimes it is necessary to apply a final barrier layer over the metallization to prevent oxidation.

3.2.2 Thick film

In its simplest form, thick film technology involves the deposition of metal circuitry on a dense ceramic substrate using screen-printing technology. The metallizations are formulated with glasses and oxides to aid in densification of the metal and adhesion to the substrate at relatively low temperatures (600 to 950°C). The ability to build up multiple layers of circuitry using insulating dielectric layers is a key advantage of this technology. Successive layers are

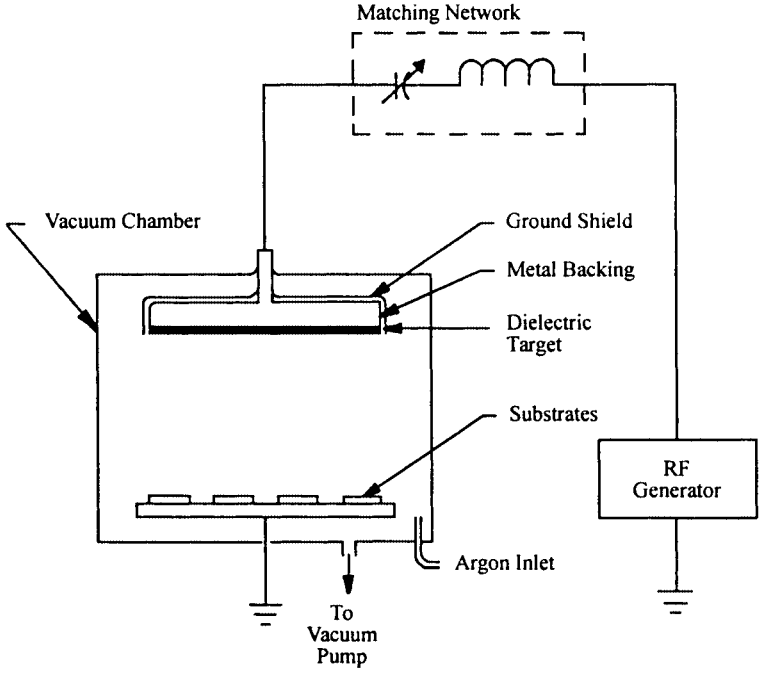

Figure 3.2 Schematic of RF sputtering unit.[12]

Downloaded from Digital Engineering Library @ McGraw-Hill (www.digitalengineeringlibrary.com)
Copyright © 2004 The McGraw-Hill Companies. All rights reserved.
Any use is subject to the Terms of Use as given at the website.

printed, dried, and fired to build up a multilayer structure on a rigid ceramic or metal base. The substrate material is widely varying; thick film metallization is used in nearly all forms of electronic ceramics, including magnetic, electro-optic, and superconductor substrate ceramics. Thick film circuits are often used as hybrid packaging, that is, as a method to interconnect active ICs and passive components such as capacitors, resistors, and inductors. Special pastes for deposition of inductors, capacitors, and resistors have been developed, greatly expanding the capabilities of the technology. Thick film has been in use in various forms since the 1920s and is one of the longest-running commodity markets in the electronics industry.

The metal, dielectric, resistor, and ferrite pastes consist of the organic vehicle, the metal or oxide powders, and a glass frit. The organic vehicle consists of a solvent, dispersants, and a binder system. The binder system is used to hold the fine inorganic particles together and form a temporary bond with the underlying substrate prior to the firing process. The organic binder resin dissolved in solvents and easily decomposed in air or nitrogen atmosphere. The solvents and dispersants are used with the binder and inorganic particles to form a paste form which can be deposited onto substrates using a rubber squeegee. Glass frit and/or bismuth or copper oxides are added to promote adhesion to the substrate. Typically, the frit consists of high lead or bismuth glasses are added to conductor paste blends to aid in adhesion. Glasses are chosen with a melting point approximately 200°C lower than the firing temperature of the paste.

Figure 3.3 shows the basis of the thick film process, screen printing. In screen printing, a rubber squeegee is used to force a thick paste through a screen, imaged for the circuit features, onto the substrate material. Typically, stainless steel mesh screens are used. The mesh of the screen is filled with a UV light-curable emulsion. Normally, the emulsion is thicker than the metal mesh, is flush with the mesh on the squeegee surface, and extends beyond the

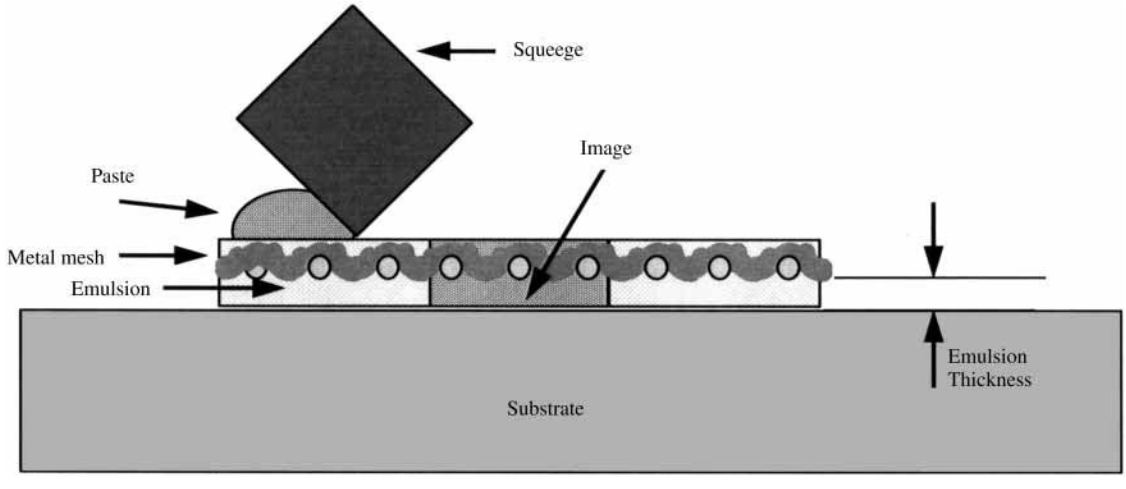

Figure 3.3 Contact printing schematic.

Downloaded from Digital Engineering Library @ McGraw-Hill (www.digitalengineeringlibrary.com)
Copyright © 2004 The McGraw-Hill Companies. All rights reserved.
Any use is subject to the Terms of Use as given at the website.

mesh on the substrate side of the screen. Emulsions typically extend beyond the thickness of the wires by several ten-thousandths of an inch. This additional emulsion is used to control print thickness and eliminate the mesh patterns from being transferred to the printed features. The circuit patterns to be printed are imaged into the screen emulsion using positive image artwork on Mylar film or glass plates. Those areas exposed to the UV light are cured. The noncured emulsion is water soluble and is washed away, leaving the open stainless steel mesh through which the thick film pastes will be deposited. Screen parameters such as mesh, emulsion thickness, wire diameter, and mesh angle determine the thickness and quality of the printed circuits. Screen meshes range from 200 to 400 mesh (wires per inch), but 325 mesh is most common. In general, finer wire diameters are desirable, but the fineness is limited by the tensile strength of stainless steel; 0.0006- to 0.002-in wires are used. Equipment parameters such as squeegee pressure, speed, and angle; snap-off; and down-stop also affect print quality. Also, material parameters such as paste rheology and control and substrate surface finish, porosity, and flatness affect print quality and variability.

Typically, two prints are used for each dielectric layer to avoid pinholes that would result in shorts between layers. The two dielectric layers are applied in print-dry-fire-print-dry-fire or print-dry-print-dry-fire fashion. As shown in Fig. 3.4, openings of ≈10 mils are designed into the dielectric layers to be filled with conductive pastes on subsequent processing. These metallized "vias" serve as the interconnect between the layers of circuitry. As increasing numbers of layers are applied, the substrate surface becomes less planar. Non-planar surfaces can result in difficulties in automated assembly of components to the package. This limits the number of circuit layers that can be applied using thick film technology to approximately seven or eight layers. The screen-printing operation limits the resolution of thick film circuitry to approximately 4-mil lines and spaces in volume production, and 6- and 8-mil lines are more common. Other technologies are being developed to expand the capabilities of thick film. Direct writing machines such as the Micropen can print circuitry through a dispensing nozzle. This system is capable of writing 3- to 4-mil lines with fine spaces (1 to 2 mil) over nonplanar surfaces and in cavities. Photoimageable and etchable thick film systems have been developed to improve the circuit resolution of thick film. DuPont's Fodel and Hereaus' KQ systems are examples. Some systems involve polymerization of the pastes by exposure to a UV light through a photonegative mask. The paste containing uncured polymer is washed away. This process of photo-imaging results in finer circuit features such as via diameters down to 100 mm. This allows for more densely packed circuitry. Etchable thick film metallizations have also been developed. The substrate is covered with a thick film layer of fired gold rather than deposited metal as in thin film processes. This metal can then be processed through subsequent thin film photoresist and etching processes to form fine-resolution circuits that are compatible with subsequent thick film printing and firing processes.

One of the key advantages of thick film is the use of high-conductivity metallizations such as Au-, Ag-, and Cu-based systems, as shown in Table 3.1b.

Downloaded from Digital Engineering Library @ McGraw-Hill (www.digitalengineeringlibrary.com)
Copyright © 2004 The McGraw-Hill Companies. All rights reserved.
Any use is subject to the Terms of Use as given at the website.

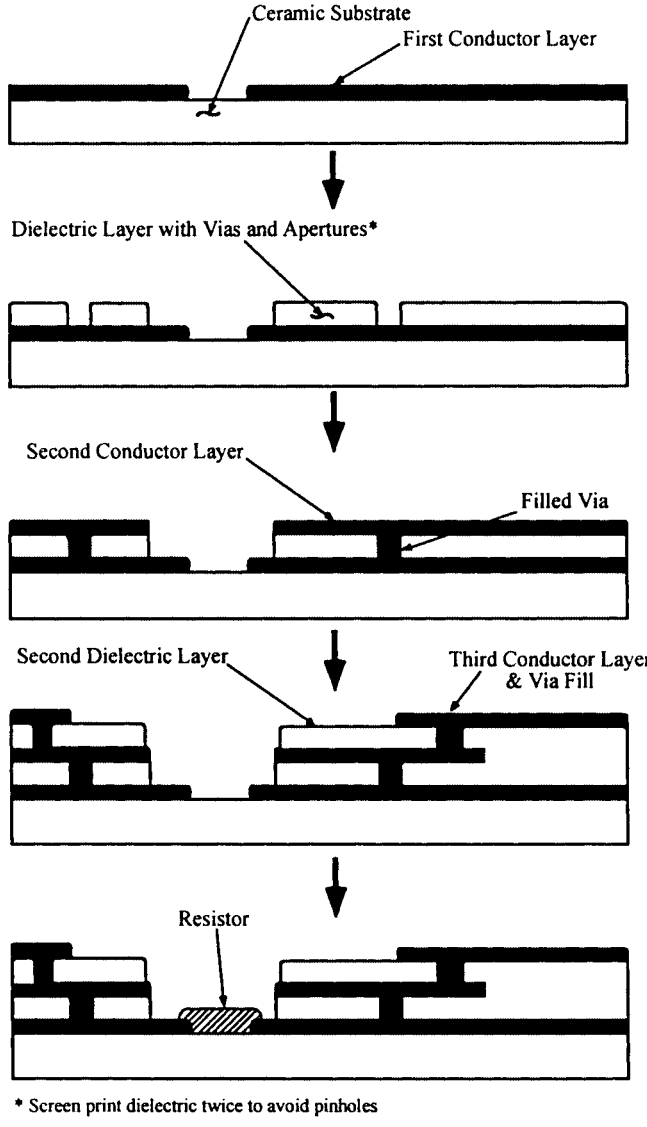

Figure 3.4 Thick film multilayer fabrication steps.[12]

The choice of metal systems is based on cost, package assembly, and performance requirements. Thick film may be Au and Al wire bondable, low-temperature solderable, or high-temperature brazable. Gold is often used for its noble metal properties; that is, its inertness to oxidation, migration, and chemical reaction. Gold circuits have excellent thermocompression bonding and high-temperature brazing (with Au-Sn, Au-Ge) properties but are not well suited for soldering because of poor leach resistance. Adding Pt and Pd to Au forms solid solutions that are more leach resistant but less conductive. The need for lower cost drove the development of Ag- and Cu-based conductors. Silver (1.5

Downloaded from Digital Engineering Library @ McGraw-Hill (www.digitalengineeringlibrary.com)
Copyright © 2004 The McGraw-Hill Companies. All rights reserved.
Any use is subject to the Terms of Use as given at the website.

TABLE 3.1b Properties of Dielectric Insulators

Material	Thermal expansion (ppm/°C)	Dielectric constant	Dielectric loss	Thermal conductivity (W/m-K)	Flexural strength (MPa)	Density (g/cc)
96%	7.4–8.2	9.5	0.0004	26	400	3.75
99.5% Al_2O_3	7.5–8.3	9.9	0.0002	35	552	3.90
Mullite	3.7–5.3	5.4–6.8	0.003	4–6.7	186	2.82–3.1
AlN	4.3–4.6	8.6–10.0	0.0002–0.001	140–220	207–345	3.25–3.30
BeO	7.5–8.8	6.5–6.7	0.0003	260	207	2.85
Steatite	4.2–7.2	5.7	0.00070.001	2.5	170–200	2.7
Fosterite	9.8–10.7	6.2	0.0002–0.0005	3.3–4.6	170–210	2.9–3.22
Spinel	7.0–8.8	6.6–8.3		7.6–15	200	3.6
Cordierite	1.4–2.5	4.5–5.7	0.004–0.008	2.5	120–245	2.0–2.53
Cristobalite	3.8	50.0				2.27–2.32
Porcelain	5.0	6.5		21–43	150–1200	3–3.18
SiC	3.1–4.7	40		36–270	230–860	3.2
a-quartz	11.2	3.8		2.0	180	2.2
BN	3.8	4.1		60 (cubic)–1300 (hex)	110–150	2.2
Diamond	1.1	5.5		2000	1400	3.5
Lead-borosilicate glass	7.0	7.0	0.004	2.5	320	3.1
Borosilicate glass	3.1	4.1	0.0006	2.0	150	2.3
Fused quartz	0.5	3.8	0.0004	1.6	80	2.2

to 3 mΩ/❑) and Cu (2 to 4 mΩ/❑) have better conductivity than Au (3 to 5 mΩ/❑) and are dramatically lower in cost, but they are prone to oxidation during firing. Silver also has problems with migration, especially in humid conditions. Alloying silver with palladium helps to reduce Ag migration. Copper has excellent stability and solderability but must be fired in an inert atmosphere to avoid oxidation. The metal powders are typically of spherical morphology. Flake-shaped particles are sometimes used for improving particle contact.

3.2.3 Multilayer packaging

The multilayer ceramic technology allows multiple circuitry's to be handled in a single, self-contained, hermetic package. Structures incorporating buried

Downloaded from Digital Engineering Library @ McGraw-Hill (www.digitalengineeringlibrary.com)
Copyright © 2004 The McGraw-Hill Companies. All rights reserved.
Any use is subject to the Terms of Use as given at the website.

components allow increased design flexibility by providing a mechanism for establishing both stripline and microstrip within the same medium. The ability to integrate digital, analog, RF, microwave, and buried passive components in this manner reduces assembly complexity and improves overall component and system reliability by reducing part count and interconnections.

The multilayer systems use low-dielectric-constant materials similar to traditional ceramic substrates for dielectric layers and an internal circuit metallization that is designed to be cofired with the ceramic dielectric. Cofiring of metallization with a ceramic dielectric required development of compatible systems that would have matching shrinkage onsets, shrinkage rates, and total volumetric shrinkage. Because the metal thermal expansions are considerably higher than that of the ceramic matrix, the metal must be compliant or have additives to make its thermal expansion more closely match that of the ceramic. Additionally, the thick film pastes must be formulated with solvents and binder systems that are compatible with that of the ceramic green tape. Additives to the metallization, in the form of glass frits or oxide bonding agents, are used to promote adhesion of the metal to the ceramic. Because these additives increase the resistivity of the metallization, the amount that can be employed is limited.

3.2.4 High-temperature cofired ceramics

The most common multilayer packaging technology to evolve uses alumina based material (90 to 94 percent) with silica and alkaline fluxes, such as MgO and CaO, added as sintering aids. The small amount of glass that forms is needed to improve the densification behavior of the dielectric and achieve better adhesion to the metallization. HTCC was first developed by IBM for use in mainframe computers. In the early 1980s, IBM developed a multilayer tape casting process for fabrication of a 33-layer cofired Mo metallization package housing 100 bipolar chips. The relatively high firing temperature of alumina-based ceramics, ≈1600°C, requires the use of more refractory metallizations for cofired internal circuitry. Because these metals possess high electrical resistivities (approximately four times that of gold), the electrical losses are higher than in other ceramic packaging technologies.

Figure 3.5 shows the fabrication process for HTCC packaging. The ceramic powders are dispersed in a solvent mixture with binder and plasticizers. The slurry is cast into thin tape form using a doctor blade process. The thin (0.5 to 10 mil) tape is heated during a continuous casting operation to dry off the solvents, leaving behind a thin flexible ceramic-organic composite. These flexible sheets enable low-cost assembly of very complex packages by forming the three-dimensional structure in the green state.

The thin sheets are cut to standard processing sizes. The circuit connections between layers (vias) are formed using programmable pneumatic punches or hard dies. These vias are filled with conductive metallization using stencils in a screen-printing process. The unique internal circuits are printed on the individual tape layers. Three-dimensional cavity patterns are formed by cutting the patterns in individual layers using punches, cutting dies, routing, and la-

Downloaded from Digital Engineering Library @ McGraw-Hill (www.digitalengineeringlibrary.com)
Copyright © 2004 The McGraw-Hill Companies. All rights reserved.
Any use is subject to the Terms of Use as given at the website.

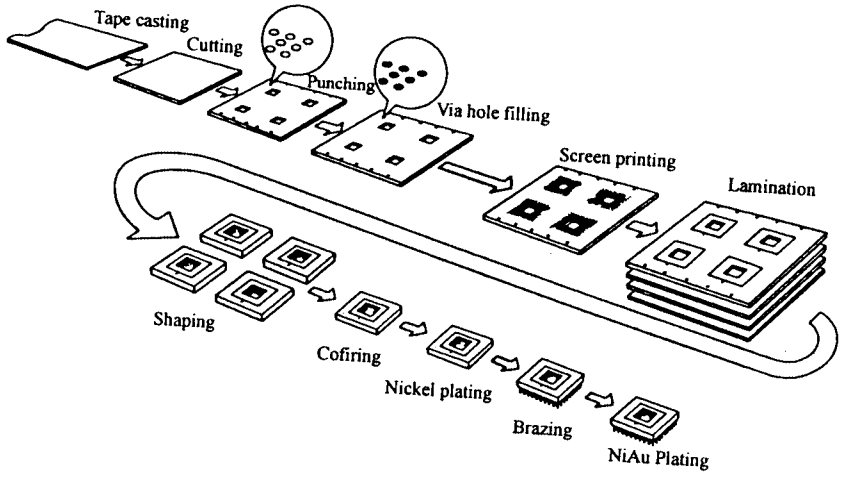

Figure 3.5 HTCC multilayer fabrication steps.[11]

ser cutting processes. The layers are stacked and registered relative to one another. The individual layers are laminated together using heated hydraulic presses. Typically, isostatic pressure is achieved on the three-dimensional structure with isostatic pressing or through the use of molds or conformal bladders or bags. Finally, the laminates are green cut to final or near-net expanded dimensions. The multilayer parts are then heated in a burnout and firing process to remove organics and densify the ceramic and metal materials.

The cofirable metal systems based on W, Mo, and Mn cannot be interconnected with traditional methods; that is, they are not wettable with solder systems or wire- or ribbon-bondable. Therefore, these packages require post-fire plating, electrolytic or electroless, with a Ni base layer, followed by a thin Au layer, to provide solder-wettable and wire-bondable terminations for interconnection. Electrolytic plating requires electrical connection to all pads requiring plating. The electroless systems plate all exposed metal surfaces.

3.2.5 Low-temperature cofired ceramics

Low-temperature cofired ceramic (LTCC) technology is based on inorganic materials and used as the housing material containing layers of dense circuit paths and assembled electronic components. LTCC has widespread applications in military, aerospace, wireless telecommunications, optical data transmission, and automotive and medical devices and equipment. LTCC technology was first developed for military avionics applications in the 1980s. Westinghouse Electric Corporation and Hughes Aircraft were the two companies driving the use of the technology in advanced weapon systems.

Monolithic LTCC structures incorporating buried passive components (resistors, capacitors, and inductors) reduces assembly complexity and improves overall component and system reliability of microelectronic packages by reducing part count and interconnections. Additionally, the reduced weight of

Downloaded from Digital Engineering Library @ McGraw-Hill (www.digitalengineeringlibrary.com)
Copyright © 2004 The McGraw-Hill Companies. All rights reserved.
Any use is subject to the Terms of Use as given at the website.

LTCC packages and the low microwave-frequency-loss characteristics of the dielectrics and conductors make this packaging technology an ideal candidate for high-performance commercial and military electronic systems.

Low-temperature cofired ceramic material is a glass ceramic composite that provides highly integrated, high-performance electronic packaging. LTCC utilizes material technologies and manufacturing processes developed for two very mature systems: high-temperature cofired ceramic (HTCC) and multilayer thick film substrates. The LTCC material system consists of a low-firing-temperature ceramic with the multilayering capability of HTCC and the high-conductivity metals (gold, silver, and copper) used in the thick film process. This combination of material technologies allows for low-temperature (<1000°C) processing of three-dimensional packages and the use of conventional chip and wire technologies for the fabrication of various complex LTCC packages. Traditional LTCC materials are glass-based systems that undergo devitrification to a crystalline phase during the firing process or consist of a glass matrix with crystalline filler. Figure 3.6 shows the microstructure of an LTCC material with crystalline filler and partial devitrification.

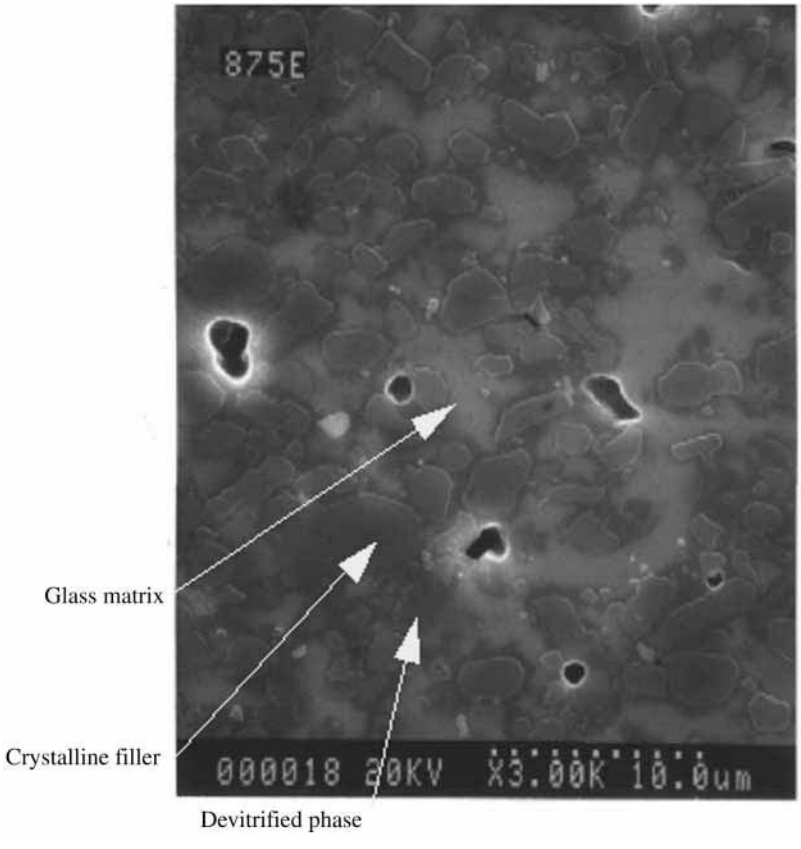

Figure 3.6 LTCC microstructure.

Downloaded from Digital Engineering Library @ McGraw-Hill (www.digitalengineeringlibrary.com)
Copyright © 2004 The McGraw-Hill Companies. All rights reserved.
Any use is subject to the Terms of Use as given at the website.

Because the glass phase of a material behaves as a supercooled liquid, it will densify at lower temperatures than the crystalline phase. The crystalline filler is added for thermal expansion match to the semiconductor chip, to control the densification behavior of the LTCC, and to achieve specific electrical performance. Figure 3.7 shows the effect of crystalline filler on TCE of a glass matrix LTCC. The crystalline phase is used for creating a thermal expansion match to other components. The key discriminating feature of LTCC is the low firing temperature, which enables the use of high conductivity metallizations in multilayer structures. This technology allows the high-density and high-resolution circuitry of HTCC in complex three-dimensional structures but uses the low firing temperature and, therefore, more highly conductive metallizations. The lower dielectric constants allow circuits with finer spacing without signal coupling.

Unlike the thick film process wherein successive lamination and firing steps cause bowing and line degradation at high layer counts, the single-step lamination and firing of LTCC produces a flat substrate with fine, high-quality line definition. In addition, the elimination of costly repeated firings greatly increases the number of conductive layers achievable. The ability to form complex three-dimensional structures with multilayer ceramic technologies offers a significant advantage in integrating multiple functions into a single cofired structure. That is, analog and digital signals from DC through microwave frequencies can be channeled through one package, achieving isolation of one section from another. Typically, ground via fences are used in the wall to divide various devices and achieve a high degree of electrical isolation.

Figure 3.8 depicts the core processing steps in the LTCC manufacturing process flow. The nine basic processes in the fabrication of an LTCC device are blanking, via formation, via filling, circuit printing, cavity formation, lay-up, lamination, firing, and post processing.

Blanking is the process by which sections of green tape of an appropriate size for processing are stripped from the Mylar carrier film and stabilized to remove residual stresses from the tape-casting process. Thermal and electri-

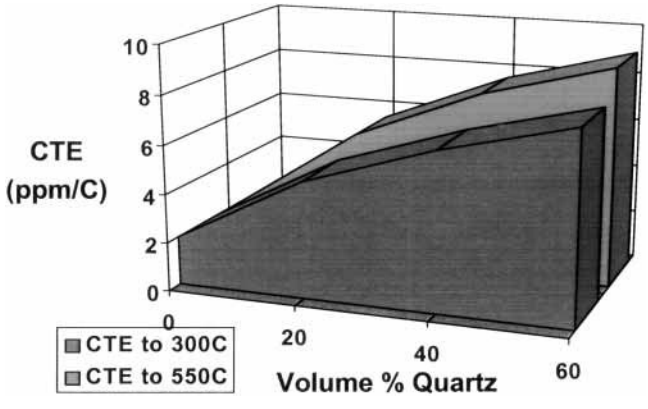

Figure 3.7 Effect of crystalline filler on thermal expansion of LTCC.

Downloaded from Digital Engineering Library @ McGraw-Hill (www.digitalengineeringlibrary.com)
Copyright © 2004 The McGraw-Hill Companies. All rights reserved.
Any use is subject to the Terms of Use as given at the website.

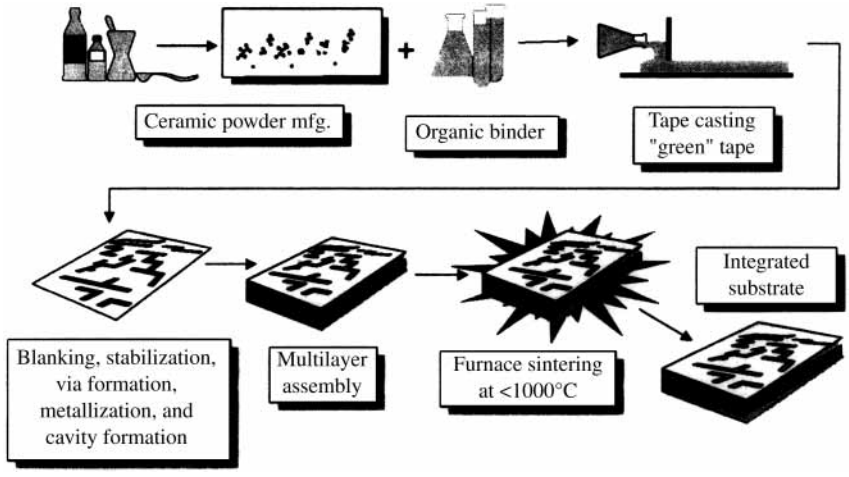

Figure 3.8 LTCC multilayer fabrication steps.

cal vias for interconnection between layers of circuitry (diameters ranging from 0.002 to 0.020 in) are formed in the appropriate layers of unfired tape using pneumatic punching equipment with 10,000+ vias per layer. In high volumes, specialized "gang" punches or fixed die sets are used.

Vias are subsequently filled with a specially formulated conductive material applied through a stencil in a screen-printing process. The stencil is made from 0.002- to 0.003-in thick brass or stainless steel containing etched or punched vias of the same pattern as the tape. The stencil and punched tape typically are optically aligned before printing the conductive pastes into the vias. Quality factors are completeness of fill, without overfill, and accuracy of the fill material placement.

Conductor patterns are printed on the green tape using the process used for printing thick film conductors. In general, printing on green tape is of better quality and higher resolution than is possible on a thick film substrate for two reasons: the printing is always done on a flat surface without the warping and topography characteristics of multilayer thick film, and the paste is deposited on a porous surface, which inhibits the tendency of the paste to spread.

The three-dimensional cavity structure is formed by cutting the patterns in each layer of tape in the required location using die punching, mechanical machining, or a carbon dioxide laser cutting process.

The individual sheets of processed tape used in a substrate are collated and aligned using tooling holes aligned to the via and circuit pattern in each layer of tape. The multilayer stack is then laminated under elevated temperature (70 to 90°C) and pressure (2000 to 6000 psi) to bond the individual layers into one cohesive stack.

Laminated stacks are fired in belt or box furnaces to burn out organic binders and densify the ceramic and metallic constituents. Burnout and firing can be accomplished in one continuous operation so that the part does not experience thermal gradients from end to end as the temperature is changed. Fin-

Downloaded from Digital Engineering Library @ McGraw-Hill (www.digitalengineeringlibrary.com)
Copyright © 2004 The McGraw-Hill Companies. All rights reserved.
Any use is subject to the Terms of Use as given at the website.

ished parts may be metallized with either a screen-printed thick film or a sputtered and etched thin film conductor.

The current state of the LTCC technology allows high-density circuitry (as fine as 0.003-in lines and spaces) interconnected with conductive vias (as fine as 0.0035-in diameter). The wide range of available dielectric constants in LTCC increases design flexibility. Dielectric constants as low as 3.8 are particularly well suited for high-speed digital applications. Moderate dielectric constants ranging from 6 to 80 are well suited for higher-frequency applications. The availability of high dielectric constants (up to 5,000) allows integration of capacitor devices into the multilayer structure. Resistor pastes are available that can be printed on internal layers of circuitry and cofired into the structure. This integration of passive components reduces the number of surface mount components, reducing the number of solder and wirebond connections, thereby increasing reliability. The ability to form complex three-dimensional structures with multilevel cavities and the ability to form grounded "walls" of conductive vias enables considerable isolation potential. This isolation allows multiple signals to be handled in one cofired package, reducing the number of substrates required, reducing interconnections, and thereby improving reliability. The fact that there are fewer exterior walls or housings when multiple circuits are contained in the same package also contributes to a reduction in volume as compared to individually packaged modules. The reduced part count leads to reduced labor hours in package manufacturing and assembly and therefore reduces costs. The reduction in the number of interconnections realized by combining functions or passive components into one package dramatically improves the reliability of the system.

Interconnect technologies such as land grid arrays (LGAs) and ball grid arrays (BGAs) used on ceramic packaging typically require the soldering of the ceramic package to an organic PWB. The large coefficient of thermal expansion (CTE) mismatch between the ceramic (6 to 7 ppm/°C typical) and organic (12 to 16 ppm/°C typical) can result in significant strain at the interface. Kyocera's HITCE system, formulated with high CTE glass and crystalline filler having a combined CTE of 11.5ppm/°C, is well suited for applications wherein the ceramic is to be attached to a PWB with a CTE in the 12 to 16ppm/°C range.

A comparison of the high-frequency electrical properties for several LTCC systems is shown in Figs. 3.9a and 3.9b. Table 3.2 provides a comparison of properties for various LTCC and HTCC systems.

3.3 Capacitors

Capacitors are essential components in most electronic circuits. Capacitors function to provide energy storage, current blocking, electrical noise filtering, high-frequency tuning, and other functions. Since the first demonstration of the energy-storage capability of a capacitor device in 1745 in Leiden, Netherlands (hence the "leyden" jar), in which a glass was used as the dielectric, capacitors have taken on a wide variety of designs. In the early 1900s, the first practical capacitor devices were fabricated from steatite porcelains, paper, and

Downloaded from Digital Engineering Library @ McGraw-Hill (www.digitalengineeringlibrary.com)
Copyright © 2004 The McGraw-Hill Companies. All rights reserved.
Any use is subject to the Terms of Use as given at the website.

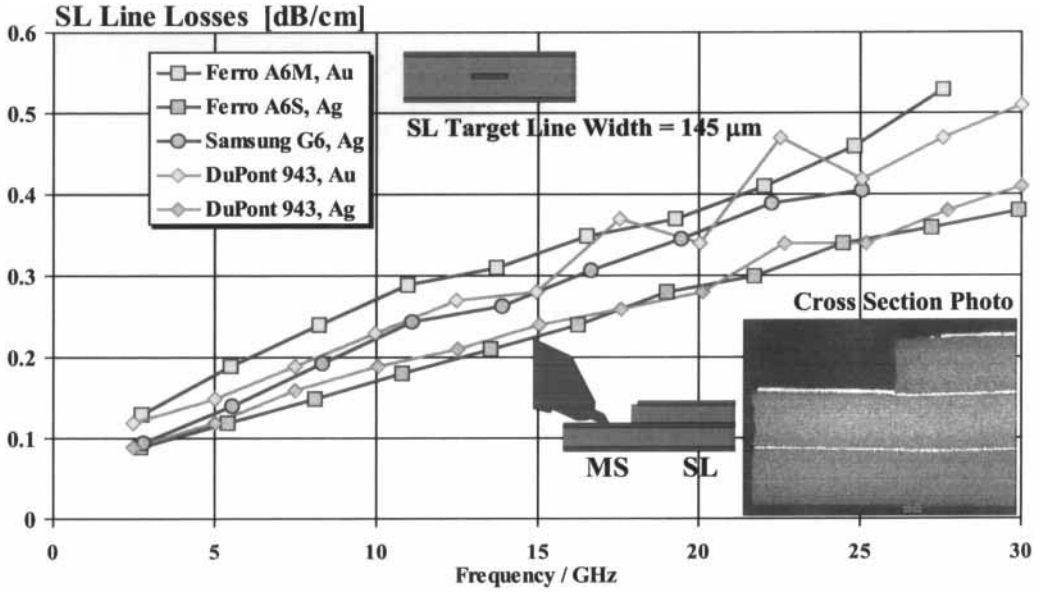

Figure 3.9a Measured line losses of buried striplines.[15]

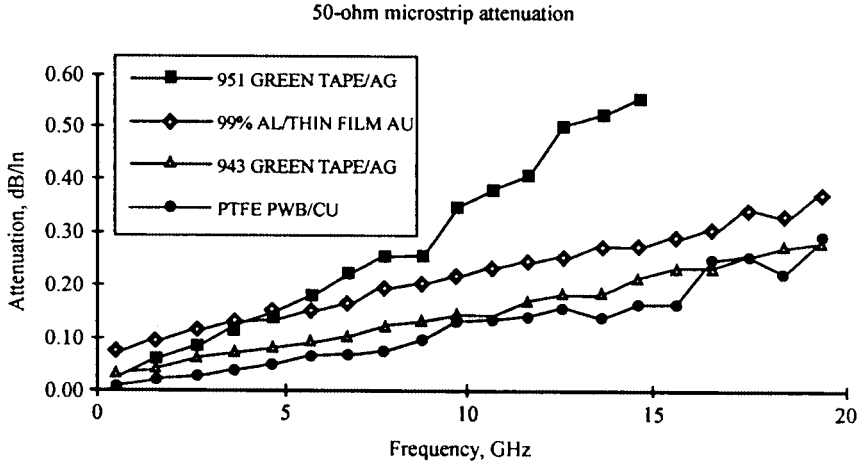

Figure 3.9b Attenuation vs. frequency for DuPont LTCC with silver conductor vs. thin film and PTFE printed wiring board.

mica. Lower-loss porcelains were developed in the 1920s, followed by higher-dielectric-constant TiO_2-based ceramics in the 1930s. In 1942, researchers at the American Lava Co. discovered the ferroelectric behavior of $BaTiO_3$. $BaTiO_3$ has been modified over the years, forming solid solutions with other perovskites and doping with various ions. $BaTiO_3$ remains the most widely used material in the ceramic capacitor industry today. Process refinements have

Downloaded from Digital Engineering Library @ McGraw-Hill (www.digitalengineeringlibrary.com)
Copyright © 2004 The McGraw-Hill Companies. All rights reserved.
Any use is subject to the Terms of Use as given at the website.

TABLE 3.2 Properties of Multilayer Ceramic Packaging

Material	Primary phase	Thermal expansion (ppm/°C)	Dielectric constant	Dielectric loss	Thermal conductivity (W/m-K)	Flexural strength (MPa)	Density (g/cc)
HTCC	Al_2O_3	7.1	9.5	0.0004	25	420	3.9
Kyocera	Al2O3	7.0	10	0.002	18	275	3.6
NTK	>92% Al_2O_3	6.8	9.4		17		
IBM	92% Al_2O_3	6.5	9.5		20	275	
NTK	Mullite	4	6.6		5		
Kyocera	Mullite	4.2	6.4	0.002	5	196	2.9
ALN	ALN	4.4	8.9	0.0004	175	320	3.3
NTK	AlN		8.9		170		
Kyocera	AlN	4.6	8.5	0.0004	150	343	3.4
Kyocera	SiC	3.7	45		270	441	
LTCC	Glass-matrix, crystallized	3–7	3.9–7.5	0.0002–0.003	2	180–210	2.25–3.0
NTK	Crystallized glass	3	4.9–5.6		3		
IBM	Cordierite	3	5.3–5.7		5		
IBM	Spodumene	2.8	5.65				
DuPont 951	Pb-BSG + $CaZrO_3$ + Al_2O_3	7	7.1	.007	3	206	
DuPont 943	Crystallized glass + Al_2O_3	5.3	7.5	0.001	3.0	230	3.2
Ferro A6	Crystallized Ca-BSG	3	5.9	.002	2		2.
Northrop	BSG + Quartz	6.8	3.9	.0008	2	100	2.3
Fujitsu	BSG + Al_2O_3	4	5.7		2.5	200	
NEC	Pb-BSG + Al_2O_3	7.9	7.8	0.003		343	
Kyocera	Glass-ceramic	7.9	7.9	0.003	2	196	2.8
Kyocera	Glass-ceramic	4.0	5.0	0.0029	2	186	2.5
Murata		8.0	6.1	0.0007	4.2	196	

Downloaded from Digital Engineering Library @ McGraw-Hill (www.digitalengineeringlibrary.com)
Copyright © 2004 The McGraw-Hill Companies. All rights reserved.
Any use is subject to the Terms of Use as given at the website.

contributed to dramatic improvements in capacitor performance through the years. The development of tape casting and cofired metallizations enabled the fabrication of multilayer capacitors (MLCs) with extremely high capacitance density. Chemical synthesis techniques have led to fine-particle dielectric powders that densify at lower temperatures and have better breakdown strengths.

The capacitance of a device is a measure of the charge stored per applied voltage and is measured in units of farads or s^2coulomb^2/kgm^2. In its simplest form, a capacitor consists of two parallel electrodes separated by a dielectric medium. The capacitance of such a device, in units of farads, is given by

$$C = A\varepsilon_r\varepsilon_o/t \tag{3.2}$$

where A = effective area of electrode plates
ε_o = permittivity of free space
ε_r = materials relative permittivity (dielectric constant)
t = separation distance between electrodes

The intrinsic volumetric energy density (U) of a parallel plate capacitor, in units of J/cm^3, is given by

$$U_{vol} = \int EdP = \frac{1}{2}\varepsilon_r\varepsilon_o E^2 \tag{3.3}$$

where P is the polarization resulting with an applied electric field E.

Substituting Eq. (3.2), the electrical energy stored, in units of joules (W-s), in a capacitor is given by

$$U_{device} = \frac{1}{2}CV^2 \tag{3.4}$$

where V is the applied voltage. These relationships show that the energy density could be maximized by increasing the permittivity, the applied electric field, or both.

While all capacitors are based on metal electrodes separated by a dielectric material, they come in many different forms. Table 3.3 gives a list of various capacitor materials and designs. The capacitance per unit volume of a device can be increased by increasing the area:thickness ratio or using higher-permittivity materials. The development of cofired multilayer process in the 1950s enabled fabrication of thin dielectric layers, mechanically stacked in series and electrically connected in parallel. High-permittivity materials will raise capacitance values but, in general, with higher permittivity comes higher loss.

Polymer film capacitors are fabricated by interleaved polymer sheets and aluminum electrodes. The dielectric thickness is typically several microns, so relatively high capacitive densities can be achieved. The use of thin layers of oil-impregnated polymer dielectrics with low permittivities (εr = 3 to 10) has enabled operation at fields up to 300 MV/m, yielding energy densities as high as 3 J/cm^3. Ceramic capacitors have significantly higher permittivities (up to

Downloaded from Digital Engineering Library @ McGraw-Hill (www.digitalengineeringlibrary.com)
Copyright © 2004 The McGraw-Hill Companies. All rights reserved.
Any use is subject to the Terms of Use as given at the website.

TABLE 3.3 Alternative Capacitor Materials and Designs

Type	Materials	Operating freq., Hz	Benefits
Polymer film	Polystyrene, polypropylene, polyester, polycarbonate, PVD, PVDF, paper	$0–10^{10}$	High voltage, high energy density, self-healing
Electrolytic	Aluminum foil electrodes with electrolyte-impregnated paper dielectric	$0–10^{4}$	High capacitance
Tantalum	Porous Ta with MnO_2 or wet electrolyte	$0–10^{4}$	Stable
Mica	Mica plates clamped in multilayer stack	$10^{3}–10^{10}$	Low cost, one of the first capacitor materials
Ceramic	Ferroelectric perovskites	$10^{2}–10^{10}$	High capacitance
Multilayer ceramic	Tape-cast ferroelectric dielectrics cofired with internal electrodes	$10^{2}–10^{10}$	Embedded passives in hybrid circuits
Thick film	Usually $BaTiO_3$,-based paste with glass adhesion promoters fired onto substrate	$10^{2}–10^{10}$	Embedded passives in hybrid circuits
Thin film	Dielectrics such as SiO_2 or TiO_2 deposited on a substrate	$10^{2}–10^{10}$	Embedded passives in hybrid circuits

≈25,000), however, ceramic dielectrics have not realized their full potential because of a reduction in permittivity and resistivity at high fields and, therefore, low breakdown strengths. Recent improvements in ceramic processing and materials properties are rivaling the state-of-the-art polymer capacitors. Polymer film capacitors currently hold at least 25 percent of the market.

Electrolytic capacitors consist of aluminum foil electrodes separated by a thin sheet of porous paper and wound into a cylindrical shape. The paper is impregnated with an electrolyte solution. These capacitors are relative inexpensive to fabricate and allow very high capacitance values. The drawbacks to electrolytics are that they are polar and operate only at lower frequencies (<10 kHz).

Tantalum capacitors are formed by sintering Ta metal powder around a Ta lead wire to form a porous body that serves as the anode. The porous Ta is then coated with a semiconductive MnO_2 layer, which is coated with carbon and silver paints to form the cathode. A supporting T-bar is then welded to the lead wire, and the assembly is encapsulated. A wet electrolyte may be used in place of the MnO_2. Tantalum capacitors are very stable over time and temperature.

Mica capacitors consist of mica, $KAl_2(Si_3Al)O_{10}(OH)_2$, plates with fired-on silver electrodes. The metallized plates are stacked together in a multilayer fashion. Mica capacitors are extremely stable over time, have low thermal coefficient of capacitance, and have relatively low loss.

Ceramic capacitors are fabricated in four general processes: thin film, thick film, single-layer, and multilayer. Thin film capacitors were developed to address a need to embed passive components into electronics packaging—hybrid

Downloaded from Digital Engineering Library @ McGraw-Hill (www.digitalengineeringlibrary.com)
Copyright © 2004 The McGraw-Hill Companies. All rights reserved.
Any use is subject to the Terms of Use as given at the website.

circuits. Dielectrics such as SiO, SiO_2, Ta_2O_3, TiO_2, titanates, and aluminosilicates can be vacuum deposited with a variety of electrode metallizations.

Thick film hybrid packaging consists of layers of screen-printed/fired dielectric and circuit layers. Here again, the desire to embed passive devices into the substrate drove the development of thick film capacitors. The screen-printed pastes consist of a high-K dielectric, usually $BaTiO_3$ based, a glass binder, and organic constituents such as binder, dispersant, and solvent.

Single-layer capacitors represent the simplest form of ceramic capacitors. These capacitors use a single layer of dielectric ceramic between two metal electrodes. The dielectric may be in the form of a disc, cylinder, or rectangular plate.

In general, capacitors are designed to take advantage of the material and geometric contributions to the capacitance. However, there are secondary properties of capacitors that drive the design. For example, high-permittivity materials are desired to maximize the energy density per unit volume, but the material must also exhibit some specified temperature response and possess low dielectric loss. For this reason, the material selection for a specific application is generally a compromise. Because capacitance is additive when individual capacitors are placed in parallel, it is desirable to use multilayer devices with interdigitated electrodes. To take advantage of the inverse relationship to dielectric thickness, there is a drive to improve processes and powder characteristics to achieve thinner dielectric layers.

Figure 3.10 shows the simple disc capacitor structure containing one layer of ceramic dielectric. This structure was the standard for ceramic capacitors for many years. The development of multilayer capacitors has eroded the market for single-layer discrete devices. The most efficient way to maximize capacitance is to stack many thin layers of dielectric in series and connect them electrically in parallel as shown in Fig. 3.11. When connected electrically in parallel, $C_{total} = C_1 + C_2 + C_3 + ...$

Two processes for forming MLCs are shown in Fig. 3.12. In both processes, the dielectric powders are mixed in a solvent solution with dispersant, organic binders, and plasticizers. In the tape process, the slurry is de-aired and cast into thin sheets using a doctor blade. The slurry is typically pumped into a reservoir. The leading edge of the reservoir has a small, adjustable gap. A metal belt or polymer film moves under the reservoir and doctor blade. As it does so, a thin film of slurry is carried along the belt. This thin film continues to move through a heated bed to gradually drive off solvents, leaving a flexible ceramic binder film, *green tape.* The end of the caster is typically equipped with a spooler so that the casting is a continuous process. The green tape is typically 50 to 60 volume percent ceramic and 25 to 30 volume percent organic binder. Dielectric sheets from 15 to 100 μm thick are typical. Sheets of the green tape are printed using a screen printer with a metal-organic paste, typically Ag or Ag-Pd based, to form the pattern of the internal electrodes. The pastes are dried, and the printed sheets are stacked and laminated at elevated pressure (1 to 4 Ksi) and temperature (50 to 90°C). Individual capacitors are diced from the laminated block prior to firing by a hot-knife or gang saws.

For thinner dielectric layers, 10 to 25 mm, a wet lay-down process is used. The wet lay-down process differs from the tape process in that the multilayer

Downloaded from Digital Engineering Library @ McGraw-Hill (www.digitalengineeringlibrary.com)
Copyright © 2004 The McGraw-Hill Companies. All rights reserved.
Any use is subject to the Terms of Use as given at the website.

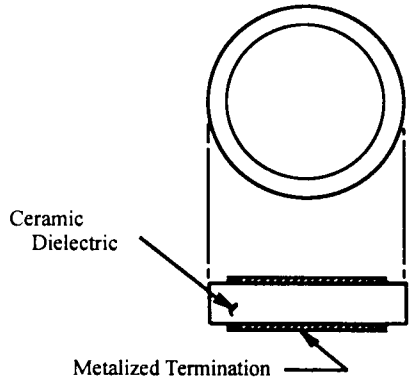

ASSEMBLED DISC CAPACITOR

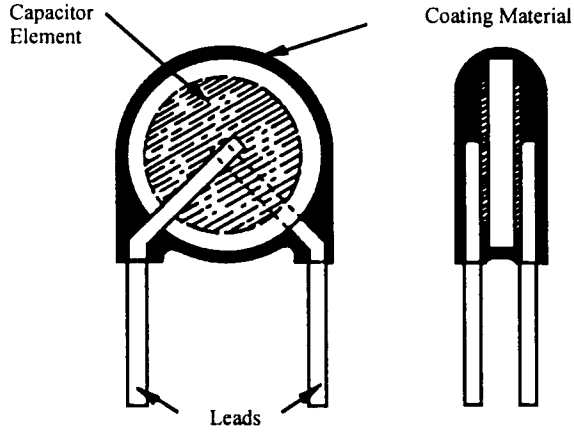

Figure 3.10 Simple disk capacitor design.[16]

structure is built up through a successive printing and drying process. Here, the slurry is printed onto a carrier plate in very thin layers. The printed dielectric is dried, and the process is repeated to avoid pinholes. The electrode print is applied to the dried dielectric layer. This process is repeated to build up the multilayer structure. The capacitors are fired in a variety of methods, but all go through some method of binder decomposition followed by sintering of the metal and ceramic particles. The fired capacitors are then terminated on two sides to achieve electrical connection to alternate layers.

3.3.1 Capacitor material classification

The Electronic Industries Alliance (EIA, formerly Electronic Industries Association) has specified a method of classifying capacitors based on their capacitance value and temperature sensitivity. Class 1 capacitors are highly stable

Downloaded from Digital Engineering Library @ McGraw-Hill (www.digitalengineeringlibrary.com)
Copyright © 2004 The McGraw-Hill Companies. All rights reserved.
Any use is subject to the Terms of Use as given at the website.

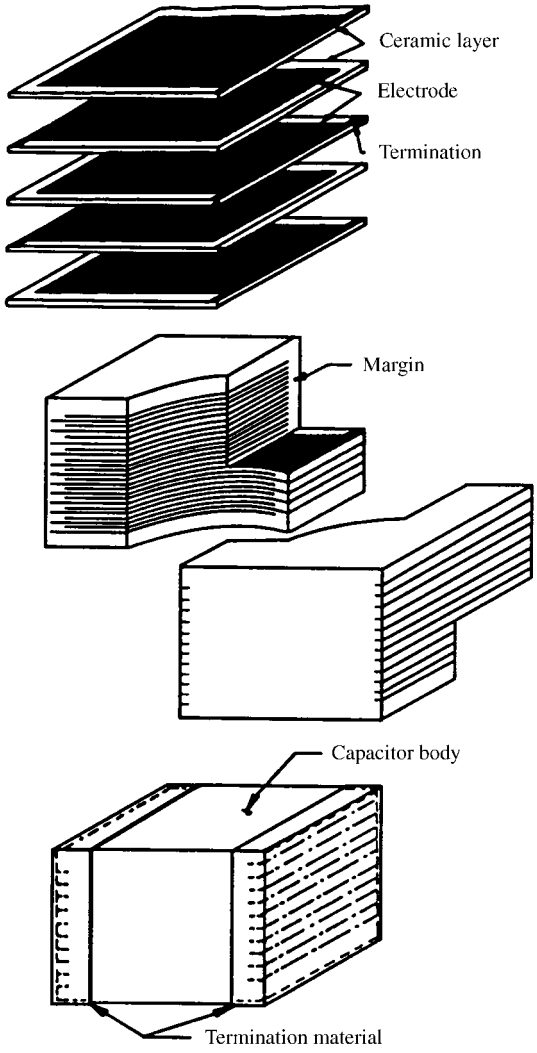

Figure 3.11 Multilayer capacitor design.[16]

with respect to temperature and time (i.e., no aging) and have low loss. Typically, these capacitors are made with titanates or tantalum. Class 2 capacitors are significantly more affected by temperature, time, and frequency; however, they are made from materials with much higher dielectric constants. Class 2 capacitors are typically made with ferroelectric materials and possess a broad range of stability. Therefore, EIA also set categories for temperature stability, outlined in Table 3.4. The classification of Class 2 capacitors is expressed in terms of three symbol codes. The first symbol represents the lower operating temperature, the second represents the upper operating temperature, and the third represents the change in capacitance over the operating temperature range.

Downloaded from Digital Engineering Library @ McGraw-Hill (www.digitalengineeringlibrary.com)
Copyright © 2004 The McGraw-Hill Companies. All rights reserved.
Any use is subject to the Terms of Use as given at the website.

Ceramics and Glasses

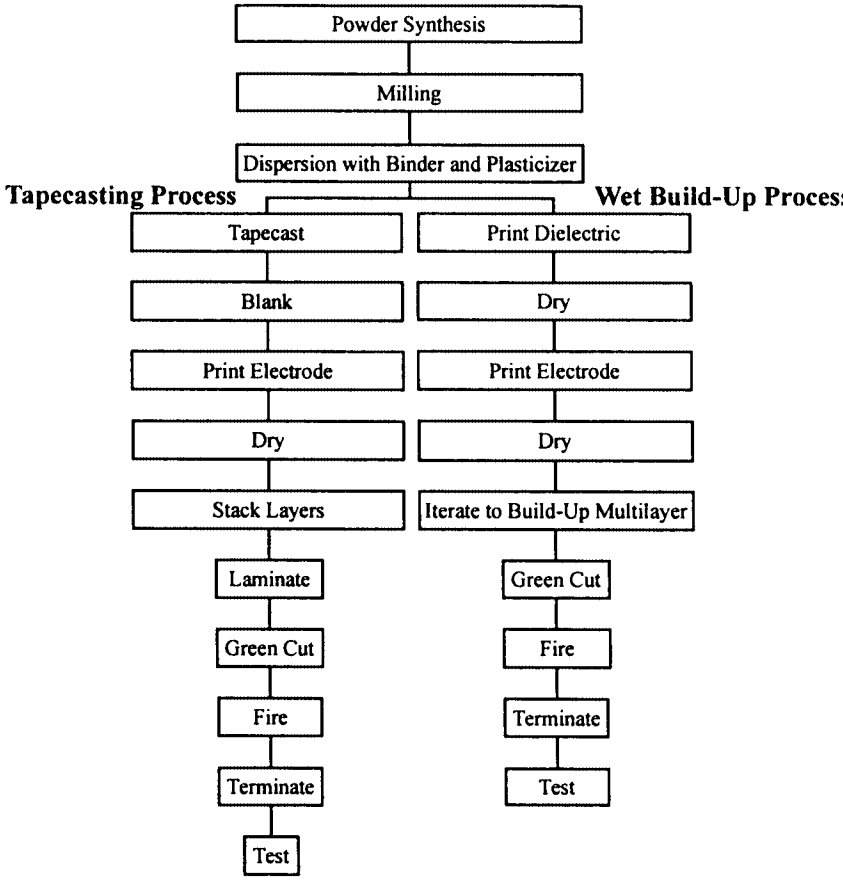

Figure 3.12 Multilayer capacitor fabrication steps.

Negative-positive 0-ppm/°C (NPO) devices are Class 1 dielectrics typically based on rutile TiO_2. These compositions can contain up to 50 percent $BaTiO_3$, which raises the dielectric constant and balances the negative temperature coefficient of rutile as shown in Table 3.5. Class 1 dielectrics are necessary for applications where a high degree of stability is necessary, as shown. Figure 3.13 shows the temperature stability for various classes of capacitors.

Class 2 devices are based on ferroelectric materials with considerably higher dielectric constants, such as those listed in Table 3.5. These materials exhibit shifts in dielectric constant as a function of time (aging). This phenomenon is a result of ferroelectric domain movement over time. A typical aging curve is shown in Fig. 3.14. The application of heat, voltage, or stress to the material will have a de-aging effect. Increasing frequency will result in reduced dielectric constant and increased dissipation factor in Class 2 dielectrics.

Applying DC voltage to a Class 1 dielectric results in a decreased capacitance and dissipation factor. AC voltages tend to raise the dielectric constant and dissipation factor (see Fig. 3.15).

Downloaded from Digital Engineering Library @ McGraw-Hill (www.digitalengineeringlibrary.com)
Copyright © 2004 The McGraw-Hill Companies. All rights reserved.
Any use is subject to the Terms of Use as given at the website.

TABLE 3.4 Electronics Industries Association (EIA) Capacitor Classifications and Examples

EIA code	Temperature range (°C)	Change in capacitance (%)	Typical dielectric constant	Typical dielectric loss (%)
X7	–55 to +125			
X5	–55 to +85			
Y5	–30 to +85			
Z5	+10 to +85			
D		±3.3		
E		±4.7		
F		±7.5		
P		±10		
R		±15		
S		±22		
T		+22 to –33		
U		+22 to –56		
V		+22 to –82		
Examples				
X7R	–55 to +125	± 15	3000–4000	<2.5
Z5U	–10 to +85	+22 to –56	8000–10,000	<4.0
Y5U	–30 to +85	+22 to –56	12,000–20,000	<4.0
Y5V	–30 to + 85	+22 to –82	12,000–25,000	<4.0
COG (NPO)	–55 to + 125	30 ppm/°C	up to 100	<0.1

Figure 3.16 shows the basic perovskite structure of $BaTiO_3$. The paraelectric perovskite is cubic and has an ABO_3 form with one formula unit per unit cell. The A site is at the corners of the unit cell, the B site is at the unit cell center, and the oxygens are at the unit cell face centers. The ferroelectric perovskite phases are in the same arrangement as the cubic phase, but the unit cell is slightly distorted into a tetragonal, rhombohedral, or orthorhombic structure. The A site atoms are coordinated by 12 O^{-2} atoms, and the B site atoms are coordinated by six O^{-2} atoms.

$BaTiO_3$ is the most common ceramic capacitor material as a result of its high permittivity, stability, and ease of doping. Figure 3.17 shows the unit cell dimensional change and associated dielectric constant change for $BaTiO_3$ as a function of temperature. The diagram shows that stoichiometric $BaTiO_3$ un-

Downloaded from Digital Engineering Library @ McGraw-Hill (www.digitalengineeringlibrary.com)
Copyright © 2004 The McGraw-Hill Companies. All rights reserved.
Any use is subject to the Terms of Use as given at the website.

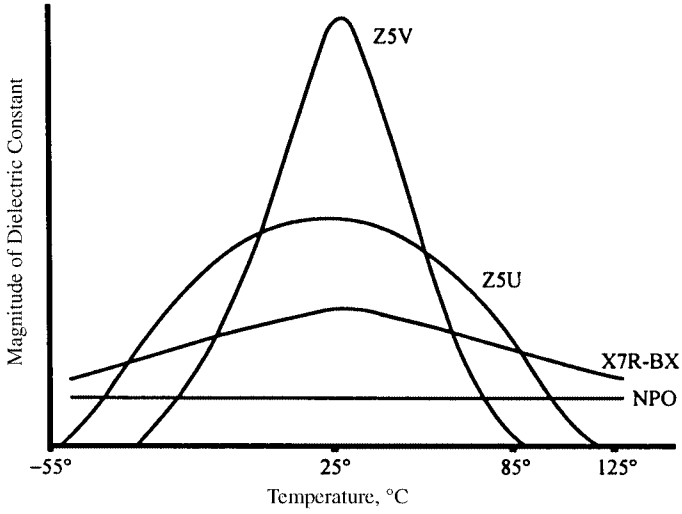

Figure 3.13 Temperature dependence of capacitance for various dielectrics.[16]

TABLE 3.5 Ceramic Capacitor Materials

Material	Relative permittivity	Dissipation factor (%)
TiO_2	110	0.02–004
$SrTiO_3$	285	<0.1
$CaTiO_3$	130	<0.1
$MgTiO_3$	16	0.01–0.03
Al_2O_3	10	0.04
MgO	10	<0.1
Steatite	6	0.03–0.1
$BaTi_4O_9$	40	0.01–0.03
$BaTiO_3$ (BT)	14,000	1–3%
BT + $CaZrO_3$	5700–700	<3%
$BaSrCaZrTiO_3$	11,500–14,000	<3%
$Ba(TiZr)O_3$	10,000	<3%
PMN-PT	20,000–28,000	<3%
PFN–PFW	24,000	<3%

Downloaded from Digital Engineering Library @ McGraw-Hill (www.digitalengineeringlibrary.com)
Copyright © 2004 The McGraw-Hill Companies. All rights reserved.
Any use is subject to the Terms of Use as given at the website.

Ceramics and Glasses

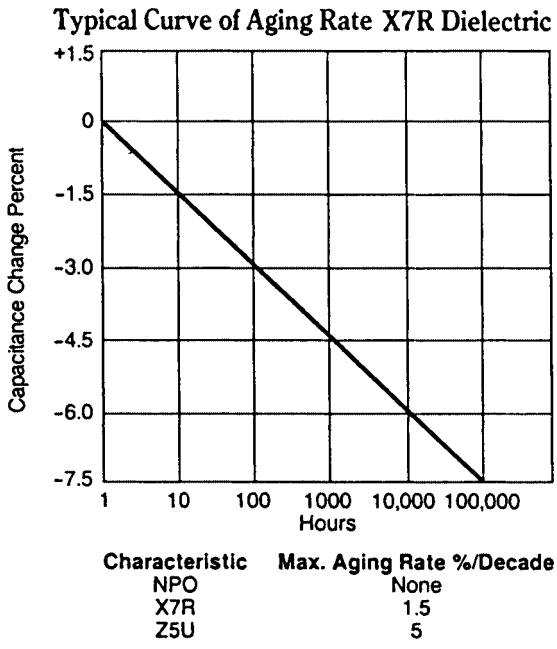

Figure 3.14 Aging behavior of various dielectrics.[4]

dergoes several phase transitions on cooling from high temperature. At approximately 110°C the high-temperature cubic phase converts from a paraelectric cubic phase to tetragonal ferroelectric phase. Cooling further results in conversion to an orthorhombic phase at approximately –10°C and a rhombohedral phase at approximately –100°C. At high temperatures, the lattice is expanded sufficiently to allow the B site ion to be centered in the cubic structure. As the material is cooled, the B site ion is shifted off center, creating a permanent dipole.

Perovskite $SrTiO_3$ (ST) is also a base capacitor material with a dielectric constant of approximately 300 at room temperature. Pure $SrTiO_3$ is paraelectric with a transition temperature near 0 K. $SrTiO_3$ is frequently used in high-voltage applications, because its dielectric constant is relatively independent of electric field, shows virtually no electrostrictive strain at high field, and maintains high resistivity at high fields. It is therefore resistant to voltage breakdown (see Figs. 3.18 and 3.19). Commercial $SrTiO_3$ compositions are typically donor doped to reduce oxygen vacancies and improve resistivities.

Calcium titanate, $CaTiO_3$ (CT), is used in applications similar to those of ST; however, the dielectric constant is roughly half that of ST as shown in Fig. 3.18. $CaTiO_3$ has a relatively flat dielectric constant over temperature and field. Both ST and CT are used in solid solutions with higher-permittivity materials to improve temperature and field stability.

Magnesium titanate, $MgTiO_3$ (MT), is an ilmenite structure material with a low but stable dielectric constant ($K = 16$). MT meets the EIA requirements for an NPO capacitor formulation of <30 ppm/°C over –55 to 125°C.

Downloaded from Digital Engineering Library @ McGraw-Hill (www.digitalengineeringlibrary.com)
Copyright © 2004 The McGraw-Hill Companies. All rights reserved.
Any use is subject to the Terms of Use as given at the website.

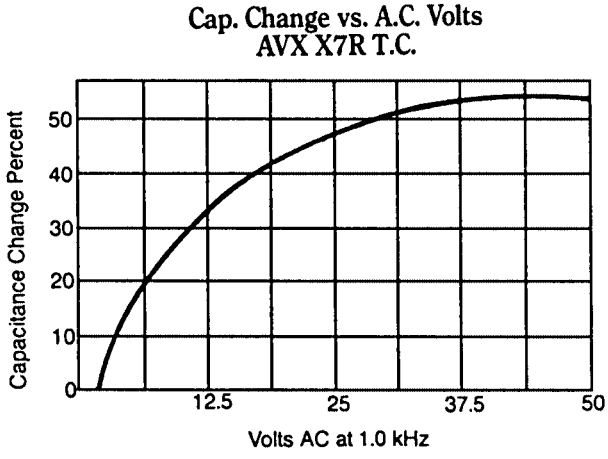

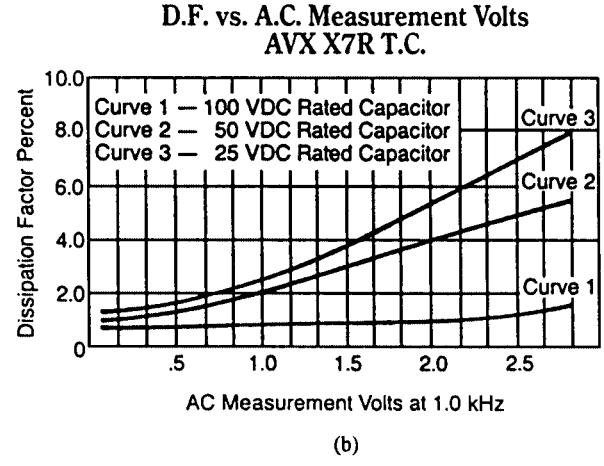

Figure 3.15 Effect of DC and AC voltages on capacitance and dissipation factor.[4]

Lead titanate, $PbTiO_3$ (PT), is a ferroelectric perovskite material with a Curie temperature near 490°C. PT is used extensively as a piezoelectric material; however, it is often used in solid solutions with other perovskites to improve capacitance and stabilize the perovskite phase. Modification of PT with Sr^{2+} substitutions for Pb^{2+} and W^{6+} and Mg^{2+} substitutions for Ti^{+4} yield excellent capacitor formulations with $K = 5000$ at room temperature.

Lead magnesium niobate, $Pb(Mg_{1/3}Nb_{2/3})O_3$, is a ferroelectric relaxor material that is paraelectric at room temperature. The perovskite phase is typically modified with additions of lead titanate or barium titanate, which raises the Curie temperature to near room temperature. Very high dielectric constants can be achieved (>20,000) but at the expense of temperature stability.

Downloaded from Digital Engineering Library @ McGraw-Hill (www.digitalengineeringlibrary.com)
Copyright © 2004 The McGraw-Hill Companies. All rights reserved.
Any use is subject to the Terms of Use as given at the website.

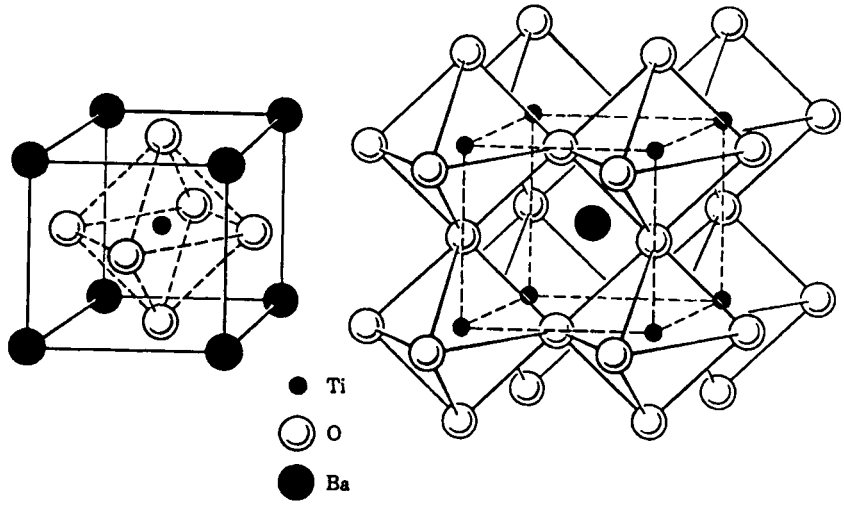

Figure 3.16 Perovskite $BaTiO_3$ structure.[14]

3.3.2 Effect of additives

Sharp changes in dielectric properties as a function of temperature are generally impractical. The properties of perovskites such as $BaTiO_3$ can easily be modified by additions of materials that form solid solutions in the perovskite structure. Isovalent substitutions on both the A and B site can be used to alter the transition temperature of perovskite materials. The ionic radii for the constituent and dopant ions are shown in Table 3.6 for the perovskite structure. In $BaTiO_3$, Pb^{2+}, Ca^{2+}, Sr^{2+}, and Cd^{2+} are substituted on the larger A site (1.3 to 1.6). Pb^{2+} raises the phase transition (Curie temp) temperature, Sr^{2+} lowers T_c, and Ca^{2+} broadens the transition. These effects are predictable if one considers these substitutions as solid solutions in titanate form. For example, $PbTiO_3$ has a higher (500°C) Curie point than $BaTiO_3$, and $SrTiO_3$ is near 0 kelvins (K). Therefore, one would expect Pb^{2+} additions to raise the Curie point and Sr^{2+} additions to drop the transition temperature. Hf^{4+}, Zr^{4+}, and Sn^{+4} can be used to substitute for Ti^{4+} on the smaller B site (0.6 to 0.75) of the perovskite structure. Isovalent substitutes have quite high solubility in the perovskite structures. Figure 3.20 shows the effect of isovalent substitutions on the transition temperature.

The effects of acceptor and donor ion substitutions in the perovskite structure was described by Jaffe, Cook, and Jaffe, as outlined in Table 3.7. Ion valences of the acceptor-type impurity atoms are lower than that of the constituent atoms. Oxygen vacancies are introduced to maintain charge balance. A decrease in DC resistivity has been attributed to the presence of charge carriers such as oxygen vacancies in the lattice. The decrease in resistivity ultimately leads to dielectric breakdown, but many ceramics fail because of the presence of voids or microcracks, which serve as initiation points

Downloaded from Digital Engineering Library @ McGraw-Hill (www.digitalengineeringlibrary.com)
Copyright © 2004 The McGraw-Hill Companies. All rights reserved.
Any use is subject to the Terms of Use as given at the website.

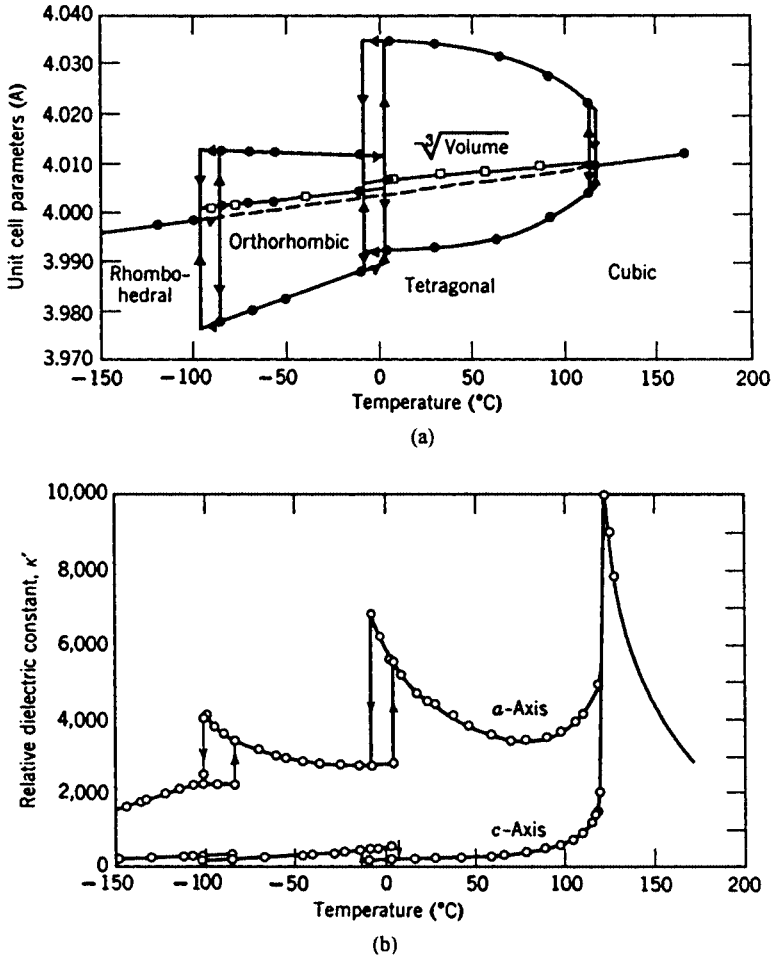

Figure 3.17 Unit cell dimensional and associated dielectric constant change for $BaTiO_3$ as a function of temperature.[14]

for breakdown. Acceptor solubility is generally limited to <5 mol%. In $BaTiO_3$, acceptor dopants such as $Mn^{2+,3+}$, $Co^{2+,3+}$, $Fe^{2+,3+}$, Ni^{2+}, and Zn^{2+} are substituted on the B site. The advantage of acceptor substitutions is that they lead to lower dissipation factors and inhibited grain growth. The distortion in the smaller unit cell caused by oxygen vacancies is believed to be the primary cause of such properties.

The ion valence of donor-type impurity atoms are higher than that of the constituent atoms, and A site vacancies are introduced. In perovskite $BaTiO_3$, donor atoms are known to suppress the peak dielectric and piezoelectric properties. This is believed to be a result of a compensating valence change of some of the Ti^{+4} to Ti^{+3}, because Ba is not volatile. In lead perovskites, such as lead zirconate titanate (PZT) or lead titanate (PT), it is believed that the excess lead created by the vacancies is allowed to leave the structure because of its

Downloaded from Digital Engineering Library @ McGraw-Hill (www.digitalengineeringlibrary.com)
Copyright © 2004 The McGraw-Hill Companies. All rights reserved.
Any use is subject to the Terms of Use as given at the website.

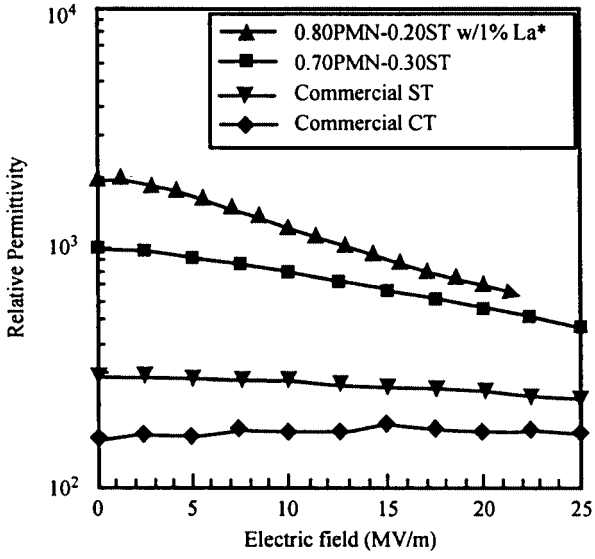

Figure 3.18 Permittivity vs. DC field for doped PMN, ST, and CT dielectrics.

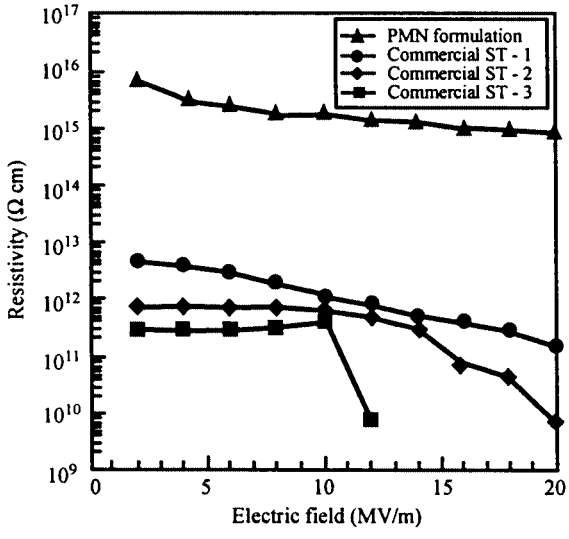

Figure 3.19 Resistivity vs. field for doped PMN and ST dielectrics.

high volatility so that the stoichiometry corrects itself. In these compounds, the peak dielectric constant and the piezoelectric properties are higher.

In $BaTiO_3$, Nb^{5+}, Ta^{5+}, and W^{6+} are substituted on the B site. Bi^{3+}, La^{3+}, or Nd^{3+} is used on the A site. The properties in this case are generally explained by increased domain wall motion resulting from the A site vacancy. The ease with which these domains will switch results in a low coercive field to switch

Downloaded from Digital Engineering Library @ McGraw-Hill (www.digitalengineeringlibrary.com)
Copyright © 2004 The McGraw-Hill Companies. All rights reserved.
Any use is subject to the Terms of Use as given at the website.

TABLE 3.6 Ionic Radii for Constituent and Dopant Ions

Ion	Site	Coordination number	Ionic radii, Å
Pb^{2+}	A	12	1.63
Ba^{2+}	A	12	1.74
Sr^{2+}	A	12	1.6
Ca^{2+}	A	12	1.34
Zn^{2+}	B	6	0.89
Nb^{5+}	B	6	0.78
Ti^{4+}	B	6	0.745
Li^{+}	B	6	0.88
Mg^{2+}	B	6	0.86
Fe^{3+}	B	6	0.785
Ta^{5+}	B	6	0.83
Sb^{5+}	B	6	0.75
W^{6+}	B	6	0.74

polarity and a reduced mechanical quality factor, because the domains will also move to cancel a small applied stress. The increased dielectric losses are also caused by increased domain wall losses. Lower aging rates are attributed to low residual stress as a result of the ease of domain wall movement. The higher DC resistivity is the result of the excess electrons countering p-type conduction.

The decrease in permittivity at high electric fields, dielectric saturation, is especially problematic in Class 2 dielectrics containing ferroelectric phases. It occurs because the ionic lattice distortion that produces the polarization has its limits. Tables 3.8 through 3.10 show typical capacitor formulations are used to achieve NPO, X7R, and Z5U performance, respectively.

3.4 Electromechanical Ceramics

Electromechanical materials are an interesting family of substances used for their ability to generate an electrical signal from a mechanical stimulation (passive devices) or generate mechanical displacements from electrical inputs (active devices). Passive devices include sensors such as sonar hydrophones, which give electrical signals as the sensor is stressed by sound waves. Advanced materials have been developed with very high electromechanical coefficients, enabling highly sensitive devices. New manufacturing processes

Downloaded from Digital Engineering Library @ McGraw-Hill (www.digitalengineeringlibrary.com)
Copyright © 2004 The McGraw-Hill Companies. All rights reserved.
Any use is subject to the Terms of Use as given at the website.

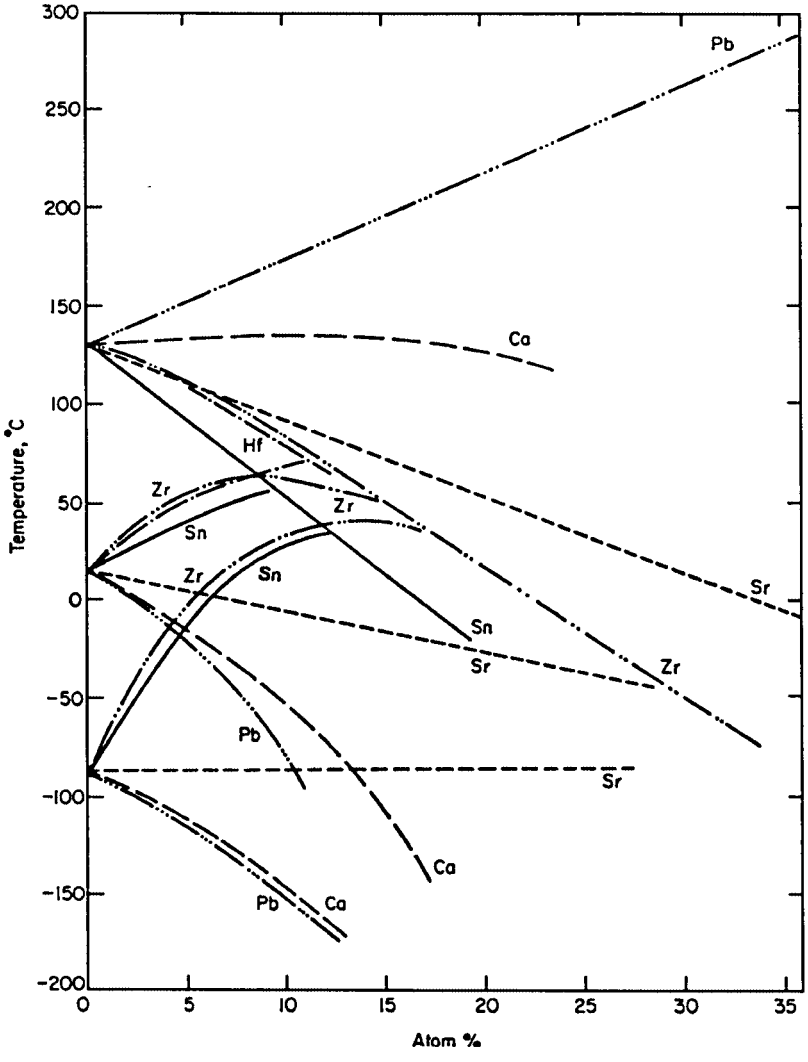

Figure 3.20 Effect of isovalent substitutions on the transition temperature of $BaTiO_3$ ceramic.[13]

allow complex arrays, composites, and multilayer stacks to be fabricated, further improving signal resolution. Other passive applications for electromechanical materials are ultrasonic sensors in medical devices and sensors in vibration-cancellation devices such as active suspensions in automobiles.

Active applications include microdisplacive devices and sonic projectors that output mechanical displacements as a result of applied electrical inputs. The high displacements, coupled with the high stiffness of ceramic electromechanical materials, allows generation of high forces. This allows vibration cancellation of relatively massive structures or generation of significant sonar source levels. Other active applications for electromechanical materials are actuators

Downloaded from Digital Engineering Library @ McGraw-Hill (www.digitalengineeringlibrary.com)
Copyright © 2004 The McGraw-Hill Companies. All rights reserved.
Any use is subject to the Terms of Use as given at the website.

TABLE 3.7 Substitution Effects on Dielectric and Piezoelectric Properties

Property	Isovalent substitution	Acceptor substitution	Donor substitution
Curie temperature	Lower	Higher	Lower
Dielectric constant	Higher	Lower	Higher
Dielectric loss	Lower	Lower	Higher
Electrical resistivity		Lower	Higher
Coercive force		Higher	Lower
Remnant polarization		Lower	Higher
Piezoelectric coefficient		Lower	Higher
Aging	Higher	Lower	Lower
Coupling coefficient		Lower	Higher
Mechanical quality factor		Higher	Lower
Elastic compliance	Lower	Lower	Higher
Strain hysteresis		Lower	Higher
Hysteresis squareness	Lower	Lower	Higher

TABLE 3.8 Formulations for NPO Capacitors

	Composition, wt%		
	1	2	3
$BaTiO_3$	41–49	39–47	15–21
TiO_2	48–54	41–47	26–34
ZrO_2		8–13	
$Nd(CO_3)_4$			59–45
Other	3–7	2–5	Small
k' (25°C, 1 kHz)	35	30	62
tan δ	<0.002	<0.002	<0.002

used for precision positioning; pumps; vibration cancellation; loudspeakers; resonators and filters for radios and televisions; and ultrasonic generators for medical devices, milling, and cleaning. These applications range from the scale of semiconductor processing for electromechanical switches or miniature arrays to several-ton transducer arrays used in active sonar.

Downloaded from Digital Engineering Library @ McGraw-Hill (www.digitalengineeringlibrary.com)
Copyright © 2004 The McGraw-Hill Companies. All rights reserved.
Any use is subject to the Terms of Use as given at the website.

TABLE 3.9 Formulations for X7R Capacitors

	Composition, wt%			
	1	2	3	Comment
$BaTiO_3$	90–97	85–92	86–94	Base material
$CaZrO_3$	2–5	4–8		Shifter
$BaCO_3$	0–5			Stoichiometry adjustment
$SrTiO_3$		3–6		Shifter
Bi_2O_3			5–10	Depressor, flux
Other	2–5	1–4	2–6	
k' (25°C, 1 kHz)	1600–2000	1800	1400–1500	
tan δ	<0.025	<0.025	<0.015	

TABLE 3.10 Formulations for Z5U Capacitors

	Composition, wt%			
	1	2	3	Comment
$BaTiO_3$	84–90	65–80	72–76	Base material
$CaZrO_3$	8–13			Shifter
$MgZrO_3$	0–3			Depressor
$SrTiO_3$		7–11	5–8	Shifter
$CaTiO_3$		7–11	4–6	Depressor
$BaZrO_3$		7–11	7–10	Shifter
$CaSnO_3$			2–4	Shifter
Other	1–3	8–13	0–3	
k' (25°C, 1 kHz)	5700–7000	5500–6500	11,500–13,000	
tan δ	≤0.03	≤0.03	≤0.03	

3.4.1 Piezoelectrics

The piezoelectric effect was first discovered in 1880 by Pierre and Jacques Curie in naturally occurring crystals such as quartz and Rochelle salt. The first significant application for piezoelectrics occurred during World War I, when Langevin developed a means of generating acoustic waves in water for signal-

Downloaded from Digital Engineering Library @ McGraw-Hill (www.digitalengineeringlibrary.com)
Copyright © 2004 The McGraw-Hill Companies. All rights reserved.
Any use is subject to the Terms of Use as given at the website.

ing and detection of German submarines. These early forms of active sonar employed the use of piezoelectric quartz. In 1920, ferroelectric behavior was discovered in Rochelle salt by Joseph Valasek. Because of its large piezoelectric effect, Rochelle salt became widely used in microphones, phonographs, loudspeakers, recorders, and oscillographs. In 1930, Sawyer and Tower developed a circuit to record the hysteresis behavior of this ferroelectric. The first polycrystalline piezoelectrics, based on $BaTiO_3$, were discovered by VonHippel and others in the mid 1940s. R. B. Gray and S. Roberts were among the first to develop piezoelectric ceramics by "poling" ferroelectrics. The ferroelectric behavior of lead titanate was discovered in 1950. In 1952, piezoelectric behavior was discovered in tungsten-bronze structure lead niobate. In the mid 1950s, PZT (lead zirconate titanate) was developed and became the most widely used piezoelectric ceramic to date. The first piezoelectric polymer, polyvinyledene fluoride, was developed in 1969 by stretching it under high fields. More recently, a variety of complex niobate based piezoelectrics with very high piezoelectric coefficients have been developed. Multilayer and thin film processing have dramatically expanded the applications of this important group of materials.

3.4.2 Ferroelectrics

Polycrystalline piezoelectric materials exhibiting ferroelectric behavior are the center of attention, because they can be readily formed into various shapes and sizes using conventional processing. Ferroelectricity is the spontaneous alignment of dipoles as a result of their mutual interaction. At lower temperatures, the electric dipoles in a ferroelectric material create a local field that is stronger than the thermal energy required for randomization and spontaneous polarization results. Without external applied forces, the dipoles align in regions or domains. The various domains are then oriented along different crystallographic directions resulting in the lowest (strain) energy state and a net-zero polarization for the fired ceramic compounds of the perovskite structure shown in Fig. 3.16. These include $Pb(Zr, Ti)O_3$ (PZT), $BaTiO_3$, $Pb(Mg_{1/3}Nb_{2/3})O_3$ PMN, and $Pb\ (Zn_{1/3}Nb_{2/3})O_3$ PZN. In addition, tungsten-bronze structures such as (Sr, Ba) Nb_2O_6, $PbNb_2O_6$, and $LiNb_2O_6$ are often ferroelectric.

These compounds are typically cubic and therefore paraelectric at high temperature. As the material is cooled, a change to a ferroelectric phase occurs at the Curie temperature, T_C, and spontaneous polarization results. The perovskite ferroelectric phase is typically tetragonal or rhombohedral. Most of the perovskite compounds readily form solid solutions with one another, allowing substantial substitution to achieve optimal performance. Often, solid solutions are formed with perovskites of different crystal structures, which results in a composition range wherein two different ferroelectric phases are present—the morphotropic phase boundary. Figure 3.21 shows the effect of solid solutions between ferroelectric $PbTiO_3$ and antiferroelectric $PbZrO_3$. It is generally desirable to develop compositions near the morphotropic phase boundary because, at this region, the dielectric and piezoelectric properties are maximized, as shown in Fig. 3.22.

Downloaded from Digital Engineering Library @ McGraw-Hill (www.digitalengineeringlibrary.com)
Copyright © 2004 The McGraw-Hill Companies. All rights reserved.
Any use is subject to the Terms of Use as given at the website.

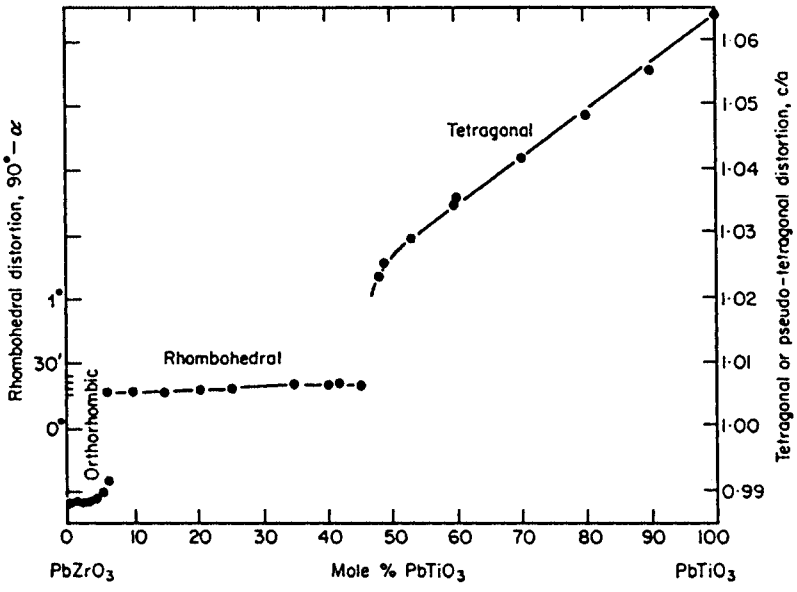

Figure 3.21 Unit cell dimension change vs. temperature in the PZT system.[13]

When a ferroelectric is cooled through its Curie region, the cubic lattice deforms to a polar phase. The polarization orients into regions, or domains, so as to minimize intergranular stresses. The dipoles of adjacent domains align along crystallographic axes.

Figure 3.23 shows how polarization changes with applied field in a ferroelectric material. At low initial fields, polarization increases nearly linearly with field. As higher fields are applied, the domains begin to align with the field and grow. The polarization increases more rapidly. Ultimately, a significant portion of the domains are aligned with the field, and little additional polarization results as the field is raised. The highest polarization achieved at high fields (>2 MV/m) with all dipoles aligned is the saturation polarization, P_S. When the external electric field is released, most of the dipole alignment remains, and there is a remnant polarization, P_R. The domain alignment can again be randomized to a net-zero polarization by reversing the polarity of the field. The field require to achieve this is the coercive field, E_C. As fields of opposite polarity are increased, the domains again align with the field, resulting in polarization of opposite polarity. This behavior under applied AC fields results in the hysteresis loop shown in Fig. 3.23. The hysteresis in the P-E relationship indicates energy lost in moving domain boundaries. The process of applying a high electric field to a polycrystalline ferroelectric to obtain a high remnant polarization, *poling*, is necessary to achieve strong piezoelectric behavior.

The piezoelectric expansion or contraction in the direction of an applied field results from alignment and stretching of dipoles in the material with the applied field. The expansion is linear and directly proportional to the magnitude

Downloaded from Digital Engineering Library @ McGraw-Hill (www.digitalengineeringlibrary.com)
Copyright © 2004 The McGraw-Hill Companies. All rights reserved.
Any use is subject to the Terms of Use as given at the website.

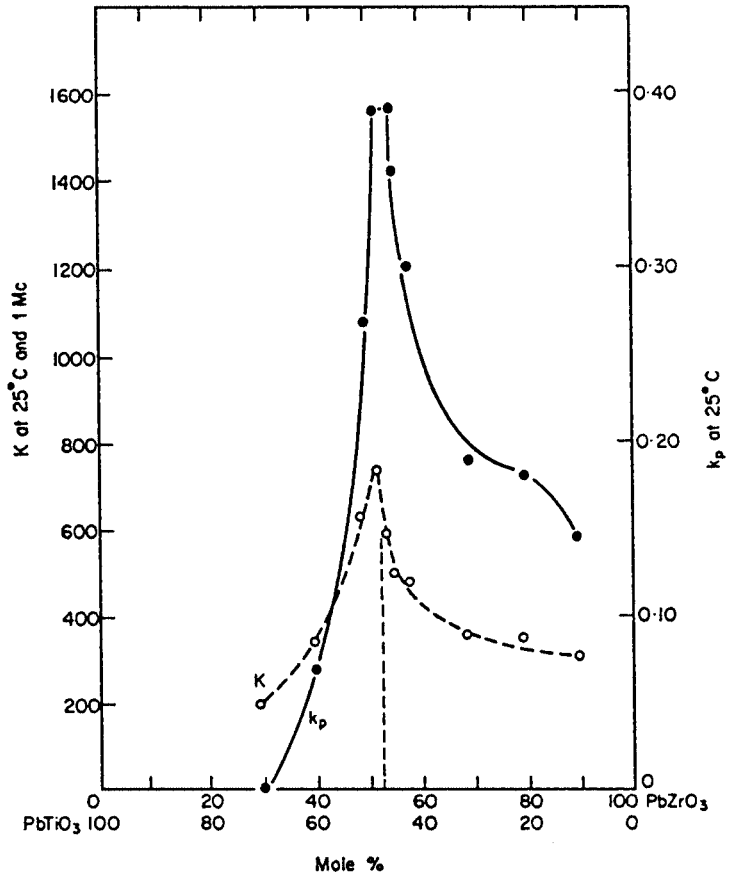

Figure 3.22 Dielectric constant and planar piezoelectric coupling coefficient for compositions near the morphotropic phase boundary in PZT.[13]

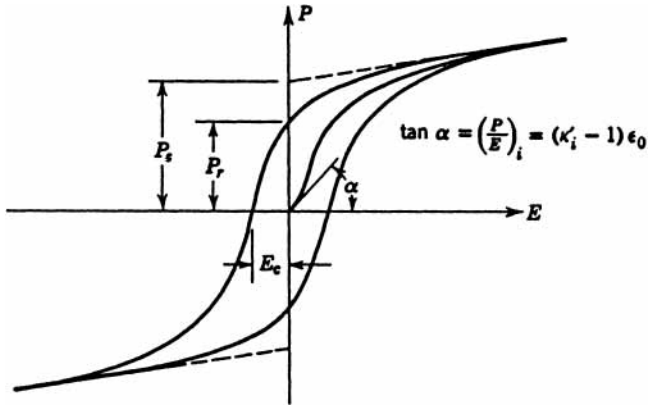

Figure 3.23 Electronic polarization vs. field for a ferroelectric material.[14]

Downloaded from Digital Engineering Library @ McGraw-Hill (www.digitalengineeringlibrary.com)
Copyright © 2004 The McGraw-Hill Companies. All rights reserved.
Any use is subject to the Terms of Use as given at the website.

and polarity of the applied field. Piezoelectric ceramics have reorientable dipoles; therefore, dipolar reorientation may occur if energy is added by electric fields, heat, or pressure. Reorientation by field (poling) is an integral part of the fabrication of a piezoelectric ceramic. Poling creates the initial remnant dipolar orientation in the material. Because all of the reorientation mechanisms involve energy inputs, there is an intrinsic energy loss during any reorientation; this energy loss is proportional to the hysteresis.

3.4.3 Electrostrictors

More recent developments of complex perovskite structures has resulted in a new class of electromechanical materials, *electrostrictors*. Purely electrostrictive materials are paraelectric and centrosymmetric; that is, they do not possess a polar axis and are typically cubic. The electrostrictive materials of most interest are ferroelectrics that are operated above or near their transition temperatures. The electrostrictive effect is a second-order phenomenon whereby an applied electric field results in a lattice distortion and mechanical distortion in the material.

During the 1980s, substantial research on electrostrictive materials, particularly PMN-based materials, occurred in the U.S. and Japan. Significant improvements in electrostrictive materials were made, achieving a pyrochlore-free perovskite near the morphotropic phase boundary. Researchers at Martin Marietta Laboratories[4] formed the perovskite phase using a sol-gel process and a mixed oxide process with barium titanate (BT) and strontium titanate (ST) additions. In particular, the base composition $0.855Pb(Zn_{0.33}Nb_{0.67})$–$0.195PbTiO_3$–$0.05BaTiO_3$, has yielded some of the highest effective piezoelectric coefficients available (i.e., low-field d_{33} = 500 to 750 pC/N).

The field induced strain in piezoelectric and electrostrictive materials is on the order of 10^{-4} to 10^{-3} and is a function of applied mechanical stresses, electric fields, and thermal expansion. Under isothermal conditions, the net elastic strain in a material is given by

$$\varepsilon_{ij} = S_{ijkl}\sigma_{ij} + g_{ijk}P_k + Q_{ijkl}P_kP_l + \ldots = S_{ijkl}\sigma_{ij} + d_{ijk}E_k + M_{ijkl}E_kE_l + \ldots \quad (3.5)$$

where the $S_{ijkl}\sigma_{ij}$ term describes the mechanically induced strain, the $g_{ijk}P_k$ term describes the first-order piezoelectric response, and the second-order $Q_{ijkl}P_kP_l$ term describes the electrostrictive contributions.

Figure 3.24 shows the transition region for a typical polycrystalline ferroelectric material. The material is cubic and paraelectric, and it exhibits purely electrostrictive behavior well above the transition region and piezoelectric, rhombohedral, or tetragonal below the transition. In the transition region, polarization is maximized as demonstrated in Eq (3.5).

Observing the strain response as a function of applied field across the transition region shows quadratic, low-hysteresis behavior at higher temperatures (Fig. 3.25). The dielectric permittivity is maximized at the transition region along with the dielectric loss. The polarization versus field plots show no hysteresis and no remnant polarization well above T_C. In pure electrostrictors, the first-order strain term in Eqs. (3.5) and (3.7) becomes negligible, and the

Downloaded from Digital Engineering Library @ McGraw-Hill (www.digitalengineeringlibrary.com)
Copyright © 2004 The McGraw-Hill Companies. All rights reserved.
Any use is subject to the Terms of Use as given at the website.

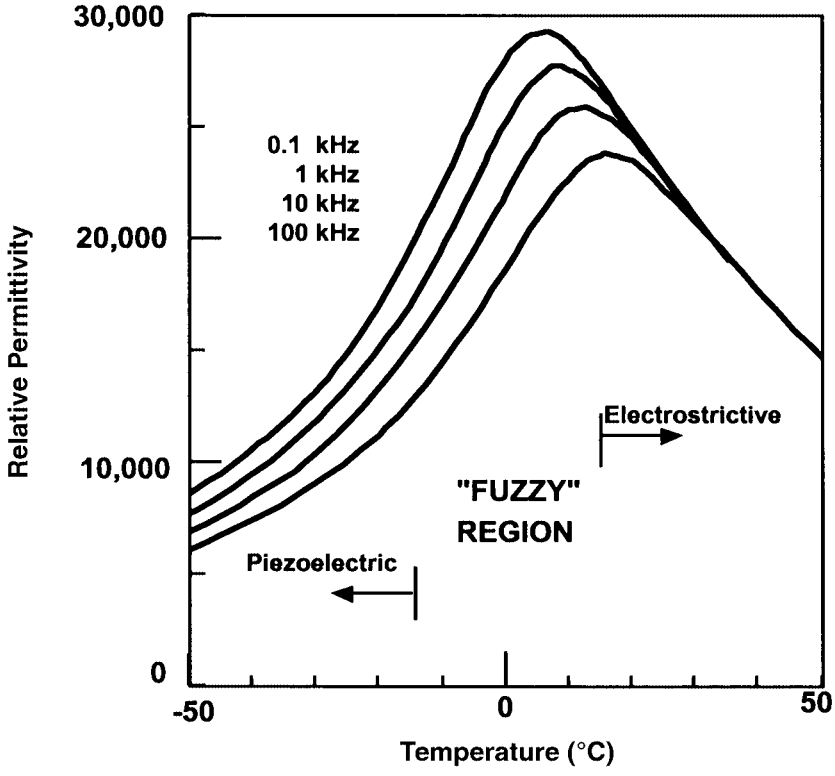

Figure 3.24 Schematic view of the weal-field dielectric properties of the relaxor ferroelectrics of interest.[22]

relation of strain to polarization or field becomes quadratic (at low fields). Electrostrictive strain is a result of a lattice distortion with applied field. Expansion of the material is observed in the direction of the applied field, regardless of the field polarity. Increasing polarization, strain, and hysteresis are observed as the material is cooled. Polarization and field-induced strain are maximized near the transition region. Ultimately, significant effects of the polar axis switching are observed; that is, large hysteresis and contraction with alternating fields (the butterfly response). Piezoelectrics expand under fields of the same polarity as the poling field but also contract under negative fields. Table 3.11 shows the properties of piezoelectric standards as well as common piezoelectric and electrostrictive materials.

3.4.4 Materials

"Hard" piezoelectric materials, Type I–IV, are typically formulated to operate well below the transition region. The piezoelectric phase is highly stable and typically formulated for high coercive force and minimal domain wall movement (minimal aging). This results in a material wherein the d coefficient is lower, but the hysteresis is relatively small as a result of minimal domain wall movement. This type of material is the most common electromechanical mate-

Downloaded from Digital Engineering Library @ McGraw-Hill (www.digitalengineeringlibrary.com)
Copyright © 2004 The McGraw-Hill Companies. All rights reserved.
Any use is subject to the Terms of Use as given at the website.

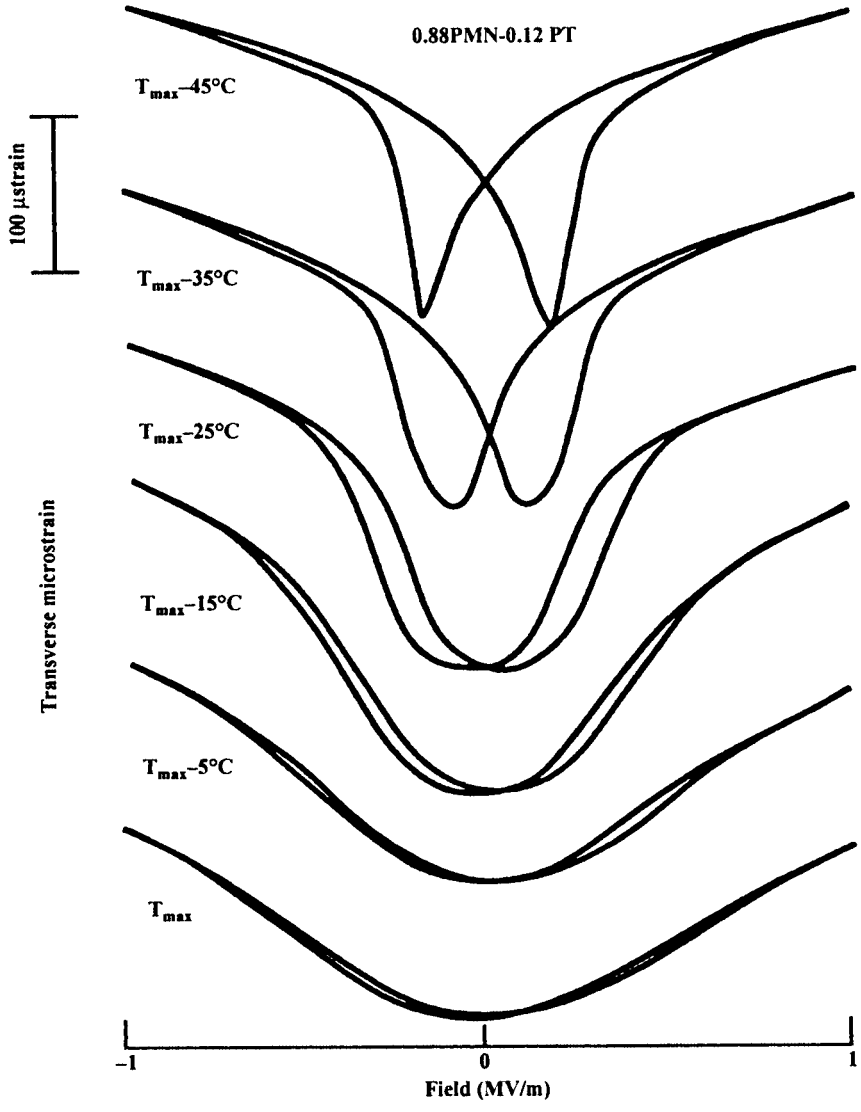

Figure 3.25 Strain vs. field and temperature for a ferroelectric, showing piezoelectric response well below T_C and a more quadratic electrostrictive response as T_C is approached.[22]

rial, used in passive and active sonar as well as in many commercial applications where high induced force and stable response are needed.

"Softer" piezoelectrics, Type V and VI, are formulated to operate closer to the transition region, achieving higher strains with higher polarization. Typically, this results in corresponding higher hysteresis and dielectric losses, and they are more susceptible to pressure depoling and aging. These materials are attractive for high sensitivity passive transducers and actuator applications where high field induced strains are desired.

Downloaded from Digital Engineering Library @ McGraw-Hill (www.digitalengineeringlibrary.com)
Copyright © 2004 The McGraw-Hill Companies. All rights reserved.
Any use is subject to the Terms of Use as given at the website.

Ceramics and Glasses

TABLE 3.11 Piezoelectric Standards and Properties of Selected Materials

Powder	Curie temperature (°C)	Room-temperature permittivity	Aging rate	d_{33} or effective d_{33} (pC/N)	Hysteresis (%)*
Navy Standards					
Type I	325	1275 ± 12.5%	–4.5 ± 2.0%	–4.5 ± 2.0%	1–3
Type II	350	1725 ± 12.5%	–1.5± 0.7%	–1.5± 0.7%	
Type III	325	1025 ± 12.5%	–4.0 ± 1.5%	–4.0 ± 1.5%	
Type IV	115	1275 ± 12.5%	–1.5 ± 0.5%	–1.5 ± 0.5%	
Type V	240	2500 ± 12.5%	–2.0 ± 1.0%	–2.0 ± 1.0%	
Type VI	180	3250 ± 12.5%	–2.0 ± 1.0%	–2.0 ± 1.0%	
MMC (129) PMN	25	23,000		760	1–4
MMC (100) PMN	33	18,000		850–1000	1–3
MMC PZN-PT-BT	144	3000–3500		650	10–11
0.91 PZN-0.09PT, single crystal	178	2200–4100		1500	
$BaTiO_3$	120	1400–2000		191	
$PbTiO_3$	500				
$Pb(Ti_{.48}Zr_{.52})O_3$				223	
U5H-32† PZT	195	2500		600	11–12

*Measurement taken at 20°C
†Ultrasonics Corporation, South Plainfield, NJ

Soft electrostrictors operate just above the transition region, where strains are maximized as a result of contributions of both piezoelectric and electrostrictive effects. This combined effect results in materials that achieve the highest electromechanical energy density and possess the highest degree of sensitivity. However, these materials are highly temperature sensitive and require high-power drivers in active roles because of the corresponding high capacitance and power dissipation.

Hard electrostrictors are formulated for low hysteresis and therefore operate well above the transition region where pure electrostrictive behavior is observed. These materials have excellent *shape memory* because of their low hysteresis and are well suited for precision positioning applications such as deformable mirrors.

Table 3.12 shows the properties of various piezoelectric transducer materials. Generally, materials with lower piezoelectric coefficients have significantly higher coercive fields, resulting in a more stable piezoelectric response.

Downloaded from Digital Engineering Library @ McGraw-Hill (www.digitalengineeringlibrary.com)
Copyright © 2004 The McGraw-Hill Companies. All rights reserved.
Any use is subject to the Terms of Use as given at the website.

TABLE 3.12 Properties of Piezoelectric Transducer Materials

Material	Dielectric Constant	d_{33} (pC/N)	d_{31} (pC/N)	g_{33} (10^3 m^2/C)	$d_h g_h$	k_p
$PbNb_2O_6$	225	85	–10		2300	
$Pb_{0.5}Ba_{0.5}Nb_2O_6$		220	–90			
$PbTiO_3$		51	–4			
$BaTiO_3$		190	–79	13		0.36
PZT		223	–93.5			0.52
PZT	1800	450	–205		100	
.855PZN-.095PT-.05BT	3000–3500	540	–228		279	
.873PZN-.097PT-.03BT	1825	440	–196		143	
PLZT 2/65/35		150		23		0.45
PLZT 7/60/40		710		22		0.72
PLZT 7/55/45		405		15		0.56

In most electromechanical materials, dopants are used to tailor the properties for specific applications. Isovalent substitutions are often used to modify the dielectric properties of these materials. For instance, Ba^{2+} or Sr^{2+} substitution for Pb^{2+} in perovskite and tungsten-bronze structures or Sn^{4+} for Zr^{4+} in PZT. The perovskite and tungsten-bronze structures will allow significant substitution with isovalent ions of similar size.

The $Pb(Zn_{1/3}Nb_{2/3})O_3$ (PZN) materials are cubic above the transition temperature (T_C), 140°C, and undergoes a diffuse phase transition to rhombohedral as it is cooled below T_C. PT is cubic above its Curie temperature of 490°C and undergoes a diffuse phase transition to tetragonal as it is cooled below T_C. The resulting solid solution of these results in a morphotropic phase transition between the rhombohedral and tetragonal phases at 9 percent PT. Additions of barium titanate (BT) to PZN-PT allow formation of pure perovskite near the morphotropic phase boundary where properties are maximized.

The ferroelectric phase of tungsten-bronze structure $PbNb_2O_6$ is metastable; that is, it normally exists only at high temperatures, >1200°C. However, by doping and rapidly cooling from high temperature, the ferroelectric tetragonal phase can be retained to low temperatures.

Piezoelectrics have been the sensing and broadcasting element of underwater acoustics since its inception. Passive sensors are designed to detect acoustic signals by converting pressure waves or vibrations into electrical signals. Ignoring temperature, bias stress, and electrostrictive effects, Eq. (3.5) reduces to

$$\varepsilon_{ij} = g_{ijk}P_k = d_{ijk}E_k \tag{3.6}$$

Downloaded from Digital Engineering Library @ McGraw-Hill (www.digitalengineeringlibrary.com)
Copyright © 2004 The McGraw-Hill Companies. All rights reserved.
Any use is subject to the Terms of Use as given at the website.

Ceramics and Glasses

for a pure piezoelectric material, where

ε_{ij} = strain
P_k = dielectric polarization vector
E_k = electric field vector
g_{ijk}/d_{ijk} = piezoelectric coefficients

The piezoelectric charge coefficients, d_{ijk}, are generally expressed using condensed subscripts, such as d_{33} and d_{31}, where the first subscript refers to the electric field direction or direction of polarization, and the second subscript refers to the stress or strain direction.

3.4.5 Applications of electromechanical materials

By definition, electromechanical materials provide a coupling between electrical and mechanical energy. The mechanical displacements are relatively small, but these materials can generate significant electrical and mechanical forces.

Actuators generate mechanical displacements with electrical inputs for applications that include precision positioning devices, miniature motors, fuel injectors, printer heads, precision machining, noise cancellation, and optical devices such as deformable mirrors. A variety of methods have been developed to achieve practical displacements with practical drive voltages. The practical maximum displacement for an electromechanical ceramic is 0.1 percent at fields of 1 to 2 MV/m. Therefore, 1 mm of material is needed to achieve a displacement of 1 μm. A monolithic block of material would require 1 to 2 kV to achieve this displacement. Multilayer actuators as shown in Fig. 3.26 use ceramic capacitor processing and designs to reduce voltage requirements. The drive voltage required for a multilayer design is reduced by a factor equal to the number of layers. For instance, if the 1-mm thick actuator consisted of ten 0.1-mm layers, the drive voltages for the 1-μm displacement would be reduced to 100 to 200 V.

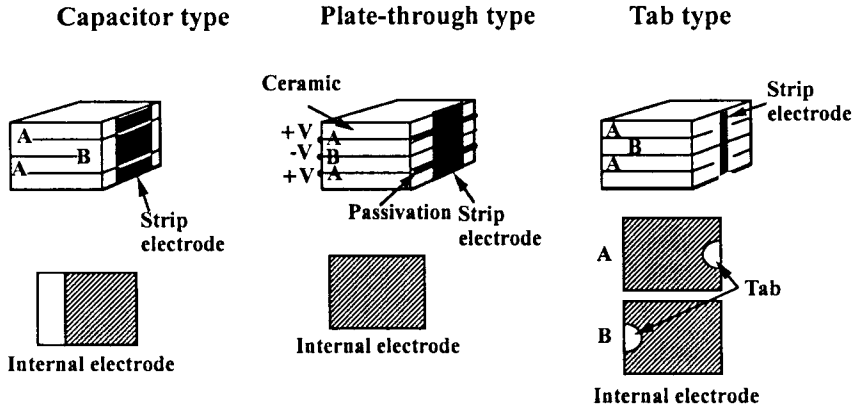

Figure 3.26 Actuator electrode and termination configurations.[22]

Downloaded from Digital Engineering Library @ McGraw-Hill (www.digitalengineeringlibrary.com)
Copyright © 2004 The McGraw-Hill Companies. All rights reserved.
Any use is subject to the Terms of Use as given at the website.

The Toyota Electronically Modulated Suspension (TEMS) uses piezoelectric sensors and actuators in a vibration cancellation role shown in Fig. 3.27. The system senses the road vibrations with a five-layer piezoelectric sensor. When rough roads or hard turns are encountered, the sensor is stressed and generates an electronic signal. The signal is amplified by a control unit that outputs a voltage to the 88-layer piezoelectric actuator. The actuator expands up to 50 μm on a hydraulic motion amplifier, which expands to 2 mm. This displacement stiffens the damping force of the shock absorbers, all within a 20-ms period.

Acoustic transducers convert electrical inputs into acoustic signals, i.e., projectors, or convert acoustic signals into electrical signals, i.e., sensors. Underwater acoustics applications have driven the development of piezoelectric ceramics. Hydrophones, such as those shown in Fig. 3.28, are the passive sensing devices in underwater acoustic applications. Hydrophones take advantage of the direct piezoelectric effect; that is, acoustic inputs in the form of pressure changes result in an electrical output. Hydrophones are designed for collecting inputs from a broad frequency band, 0.1 to 100 kHz. The higher frequencies allow higher resolution but are rapidly dissipated in water. Lower frequencies are therefore used for longer-range detection.

In sonar projector applications, acoustic power is applied to the water by an active surface. In most active sonar applications, the device operates at a natural resonant frequency so as to minimize the power requirements for large displacements. Projectors are the active devices for sound generation in underwater acoustics. Sonar projectors take advantage of the converse piezoelectric effect by converting large electrical signal inputs into mechanical outputs in the form of pressure changes, or sound waves. Projectors are typically designed to operate at resonance for maximum source level; therefore, the operating frequency band of individual devices is narrow. Often, arrays of projectors operating at different frequencies are used to produce broadband acoustic sources.

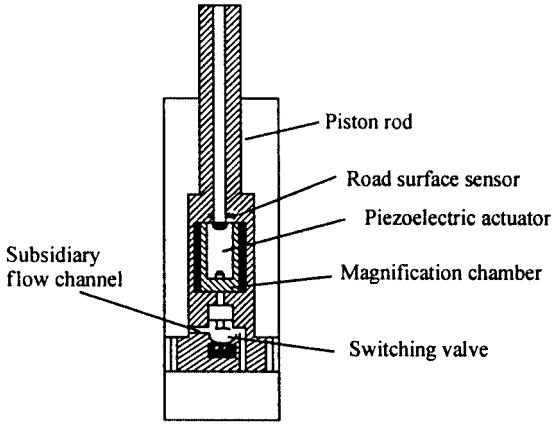

Figure 3.27 Schematic of the Toyota Electronically Modulated Suspension (TEMS) shock absorber.[21]

Downloaded from Digital Engineering Library @ McGraw-Hill (www.digitalengineeringlibrary.com)
Copyright © 2004 The McGraw-Hill Companies. All rights reserved.
Any use is subject to the Terms of Use as given at the website.

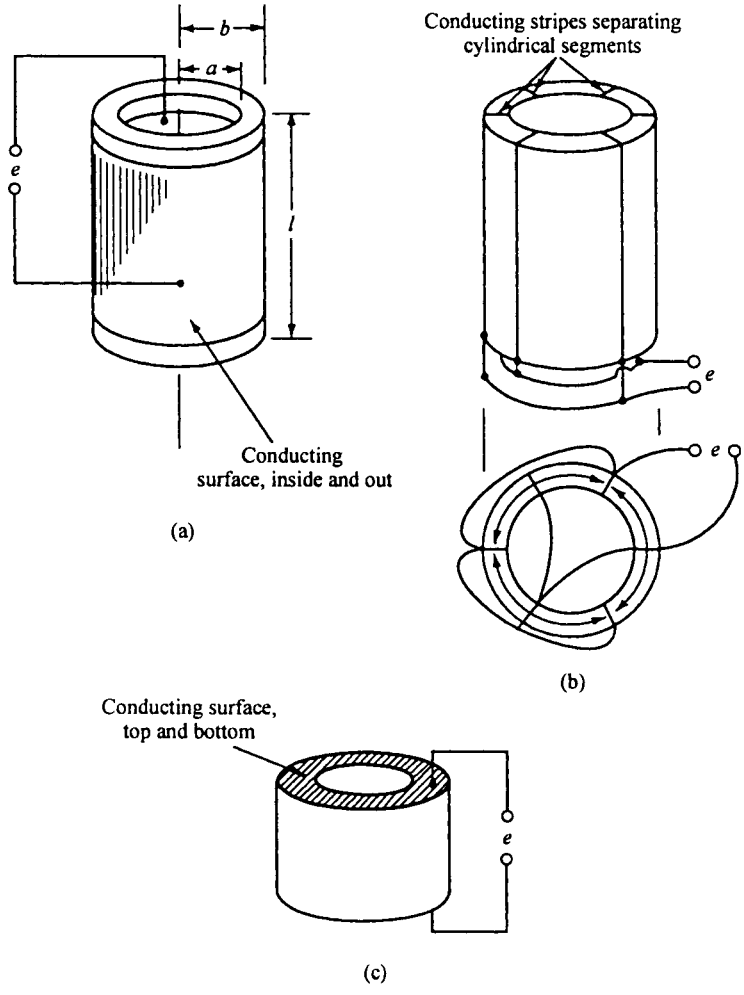

Figure 3.28 Ceramic cylindrical hydrophones: *(a)* radial mode, *(b)* tangential mode, and *(c)* longitudinal mode.[6]

Two types of sonar projectors are shown in Fig. 3.28. The Tompilz projector uses a stack of longitudinally poled piezoelectric slabs. The slabs are doughnut shaped so that a center bolt can be used to connect the head mass to the tail mass and prestress the multilayer ceramic stack. The slabs typically are metallized with thick film, fire-on metals with thicker metal shims separating slabs for better current carrying capability. The multilayer stack is electrically connected in parallel.

Flextensional transducers also contain a longitudinally poled stack of piezoelectric slabs, electrically connected in parallel and inserted into an elliptical metal ring. The metal ring is designed to have a center opening somewhat smaller than the ceramic stack so that the metal ring must be compressed along the short axis to insert the stack. This is an effective method for pre-

Downloaded from Digital Engineering Library @ McGraw-Hill (www.digitalengineeringlibrary.com)
Copyright © 2004 The McGraw-Hill Companies. All rights reserved.
Any use is subject to the Terms of Use as given at the website.

stressing the multilayer stack. The approximately 3:1 aspect ratio of the flextensional transducer amplifies the mechanical displacement along the minor axis. The flextensional transducer obeys conservation of energy laws, so the 3:1 amplitude improvement is at the expense of a 3:1 reduction in the force generated along the minor axis direction.

Ultrasonic transducers for medical imaging utilize piezoelectric ceramics and composites to generate an ultrasonic beam that can penetrate soft tissue. The same transducer then picks up the reflections off internal structures, organs, fetuses, and so on. These transducers most often consist of square cross-section piezoelectric rods in a polymer matrix. These are formed by a dice-and-fill process. Figure 3.29 shows various piezoelectric-polymer composites used to optimize the performance for various applications. The diced 1-3 composite is typically used in ultrasonic transducer applications.

3.5 Electro-optic materials

The electro-optic effect is simply a change in optical properties, namely refractive index, with an applied field. Changes in refractive indices are relatively small, on the order of 10^4; however, this is sufficient to modulate the phase or intensity of transmitted light. A half-wavelength change in phase is sufficient to modulate polarized light from 0 to 100 percent transmission.

The first observation of natural optical anisotropy was made in 1669, by Bartolinius, in calcite crystals, in which light travels at different velocities depending on the direction of propagation relative to the crystal structure. The electro-optic effect, electric field-induced anisotropy, was first observed in

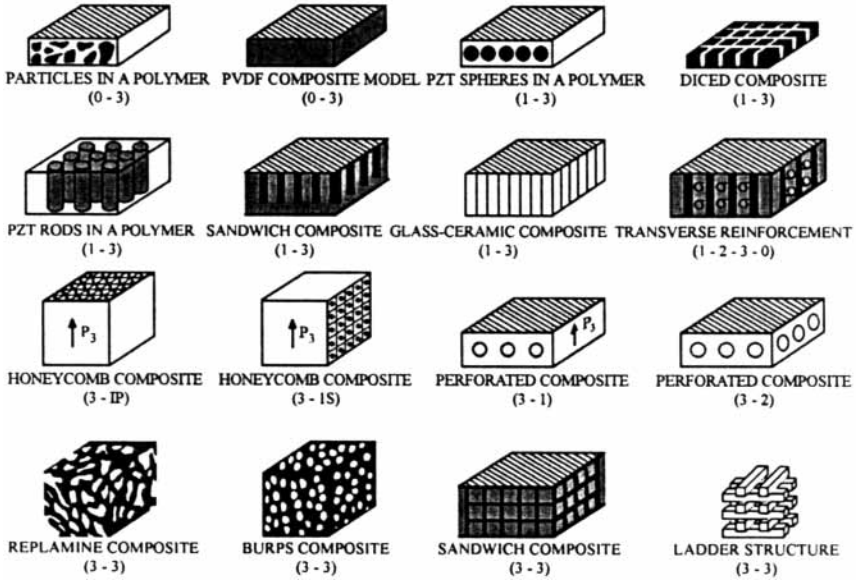

Figure 3.29 Piezoelectric-polymer composite configurations used to optimize ultrasonic transducer and hydrophone performance.[16]

Downloaded from Digital Engineering Library @ McGraw-Hill (www.digitalengineeringlibrary.com)
Copyright © 2004 The McGraw-Hill Companies. All rights reserved.
Any use is subject to the Terms of Use as given at the website.

glass, in 1875, by J. Kerr. Kerr found a nonlinear dependence of refractive index on an applied electric field. The "Kerr effect" is used to describe the quadratic electro-optic effect observed in isotropic materials. The linear electro-optic effect was first observed in quartz crystals in 1883, by W. Rontgen and A. Kundt. Pockels broadened the analysis of this relationship in quartz and other crystals, which led to the term *Pockels effect* to describe linear behavior. In the 1960s several developments in the areas of materials and processing led to the concept of electro-optic ceramics. The development of hot-pressing techniques enabled the fabrication of fully dense ceramic bodies with a high degree of transparency. The first electro-optic ceramics developed at Sandia National Laboratories were based on the solid solution of lead zirconate-lead titanate (PZT). By 1969, the first transparent ceramics of lanthanum-doped PZT (PLZT) were fabricated. G. Hartling and C. Land have extensively studied the electro-optic properties of PLZT and defined the composition dependence. The first single crystals of $Sr_xBa_{1-x}Nb_2O_6$ were fabricated in 1966 by A. Ballman and H. Brown. The large electro-optic coefficients were attractive for applications in laser modulation and deflection devices.

To sufficiently describe this effect, a review of optical properties of materials is necessary. The refractive index of a material is a measure of the reduction in the speed of light as it travels through a transparent material, that is,

$$n = \frac{c}{c_{material}} \tag{3.7}$$

where c = the speed of light in vacuum, 3×10^8 m/s

Because $\lambda = c\upsilon$, a reduction in the speed of light results in a reduction in wavelength, λ.

The speed of light is affected as a result of the interaction with the electronic structure of the medium in which it is traveling. Materials containing large ions or negatively charge ions whose outer electrons are not so tightly bound (i.e., having high polarizability) have a stronger interaction with electromagnetic waves. In general, materials with more dense crystal structures lower the speed of light and result in higher refractive indices. The index of refraction of various transparent materials is shown in Table 3.13. Refractive index is somewhat dependent on the wavelength of the incident light. Typically, there is an increase in index at low wavelengths and a reduction at high wavelengths. Figure 3.30 shows the variation in refractive index for a variety of optical materials as a function of wavelength. The amount of light reflected or refracted at the interface between two different materials is determined by their refractive indices. The amount of light reflected at an angle equal to the incident angle is given by Fresnel's formula,

$$R = \left(\frac{n-1}{n+1}\right)^2 \tag{3.8}$$

for reflection in air.

Downloaded from Digital Engineering Library @ McGraw-Hill (www.digitalengineeringlibrary.com)
Copyright © 2004 The McGraw-Hill Companies. All rights reserved.
Any use is subject to the Terms of Use as given at the website.

TABLE 3.13 Index of Refraction for Various Transparent Materials

Material	Refractive index
Air	1.003
Soda-lime-silica glass	1.52
Fused quartz	1.46
Quartz	1.5/1.6
Calcite, $CaCO_3$	1.56/1.74
ZnSe	2.62
$SrTiO_3$	2.49
Strontium barium niobate	2.34
LA-doped lead zirconate titanate (PLZT)	2.50
$BaTiO_3$	2.40
$LiNbO_3$	2.31

The degree of refraction at the interface resulting from the change in light velocity is given by Snell's law,

$$\frac{\sin\phi_i}{\sin\phi_r} = \frac{n_2}{n_1} \tag{3.9}$$

where n_2 is the refractive index of the material through which the light is refracted. Unpolarized (white) light contains randomly oriented electric field vectors, phases, and wavelengths. Both the reflected and refracted light undergo polarization of the electric field component vibrations. When unpolarized light contacts an interface, the reflected wave will have an electric field component whose vibrations tend to polarize perpendicular to the plane of incidence. This is illustrated in Fig. 3.31. The refracted wave vibrations tend to polarize parallel to the plane of incidence.

The direction of polarization in an isotropic material is always parallel to the applied field. The velocity of light travelling in an anisotropic material is dependent on both the direction of polarization and propagation. The optic axis is the crystallographic direction in which light will propagate at a speed that is independent of the polarization plane. When the electric displacement component of light vibrates at right angles to the optic axis, regardless of direction, the ray is called *ordinary.* For rays that vibrate parallel to the optic axis, *extraordinary* waves, the speed is dependent on the direction. The difference in refractive index between that of the ordinary wave, n_o, and the extraordinary wave, n_e, is the birefringence, Δn. Birefringence is a measure of the phase difference between the ordinary and extraordinary waves. The relative impermeability of a material is given by

Downloaded from Digital Engineering Library @ McGraw-Hill (www.digitalengineeringlibrary.com)
Copyright © 2004 The McGraw-Hill Companies. All rights reserved.
Any use is subject to the Terms of Use as given at the website.

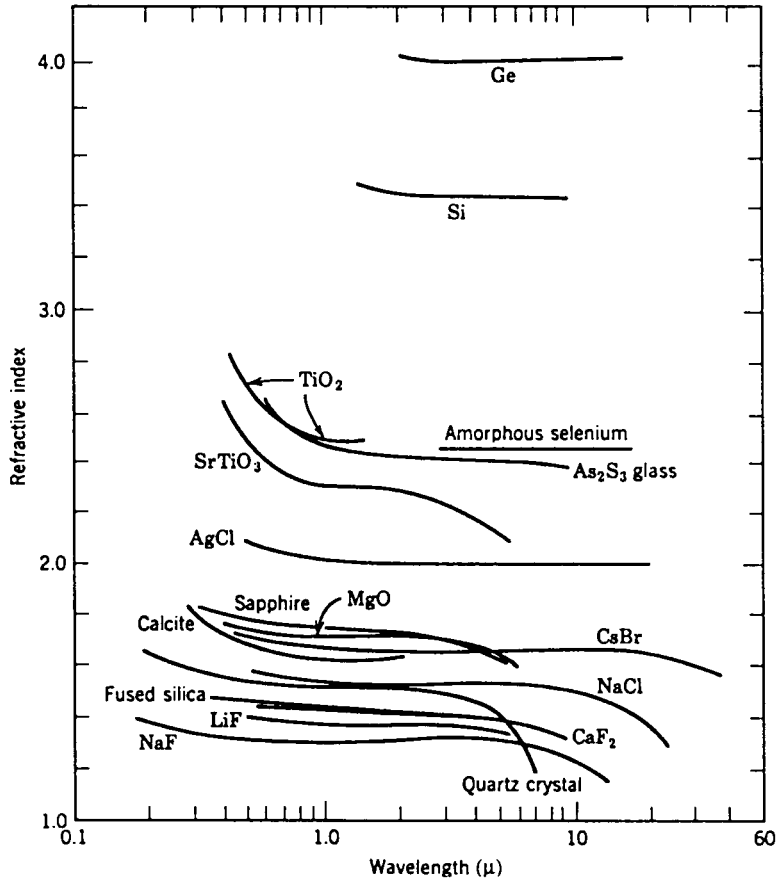

Figure 3.30 Change in refractive index with wavelength for several crystals and glasses.[14]

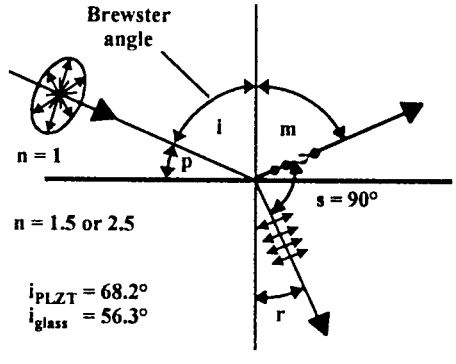

Figure 3.31 Polarization effects in unpolarized light on reflection and refraction.[16]

Downloaded from Digital Engineering Library @ McGraw-Hill (www.digitalengineeringlibrary.com)
Copyright © 2004 The McGraw-Hill Companies. All rights reserved.
Any use is subject to the Terms of Use as given at the website.

$$B_{ij} = \frac{1}{\varepsilon_r} = \frac{l}{n^2} \tag{3.10}$$

where ε_r = relative permittivity
n = refractive index for the material

In reference to the principal axes of a crystal, the relation becomes the optical indicatrix,

$$B_{ij}x_i x_j = \frac{x_1^2}{n_1^2} + \frac{x_2^2}{n_2^2} + \frac{x_3^2}{n_3^2} = 1 \tag{3.11}$$

Application of a field causes a distortion in the optical indicatrix of ΔB_{ij}. The electro-optic effect can be described in terms of the relative impermeability, ΔB_{ij}, dependence on applied field,

$$\Delta B_{ij} = r_{ijk} E_k + R_{ijkl} E_k E_l \tag{3.12}$$

where r_{ijk} = linear Pockels electro-optic coefficients
R_{ijk} = quadratic Kerr electro-optic coefficient

When a field is applied to an anisotropic crystal, the change in refractive index is

$$\Delta n = \frac{-n^3 r_c E}{2} \tag{3.13}$$

where $r_c = r_{33} - \frac{n_o^3 r_{13}}{n_e^3}$

These relationships describe the linear Pockels electro-optic effect.

When a field is applied to an isotropic crystal, the change in refractive index is

$$\Delta n = \frac{-n^3 (R_{11} - R_{12}) E^2}{2} \tag{3.14}$$

These relationships describe the quadratic Kerr electro-optic effect.

Just as the permittivity and polarization of a dielectric is dependent on the applied field, so is the refractive index; that is,

$$n = n_o + aE_o + bE_o^2 + \ldots \tag{3.15}$$

The refractive index at no applied field is represented by n_o. The aE_o component represents the linear behavior between the refractive index and applied

Downloaded from Digital Engineering Library @ McGraw-Hill (www.digitalengineeringlibrary.com)
Copyright © 2004 The McGraw-Hill Companies. All rights reserved.
Any use is subject to the Terms of Use as given at the website.

Ceramics and Glasses

electric field for materials that are noncentrosymmetric. The quadratic relationship between refractive index and applied field, the bE_o^2 term, is seen in glasses and isotropic materials. In isotropic materials, the refractive index is the same, regardless of the direction of light propagation, and the polarization state of the incident light remains unchanged. As an electric field is applied, there is distortion of the electronic structure of the crystal, and the material will then exhibit different refractive indices. Therefore, light passing through the material will split into two rays having different velocities. As the rays recombine on exiting the material, there is interference, resulting in a rotation of the polarization direction. The phase shift, or retardation, Γ, is given by

$$\Gamma = \Delta nt \tag{3.16}$$

where t is the thickness of the electro-optic material through which the light propagates.

3.6 Materials

All electro-optic materials are ferroelectric; that is, they exhibit a spontaneous polarization below T_C. The material of greatest importance is La-doped $Pb(Zr_zTi_{(1-z)})O_3$. The phase diagram for PLZT is shown in Fig. 3.32. La^{+3} substitutes on the A site of the perovskite structure in place of Pb^{+2}, acting as an electron donor. Charge neutrality is maintained by the formation of A or B site vacancies. Although the exact lattice configuration is still unknown, experimental results by Hartling et al. have shown that a significant number of lattice vacancies exist when PZT is doped with La. The result is a reduction in the c/a ratio and a drop in the T_C. As T_C is approached in a ferroelectric, the domain structure is more easily realigned, i.e., low coercive fields. PLZT com-

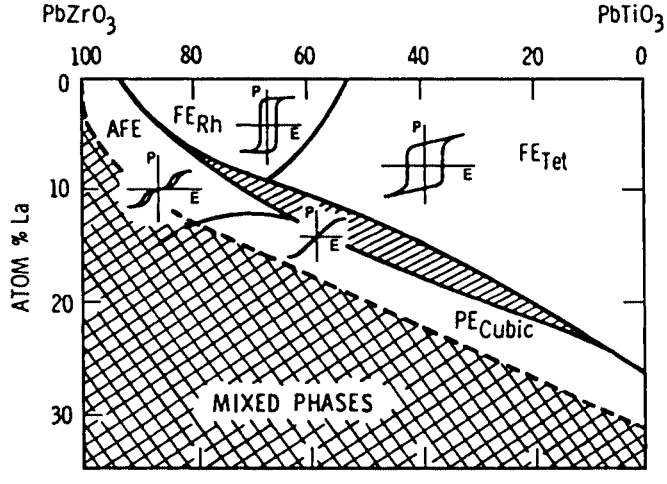

Figure 3.32 Room-temperature phase diagram of the PLZT system illustrating the phases present and typical hysteresis loops associated with each phase.[16]

Downloaded from Digital Engineering Library @ McGraw-Hill (www.digitalengineeringlibrary.com)
Copyright © 2004 The McGraw-Hill Companies. All rights reserved.
Any use is subject to the Terms of Use as given at the website.

positions used in electro-optic applications are nearly cubic, and the c/a ratio is approximately 1.01. Most often, compositions are chosen that lie close to the morphotropic phase boundary between tetragonal and rhombohedral phases where properties are maximized. Compositions on the tetragonal side of the boundary tend to be hard ferroelectrics, i.e., higher coercive fields. Compositions on the rhombohedral side are softer, i.e., lower coercive fields. Table 3.14 shows the electro-optic coefficients for some common electro-optic materials.

TABLE 3.14 Electro-optic Properties of Various Materials

Material (single crystals)	T_C, °C	R, m^2/V^2	R_c, M/V	E_c, kV/cm
$BaTiO_3$	130		19–23	
$LiNbO_3$			17.5	
$LiTaO_3$			22	
2/65/35	320	10^{-16}		13.7
7/65/35	150	10^{-16}		5.3
8/65/35	65	10^{-16}		3.6
8.5/65/35		38.6×10^{-16}		
9/65/35	5	$38. \times 10^{-16}$		0
9.5/65/35	–10	1.5×10^{-16}		0
10/65/35	–25	0.80×10^{-16}		0
11/65/35		0.32×10^{-16}		0
12/65/35		0.16×10^{-16}		0
8/90/10		10^{-16}		0
8/70/30	20	11.7×10^{-16}		0
8/40/60	240		1.0	
8/10/90	355			37.5
12/40/60			1.2	
$Sr_{0.5}Ba_{0.5}Nb_2O_6$			2.10	
$Sr_{0.75}Ba_{0.25}Nb_2O_6$			14.0	
KH_2PO_4			0.52	
$LiNbO_3$			0.17	
$LiTaO_3$			0.22	

Transparency is a key requirement of electro-optic materials. Light scattering will occur at discontinuities such as porosity, phase boundaries, and grain boundaries. The best transmission is usually observed in isotropic materials

Downloaded from Digital Engineering Library @ McGraw-Hill (www.digitalengineeringlibrary.com)
Copyright © 2004 The McGraw-Hill Companies. All rights reserved.
Any use is subject to the Terms of Use as given at the website.

that are single phase, with a high degree of homogeneity, and fully dense. Although the properties of single-crystal electro-optic materials are superior to those of ceramics, polycrystalline ceramics have a number of advantages over single crystals. Process complexity and cost are perhaps the greatest advantages. Single crystals are typically grown from a molten bath and are limited in size. Polycrystalline materials can be formed in large sizes and complex shapes at relatively low cost. To approach the properties of single-crystal specimens, electro-optic ceramics are typically hot-pressed to achieve full densification. Improvements in homogeneity have occurred with the adoption of wet chemistry methods, such as sol-gel and precipitation, for preparation of the ceramic powders.

3.6.1 Applications

Electro-optic behavior falls into three categories: memory, linear, and quadratic. Figure 3.33 shows the characteristic polarization versus field behavior and the change in refractive index with applied field. Devices using the quadratic configuration are based on isotropic compositions with no applied field, such as 8 to 12 percent La additions in $Pb(Zr_{0.65}Ti_{0.35})O_3$. As a field is applied, a ferroelectric-type state is induced. These materials exhibit the quadratic, Kerr, dependence of birefringence on electric field.

Memory characteristic include soft ferroelectric behavior. Compositions exhibiting low coercive forces, <1 MV/m, near the morphotropic phase boundary are typical, such as $Pb(Zr_{0.65}Ti_{0.35})O_3$ doped with <8 percent La. Typically, a large field is applied to achieve a large remnant polarization. Intermediate polarization states can be obtained by applying voltages.

Linear characteristics are achieved by forming compositions that are hard ferroelectrics, i.e., in the tetragonal phase region of PLZT, where the coercive fields are large (≈1.5 to 2 MV/m). Typically, compositions for linear behavior are based on 8 to 12 percent La-doped $Pb(Zr_{0.40}Ti_{0.60})O_3$. To achieve the desired linear characteristics (Pockels behavior), the material first must be poled to achieve high remnant polarization.

Optical shutters utilize the properties of quadratic electro-optic materials as shown in Fig. 3.34. Switching from zero field to the field required for half-wave retardation results in a light shutter. If the electro-optic material is placed between crossed polarizers, polarized light is transmitted through the first polarizer. None of the polarized light is transmitted through the second crossed polarizer at zero applied field. Applying sufficient field causes birefringence and a net rotation of the polarized light by 90°, passing through the second crossed polarizer.

The voltage required to achieve 90° rotation of one wave component relative to the other is given by

$$V = \frac{\lambda t_{field}}{R t_{prop}} \tag{3.17}$$

where λ = wavelength of the incident light

Downloaded from Digital Engineering Library @ McGraw-Hill (www.digitalengineeringlibrary.com)
Copyright © 2004 The McGraw-Hill Companies. All rights reserved.
Any use is subject to the Terms of Use as given at the website.

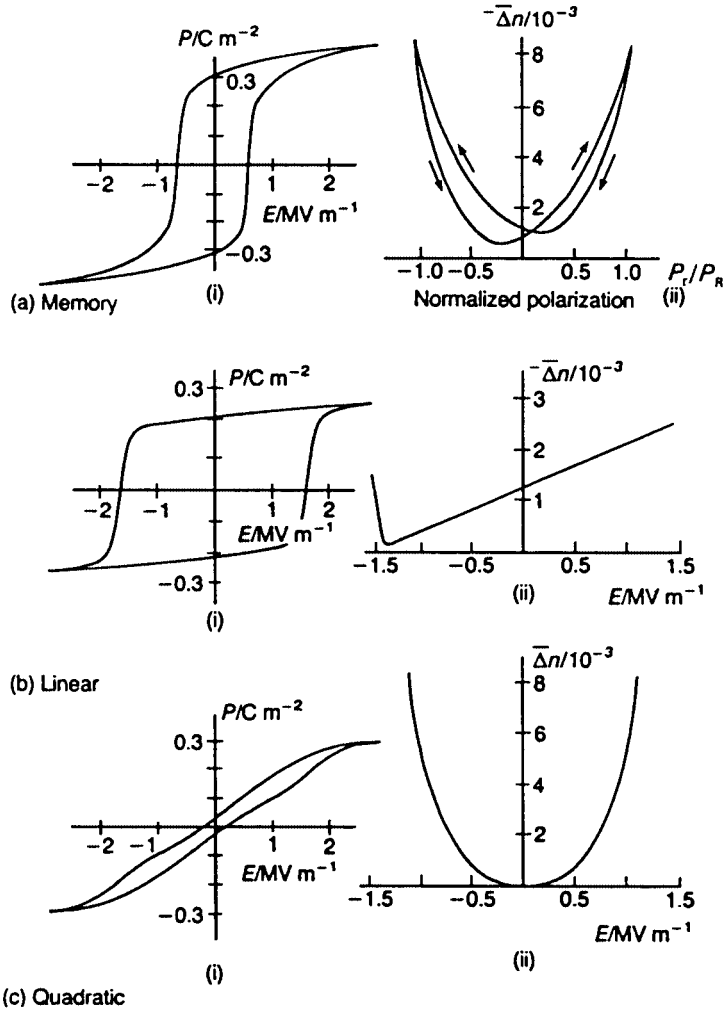

Figure 3.33 Hysteresis and electro-optic characteristics of the three main types of PLZT: *(a)* memory, *(b)* linear, and *(c)* quadratic.[18]

t_{field} = thickness across which an electric field is applied
t_{prop} = propagation distance

The required voltage can be reduced by increasing the electro-optic coefficient, reducing the material thickness in the applied field direction, or increasing the propagation distance.

The ratio of transmitted light to incident light in a cross-polarized light shutter is given by

$$I_t/I_i = \sin 2(\Delta n\pi/\lambda) \tag{3.18}$$

for monochromatic light of wavelength λ.

Downloaded from Digital Engineering Library @ McGraw-Hill (www.digitalengineeringlibrary.com)
Copyright © 2004 The McGraw-Hill Companies. All rights reserved.
Any use is subject to the Terms of Use as given at the website.

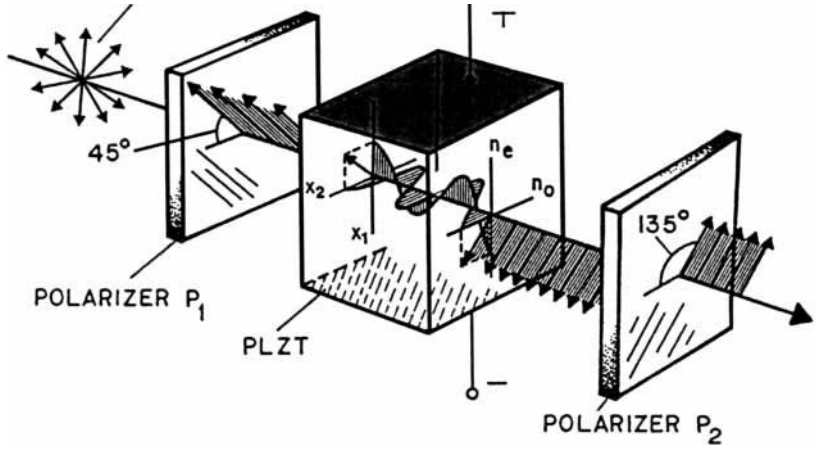

Figure 3.34 Optical phase retardation in an activated PLZT electro-optic ceramic; the open state at half-wave voltage is shown for a crossed-polarizer configuration.[16]

However, when the incident light is white light, there is a retardation of different wavelengths as the electric field is increased. Figure 3.35 shows the Kerr optical interference color chart. It shows transmitted wavelengths and, therefore, colors with applied field for various material birefringence and thickness values.

Electro-optic thin film devices are of two types: one in which the propagation of light is along the plane of the film (optical waveguides), and the other in which the light passes through the film (optical memory and displays). An optical waveguide controls the propagation of light in a transparent material (ferroelectric thin film) along a certain path. For the waveguide to work properly, the refractive index of the film should be higher than that of the substrate. For light to propagate in the waveguide, the thin film should be optically transparent. A great deal of work has been done on making ferroelectric thin film waveguides from $LiNbO_3$ and $Li(Nb,Ta)O_3$ using LPE, EGM, and MBE methods. PZT and PLZT thin films are even better candidates for optical waveguide applications because of their large electro-optic coefficients.

Ferroelectric thin films may replace the use of PLZT bulk ceramics for optical memory and display applications. The advantages offered by thin films for display applications include a simplification of the display device design and lower operating voltages as compared to PLZT ceramic devices. Optical memories using PLZT thin films will also need lower operating voltages.

3.7 Magnetic Ceramics

Magnetic ceramics differ from magnetic metals in that they are oxides that have lower magnetic moments, high resistivities, and a greater dependency of properties on microstructure; some types of magnetic ceramics, ferromagnetic and ferrimagnetic materials, exhibit remnant induction behavior. Magnetite (Fe_3O_4) is a naturally occurring magnetic material (lodestone) that

Downloaded from Digital Engineering Library @ McGraw-Hill (www.digitalengineeringlibrary.com)
Copyright © 2004 The McGraw-Hill Companies. All rights reserved.
Any use is subject to the Terms of Use as given at the website.

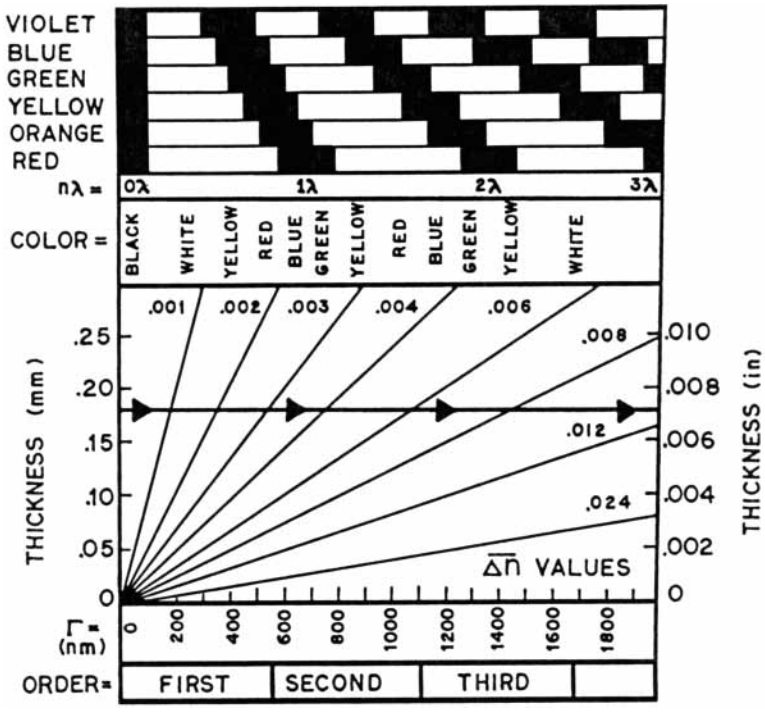

Figure 3.35 A Kerr retardation chart showing the origin of the Newton color orders.[16]

was used as primitive magnets thousands of years ago. Magnetite belongs to the spinel family of minerals, having the general formulation MFe_2O_4, where M is typically a transition metal ion. Other important crystal structures in magnetic ceramics are iron garnets, $M_3Fe_5O_{12}$, and magnetoplumbite, $MFe_{12}O_{19}$.

Investigations into the magnetic properties of various spinels began in the early 1900s (Hilpert). Throughout the 1930s, 1940s, and 1950s, there was increasing interest in developing ferrite materials as magnetic cores. These investigations led to the discovery of ferromagnetism (by Neel) in 1948, permanent magnet hexaferrites in 1951 (by Went), and ferromagnetic behavior in other structures such as orthoferrites and garnets. Magnetic garnets were discovered in the mid-1950s by Bertaut and Forrat. Volume production of Cu-Zn ferrite materials for magnetic core applications began in the 1930s. Applications for ferrite ceramics have expanded with the rapid growth of the electronics industry to include inductors, transformers, permanent magnets, magneto-optical devices, electro-mechanical devices, and microwave electronics devices.

A magnetic moment results from current loops. In a magnetic material, this can result from electrons orbiting atomic nuclei, electrons spinning on their own axes, and nuclei contributions. Nuclear magnetic moments are very small and typically are ignored.

Downloaded from Digital Engineering Library @ McGraw-Hill (www.digitalengineeringlibrary.com)
Copyright © 2004 The McGraw-Hill Companies. All rights reserved.
Any use is subject to the Terms of Use as given at the website.

Ceramics and Glasses

The magnitude of magnetic moment for an orbiting electron is a Bohr magneton,

$$\mu_B = \frac{eh}{4\pi m_e} = \frac{(1.602 \times 10^{-19}\text{C})(6.623 \times 10^{-34}\text{ J/s})}{4\pi(9.109 \times 10^{-31}\text{ kg})}$$

$$= 9.274 \times 10^{-24}\text{ Am}^2\text{/electron } (9.274 \times 10^{-21}\text{ erg/Oe})$$

In most ferrites, the electronic interaction in bonding is such that there is little electron orbital momentum (orbital quenching). The main contribution to magnetic moment is from electron spins that are free to orient with an applied field and that are not cancelled by antiparallel spins on other sublattices. Pauli exclusion principles allow only two electrons to occupy an energy level. These electrons will have opposite spins that cancel their magnetic moments (s = +1/2, s = –1/2). Permanent magnetic moments are found in solids containing ions with unpaired electrons, such as those containing conduction band electrons; an odd number of electrons; or transition, rare-earth, or actinide elements (because of their incompletely filled inner shells). Figure 3.36 shows the order in which electrons fill electron orbitals in an atom or ion. The superscript represents the number of electrons in each orbital. Electrons are oriented in four types of orbitals (s, p, d, and f) for which the space quantum number, l, equals 0, 1, 2, and 3, respectively. The orbital quantum number for all the electrons in an ion is equal the sum of the space quantum numbers, $L = \Sigma l$. The space quantum number is equal to –l, –l+1, –l+2, –l+3, …, +l for the number of electrons in each orbital. The spin quantum number for all the electrons in an ion, S, is equal to Σs. Hund's rules can be used to determine the total magnetic moment for a given atom or ion. Hund's rules state the following:

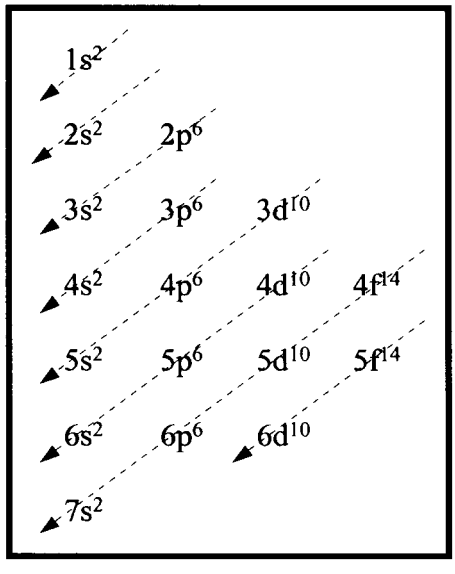

Figure 3.36 The order of electron orbital filling.

Downloaded from Digital Engineering Library @ McGraw-Hill (www.digitalengineeringlibrary.com)
Copyright © 2004 The McGraw-Hill Companies. All rights reserved.
Any use is subject to the Terms of Use as given at the website.

1. The number of unpaired spins is a maximum.
2. The L value is the maximum allowed.
3. $J = |L - S|$ when the shell is less than half filled.
4. $J = |L + S|$ when the shell is more than half filled.
5. $J = S$ when the shell is half filled.

The total magnetic moment for the ion is

$$\mu = 2[J(J + 1)]^{1/2} \mu_B \tag{3.19}$$

This relationship can be used to calculate the magnetic moments of various ions in a solid. Table 3.15 shows the electron configuration of ions in ferrite materials. Notice the unfilled 3d orbital for the transition metal ions.

TABLE 3.15 Electron Configuration of Ferrite Constituent Ions

Ion	Electrons	Electron configuration	Unpaired electrons
O^{2}	10	$1s^2 2s^2 2p^6$	0
Fe^{2+}	24 (23)	$1s^2 2s^2 2p^6 3s^2 3p^6 3d^6 (3d^5)$	4(5)
Mg^{2+}	10	$1s^2 2s^2 2p^6$	0
Al^{3+}	10	$1s^2 2s^2 2p^6$	0
Li^{+}	2	$1s^2$	0
Zn^{2+}	28	$1s^2 2s^2 2p^6 3s^2 3p^6 3d^{10}$	0
Cd^{2+}	46	$1s^2 2s^2 2p^6 3s^2 3p^6 4s^2 4p^6 4d^{10}$	0
Mn^{2+} (Mn^{3+}) (Mn^{4+})	23 (22) (21)	$1s^2 2s^2 2p^6 3s^2 3p^6 3d^5 (3d^4)(3d^3)$	5 (4) (3)
Cr^{2+} (Cr^{3+})	22 (21)	$1s^2 2s^2 p^6 3s^2 3p^6 3d^4 (3d^3)$	4 (3)
Co^{2+} (Co^{3+})	25 (24)	$1s^2 2s^2 p^6 3s^2 3p^6 3d^7$ ($3d^6$)	3 (4)
Ni^{2+}	26	$1s^2 2s^2 p^6 3s^2 3p^6 3d^8$	2
Cu^{+} (Cu^{2+})	28 (27)	$1s^2 2s^2 2p^6 3s^2 3p^6 3d^{10} (3d^9)$	0 (1)

The bulk magnetization, M, can be calculated using the formula

$$M = n \mu_B N_o d / A \tag{3.20}$$

where n = number of unpaired electron spins/atom
N_o = Avagadro's number (6.023×10^{23} atoms/mole)
d = density
A = atomic weight

Downloaded from Digital Engineering Library @ McGraw-Hill (www.digitalengineeringlibrary.com)
Copyright © 2004 The McGraw-Hill Companies. All rights reserved.
Any use is subject to the Terms of Use as given at the website.

Diamagnetic materials have electronic interactions that produce a net-zero magnetic moment. If a magnetic field is applied to these materials, a small magnetic moment is induced that orients opposing the applied field. These materials, which have closed electron shells, have negative susceptibilities on the order of 10^{-5} to 10^{-6}. Diamagnetic materials include most ceramics and metals with a closed electron shell, organics, and inert gases.

Materials containing ions with odd numbers of electrons, such as those from the rare-earth and transition series, possess a net magnetic moment. In the absence of an applied magnetic field, the orientation of these moments is random, with no mutual interaction, resulting in a net-zero magnetism. If a magnetic field is applied, the individual moments tend to align their polarity with the field, creating a net magnetism. Paramagnetic materials have a permanent magnetic moment with a positive but small susceptibility (10^{-3} to 10^{-6}). Thermal energy opposes this effect.

Ferromagnetic materials have large magnetization due to strong magnetic dipole interaction, spontaneously aligning without an applied field in small volumes of material. The magnetic dipole interaction is a result of electron exchange between O^{2-} ions and neighboring Fe^{3+} ions. These small volumes of material with aligned dipoles, Weiss domains, tend to randomly orient to the lowest energy state in the absence of an applied field. However, the net magnetization for the bulk material is zero because of the random orientation of the magnetization vectors between domains. Under applied field, those domains oriented in the direction of the applied field grow at the expense of oppositely oriented or perpendicular domains. The spontaneous magnetization is typically several orders of magnitude greater than the applied field, resulting in very high permeability.

Antiferroelectric materials have an exchange interaction between unpaired electrons, which results in antiparallel alignment of electron spins. The magnetic moments of ions in adjacent planes are equal in magnitude, aligned, but in opposite polarity; therefore, the result is no net magnetization. A few materials, such as FeO, MnO, NiO, and CoO, exhibit this behavior.

It is more common for materials to exhibit antiparallel alignment between two sublattices. These different sublattices have unequal numbers of antiparallel moments, resulting in a net magnetic moment for the crystal. These ferrimagnetic materials (ferrites) are the most broadly used magnetic material group. Both ferromagnetic and ferrimagnetic materials possess Weiss domain regions wherein there is a strong mutual interaction between magnetic moments, and spontaneous magnetization occurs. This spontaneous magnetization occurs along specific crystallographic directions that minimize the free energy of the material. Figure 3.37 shows how the successive breakup of magnetic domains keeps the magnetic flux within the material and lowers the energy level of the material. The boundary between adjacent domains has a finite width (approximately 1 μm) and consists of a gradual change in magnetic moment from one orientation to the other, which minimizes the boundary energy. Figure 3.38 shows the behavior of a ferro- or ferrimagnetic material as a magnetic field is applied. The magnetic moments begin to align with the field; domain boundaries move so that domains aligned with field

Downloaded from Digital Engineering Library @ McGraw-Hill (www.digitalengineeringlibrary.com)
Copyright © 2004 The McGraw-Hill Companies. All rights reserved.
Any use is subject to the Terms of Use as given at the website.

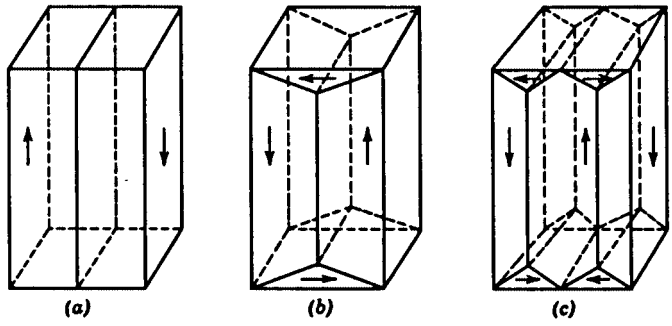

Figure 3.37 Several domain structures of a solid, each having a zero net magnetization but progressively lower energy.[14]

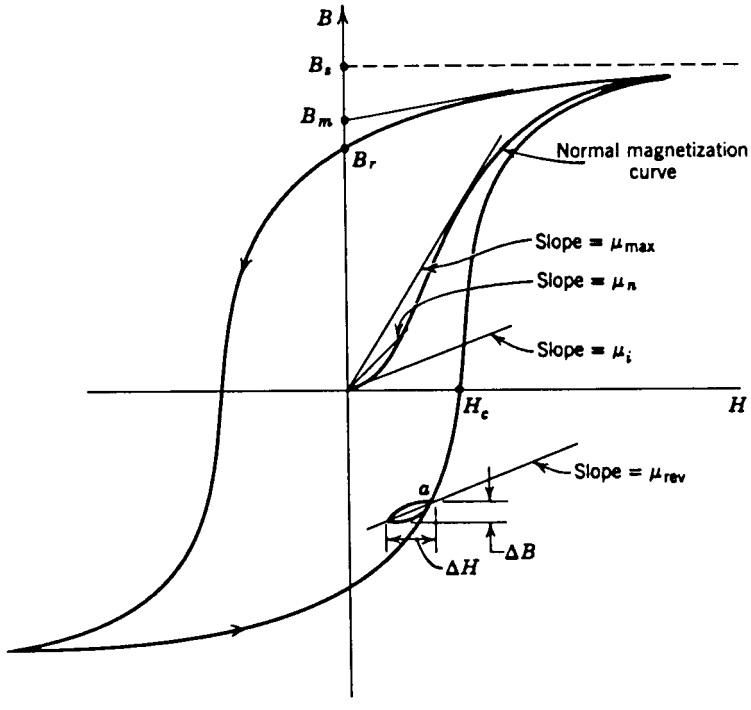

Figure 3.38 Magnetic induction vs. magnetic field for a ferrite.[14]

grow at the expense of others. This alignment results in increased magnetization as higher fields are applied. The ratio of the change in magnetic induction with applied field is the magnetic permeability; that is,

$$\mu = \Delta B/\Delta H \tag{3.21}$$

At high fields, the magnetization reaches saturation, B_s, as nearly all of the material aligns with the field. If the field is removed, a significant portion of

Downloaded from Digital Engineering Library @ McGraw-Hill (www.digitalengineeringlibrary.com)
Copyright © 2004 The McGraw-Hill Companies. All rights reserved.
Any use is subject to the Terms of Use as given at the website.

the domain alignment remains, creating a remnant magnetization (induction), B_r. If a reversed field is applied, the remnant induction is reduced. The field required to completely reverse the induced magnetization is the coercive field, H_c. If a large enough reverse field is applied, the domains will align in the opposite direction and ultimately saturate with reverse polarity. This cyclical behavior, hysteresis, is characteristic of ferro- and ferrimagnetic materials. This nonreversible B-H behavior represents an energy loss, in the form of heat, as a result of moving domain boundaries.

An applied magnetic field on a ferromagnetic material causes alignment of the magnetization vectors in the direction of the field. The magnetization, M, is the magnetic moment per unit volume and has units of tesla (weber/m^2). Analogous to dielectric relationships, the relative permeability, μ_r, can be defined as μ'/μ_o. The magnetic susceptibility, X_m, is defined as the amount of magnetization for an applied magnetic field,

$$X_m = M/H = \mu_r - 1 \tag{3.22}$$

Ferro- and ferrimagnetic materials obey the Curie-Weiss law; that is, magnetization drops as temperature increases as a result of the randomization of magnetic moments caused by the increased thermal energy. At the Curie temperature, spontaneous magnetization goes to zero, and the material becomes paramagnetic.

$$\frac{1}{X_m} = \frac{1}{C(T - T_C)} \tag{3.23}$$

where C = Curie-Weiss constant
T_C = Curie temperature

The resultant magnetic induction (or magnetic flux density), B, as a result of a current loop on a nonmagnetic material is $B = \mu_o\, nI$, where μ_o is the magnetic permeability of vacuum, $4\pi \times 10^{-7}$H/m (1 G/Oe), n is the number of turns, and I is the current. If a coil is wound on magnetic material, amperian currents result (I_a) from electron orbits and spin; this results in an additional contribution to the magnetic induction. The total magnetic induction (magnetic flux density) on a magnetic material is the sum of the magnetization and the external magnetic field.

$$B = \mu_o\, nI + \mu_o\, I_a = \mu_o(H + M) = \mu_o(H + X_m H) = \mu_o\, \mu_r H = \mu' H \tag{3.24}$$

where μ = permeability of the material

When an external field is applied to a ferrite shape, the material aligns to oppose the applied field, and magnetic poles are formed at the surfaces. The shape of the ferrite determines the magnitude of the field within the material. This internal field, H_i, is related to the applied field H_a and the demagnetizing field, H_D by

Downloaded from Digital Engineering Library @ McGraw-Hill (www.digitalengineeringlibrary.com)
Copyright © 2004 The McGraw-Hill Companies. All rights reserved.
Any use is subject to the Terms of Use as given at the website.

$$H_i = H_a - H_D = H_a - N_D M \tag{3.25}$$

where N_D = demagnetizing factor dependent on the device shape
M = magnetization

If a uniform sphere of material is assumed, N_D is equal to 1/3, and the magnetic induction and will equal 4π; then,

$$B = H + 4\pi M \tag{3.26}$$

Typically, the total induction is expressed with the field subtracted out to equal $4\pi M_s$. In materials wherein saturation can be reached at relatively low fields, the saturation induction is equal to $4\pi M_s$. Therefore, the total magnetic induction in a material is given by

$$B = H + 4\pi M_s \tag{3.27}$$

In soft ferrites, the peak induction approaches the $4\pi M_s$ value. Ferrites have lower saturation magnetization and higher resistivities than magnetic metals, primarily because of the amount of large, nonmagnetic oxygen ions.

Magnetic field strength and flux density are measured in terms of Gauss or Oersteds. 1 Oe = 79.7 A/m. 1 G = 10^{-4} Weber/m^2. One Weber/m^2 = 1 tesla = 796 emu/cm^3. Permeability is given in terms of henry/m or erg/Oe. The elementary unit of magnetic moment, the Bohr magneton, μ_B, is 9.27×10^{-24} Am^2/electron = 9.27×10^{-21} erg/G.

3.7.1 Spinels

Spinels have the general chemical formula MFe_2O_4. The unit cell of the spinel crystal structure is composed of eight formula units, with the oxygen ions forming a cubic close-packed array as shown in Fig. 3.39. The oxygen array contains 64 tetrahedral (A sites) and 32 larger octahedral (B sites) coordinated interstices. Eight of the tetrahedral A sites and 16 of the octahedral B sites are filled; that is, 1 tetrahedral and 2 octahedral sites per formula unit are filled. The electronic spins of the ions on the A and B sites (and, therefore, their magnetic moments) are set up in opposing directions, antiferroelectric. In normal spinel, such as $MgFe_2O_4$, $CdFe_2O_4$, and $ZnFe_2O_4$, divalent ions occupy all eight of the available A sites, and trivalent Fe ions occupy the available B sites and have the chemical formula of $(M^{2+}O)Fe^{3+}{}_2O_3$. The tetrahedral site is smaller (0.55 to 0.67 Å) than the octahedral site (0.72 to 0.78Å) and can more readily accommodate the smaller trivalent ions.

In inverse spinels, such as Fe_3O_4 and $CoFe_2O_4$, all of the A sites and half of the available B sites are filled with trivalent ions; the remaining eight B sites are occupied by divalent ions and have a chemical formula of $Fe^{3+}(Fe^{3+}M^{2+})O_4$. The O^{2-} ions have a full 2p shell; the six electrons pair off with opposing spins that cannot contribute to a magnetic moment. Each Fe^{3+} ion has five unpaired 3d shell electrons whose spins are parallel and can contribute to a magnetic moment. In these antiferromagnetic materials, the unpaired

Downloaded from Digital Engineering Library @ McGraw-Hill (www.digitalengineeringlibrary.com)
Copyright © 2004 The McGraw-Hill Companies. All rights reserved.
Any use is subject to the Terms of Use as given at the website.

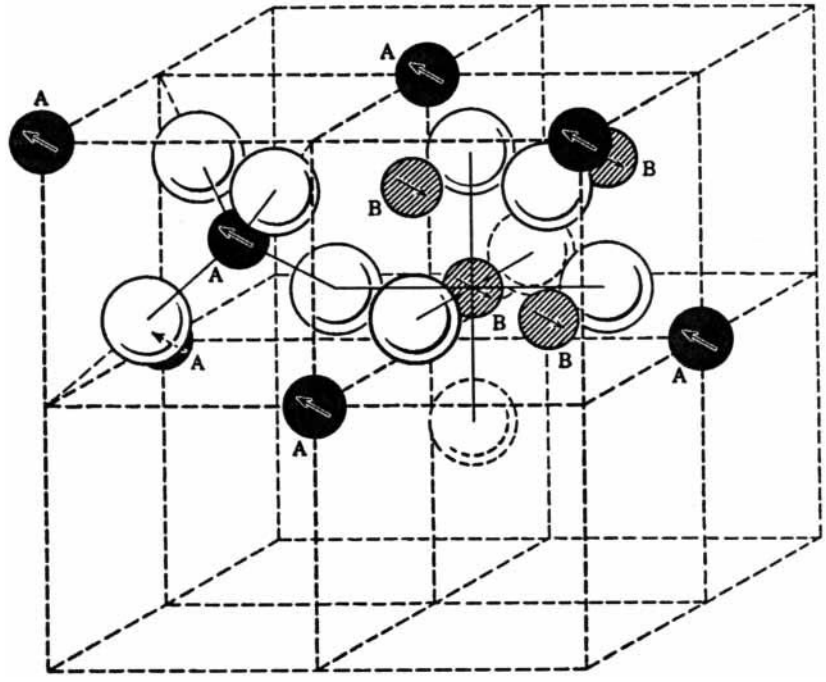

Figure 3.39 The crystal structure of spinel, AB_2O_4.[14]

electronic spins of the trivalent ions (Fe^{3+}) on A site ions are antiparallel to those on the B site, canceling their magnetic moments. The net moment is a result of the remaining eight divalent ions on the B site. In $NiFe_2O_4$, the Fe^{+3} ions on the A site align antiparallel to those on the B site and mutually cancel. The net moment is the result of the remaining Ni^{+2} ions on the B site.

For a divalent M ion from the transition series with n electrons in the d shell, the magnetic moment for the ferrite is:

$$\mu_m = n\mu_B \text{ if } n < 6 \text{ or } (10 - n)\mu_B \text{ if } n > 5 \tag{3.28}$$

All of the metal atoms in the A and B sites will orient in the minimum energy configuration. Some ferrite formulations result in structures that are not fully inverse or normal, depending on the metal ion size, heat treatment, and atmosphere. If x is the fraction of divalent ions on the B site, then

$$\mu_m \text{ (A site)} = (1 - x)n\mu_B + \times 5\ \mu_B \tag{3.29}$$

$$\mu_m \text{ (B site)} = (1 - x)5\mu_B + 5 + xn\ \mu_B \tag{3.30}$$

$$\mu_m \text{ (net)} = \mu_m\text{(A site)} - \mu_m\text{(B site)} \tag{3.31}$$

Manganese ferrite is about 80 percent normal spinel and is not influenced much by heat treatment. Nickel ferrite is about 80 percent inverse and also is

Downloaded from Digital Engineering Library @ McGraw-Hill (www.digitalengineeringlibrary.com)
Copyright © 2004 The McGraw-Hill Companies. All rights reserved.
Any use is subject to the Terms of Use as given at the website.

not affected by heat treatment. In general, ferrites shift to the normal structure at higher temperatures. Magnesium and copper ferrite are normal spinel at high temperature; if quenched, the normal spinel structure is retained. If slow cooled, the spinel transforms to the inverse spinel structure.

Lithium ferrite, $Li_{0.5}Fe_{2.5}O_4$, requires an excess of Fe^{+3} ions to maintain charge balance with Li^+. Four of the 16 occupied octahedral sites are filled by Li^+. Gamma ferric oxide, γ-Fe_2O_3, is a special case of the spinel structure containing no divalent ions. For charge balance, only two-thirds of the normally occupied octahedral sites are filled with Fe^{3+}. This leads to an imbalance in the magnetic spins on the A and B sites, resulting in a net magnetic moment. Table 3.16 shows the magnetic moments for various ferrites calculated in this manor versus measured values. The differences are primarily the result of variability in ion location form the prediction, minor contributions from orbital momentum, and spin directions not being perfectly parallel. Table 3.17 shows the range of properties for ferrite materials.

TABLE 3.16 Measured vs. Calculated Values for Magnetic Moments of Ferrites

	Density, g/cm^3	T_C, °C	μ_m	M_z	B_5
$FeFe_2O_4$	5.24	585	4	480	6000
$ZnFe_2O_4$	5.33	N/A	0		
$MgFe_2O_4$	4.52	440	0	110	1500
$NiFe_2O_4$	5.38	585	2	270	3400
$CuFe_2O_4$	5.42	455	1	135	1700
$Li_{0.5}Fe_{2.5}O_4$	4.75	670	2.5	310	3900
$MnFe_2O_4$	5.00		5	400	6000
$CoFe_2O_4$	5.29	520	3	425	5300

Zinc substitutions for magnetic divalent ions can be used to raise the magnetic moment of the material. Zn^{2+} ions enter the tetrahedral A sites with no magnetic moment to orient antiparallel to the B site moments. The result is a larger uncanceled moment from the B site that contributes to the net magnetic moment. Figure 3.40 shows the measured effect of Zn additions to various ferrites.

Because Fe^{+3} and Mn^{+2} have the highest magnetic contribution of any ion, 5 μ_B, they have the highest potential contribution to the magnetization of a ferrite. Applications wherein the highest magnetic moments are needed typically contain Mn^{2+} or uncompensated Fe^{+3} additions. The magnetostriction coefficient for ferrous ferrite is positive, so additions of Fe^{+3} ions also reduce the magnitude of electrostriction in most ferrites. Replacing some of the Mn^{+2} ions

Downloaded from Digital Engineering Library @ McGraw-Hill (www.digitalengineeringlibrary.com)
Copyright © 2004 The McGraw-Hill Companies. All rights reserved.
Any use is subject to the Terms of Use as given at the website.

TABLE 3.17 Properties of Commercially Available Microwave Ferrites[*10]

Major composition	Saturation magnetization, $4\pi M_s$, G	Curie temp., T_C, K	Resonance line width, ΔH, Oe	Lande g factor	Coercive force, H_c, Oe	Dielectric constant, ε	Dielectric loss factor, tan δ_ε	Dielectric density, g/cm^3
Y	1800	575	60					
Y	1780	555	45	2.00			<0.00025	5.06
Y	1780	555	55	2.01	0.75	16.0	<0.00025	
Y	1750	555	60	2.0		15	0.0005	
Y	1750	555	35	2.01		16.3		5.08
Y	1750	550	50			16.2	0.0005	
Y	1740	550	60	2.0				5.1
YGd	1600	540	60	2.0	1.1	16.0	<0.00025	
YAl	1540	550	50			14.8	0.0005	
YGd	1520	555	55	2.01			<0.00025	5.26
YAl	1470	525	40	2.01			<0.00025	5.04
YGd	1300	555	70	2.03			<0.00025	5.42
YAl	1220	515	55			14.6	0.0005	
YGd	1220	525	100	2.0		15	0.0005	
YGd	1200	555	85	2.00	0.75	15	<0.00025	
YAl	1200	535	60	1.99	0.5	15.5	<0.00025	
YGdAl	1200	525	55			14.8	0.0005	
YAl	1150	500	60	2.0				5.0
YAl	1120	485	40	2.01			<0.00025	5.03
YGd	1000	555	130	2.05			<0.00025	5.68
YGd	1000	555	120	2.00	0.8	15.5	<0.00025	
YAl	1000	525	60	1.99	1.2	15.0	<0.00025	
YAl	990	485	55			14.4	0.0005	
YAl	850	455	40	2.01			<0.00025	5.00
YGd	850	555	160	2.00	1.0	15.5	<0.00025	
YGd	840	525	200	2.0		15	0.0005	
YAl	800	505	65	2.00	1.2	15.0	<0.00025	
YGdAl	800	525	110			15.0	0.0005	

Downloaded from Digital Engineering Library @ McGraw-Hill (www.digitalengineeringlibrary.com)
Copyright © 2004 The McGraw-Hill Companies. All rights reserved.
Any use is subject to the Terms of Use as given at the website.

TABLE 3.17 Properties of Commercially Available Microwave Ferrites[*10] *(Continued)*

Major composition	Saturation magnetization, $4\pi M_s$, G	Curie temp., T_C, K	Resonance line width, ΔH, Oe	Lande g factor	Coercive force, H_c, Oe	Dielectric constant, ε	Dielectric loss factor, tan δ_ε	Dielectric density, g/cm^3
YGdAl	750	525	80			15.0	0.0005	
YGd	750	555	200	2.08			<0.00025	5.85
YGd	725	555	220	2.03	1.0	15.5	<0.0005	
YAl	680	475	70	2.00	1.2	15.0	<0.00025	
YAl	680	455	45	2.00	1.0	14.5	<0.00025	
YGdAl	675	475	120	2.0				5.1
YGdAl	660	525	210	2.05			<0.00025	5.73
YAl	650	445	40	2.02			<0.00025	5.00
YAl	600	430	60	2.0		15	0.0005	
YAl	600	445	40			14.3	0.0005	
YAl	550	435	75	2.00	1.2	14.0	<0.00025	
YAl	475	430	50			14.0	0.0004	
YAl	400	405	45	2.01	1.0	14.0	<0.00025	
YAl	400	405	45			13.8	0.0005	
YAl	370	400	40			14.0	0.0005	
YGdAl	340	475	310	2.10			<0.00025	5.63
YAl	300	400	40	2.02	0.4	14.0	<0.00025	
YAl	290	390	40			13.4	0.0005	
YAl	240	370	40	2.03	1.0	14.0	<0.00025	
YAl	225	380	35			13.8	0.0004	
			Nickel ferrites					
NiZn	5000	650	135	2.08	0.9	12.5	0.001	
Ni	3000	850	350	2.3				5.1
NiCo	3000	860	350	2.21	12	13.0	0.0025	
NiCo	3000	865	200	2.2		13	0.0005	
Ni	3000	865	500	3.3		12	0.0005	
NiCoAl	2440	826	260	2.33			<0.0005	5.05
NiTiAl	2200	825	500	2.45		12.0	0.002	4.80

Downloaded from Digital Engineering Library @ McGraw-Hill (www.digitalengineeringlibrary.com)
Copyright © 2004 The McGraw-Hill Companies. All rights reserved.
Any use is subject to the Terms of Use as given at the website.

Ceramics and Glasses

TABLE 3.17 Properties of Commercially Available Microwave Ferrites[*10] *(Continued)*

Major composition	Saturation magnetization, $4\pi M_s$, G	Curie temp., T_C, K	Resonance line width, ΔH, Oe	Lande g factor	Coercive force, H_c, Oe	Dielectric constant, ε	Dielectric loss factor, tan δ_ε	Dielectric density, g/cm^3
NiAl	2000	835	450	2.31	4	12.8	0.001	
NiCoAl	1800	820	1000	2.55	36	9.0	0.0015	
NiCoAl	1800	775	800	2.55	21	9.5	0.002	
			Magnesium ferrites					
MgMn	2220	585	500	2.07			<0.00025	4.20
MgMn	2150	595	540	2.10	2.5	13.0	<0.00025	
MgMn	2100	575	425	2.0		12	0.0005	
MgMn	2000	555	350	2.0				4.3
MgMn	2000	575	400	2.07		12	0.0008	4.3
MgMn	1950	515	150	2.0				4.3
MgMn	1780	595	380	2.06	1.4	12	0.0005	4.15
MgMnAl	1760	565	490	2.11	2.1	12	0.0005	4.10
MgMnAl	1700	500	225	2.00	1.0	12.0	<0.00025	
MgMn	1650	575	650	2.0				4.3
MgMnAl	1550	515	375	2.0				4.3
MgMnAl	1250	439	155	2.00	0.4	11.5	<0.00025	
MgMnAl	1250	475	300	2.0				4.2
MgMnAl	1140	425	165	0.02				4.10
MgMnAl	1110	415	220	2.04	0.8	12	0.0003	3.95
MgMnAl	730	375	120	2.00	0.7	12	0.0004	3.90
MgMnAl	680	375	120	2.02	1.2	11.5	<0.00025	

[*]Measurements made at X band.

SOURCE: *Handbook of Microwave Ferrite Materials,* W. H. von Aulock, Ed., © Academic Press, Orlando, FL, l965, pp. xviii–xxi.

in $MnFe_2O_3$ with Fe^{+3} ions has the effect of reducing the magnetic anisotropy to zero, raises the permeability, and decreases the resistivity. Additions of Co in most ferrites have the effect of making anisotropy more positive. Co is also added to improve power handling in ferrites.

Zn substitution in Mn and Ni ferrites increases the magnetic moments but also reduces the Curie temperatures, resulting in lower saturation induction values. Zinc additions also lowers magnetostriction and magnetocrystalline

Downloaded from Digital Engineering Library @ McGraw-Hill (www.digitalengineeringlibrary.com)
Copyright © 2004 The McGraw-Hill Companies. All rights reserved.
Any use is subject to the Terms of Use as given at the website.

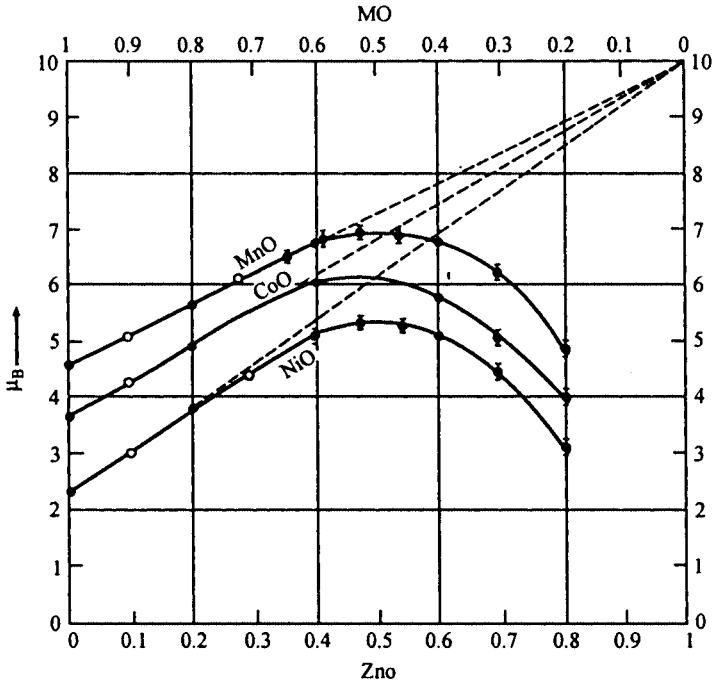

Figure 3.40 Effect of zinc substitution on magnetic moments of various ferrites.[10]

anisotropy. Most commercial ferrites are solid solutions of different ferrites, mixed ferrites, to optimize the properties for a particular application. $NiFe_2O_4$ and $MgFe_2O_4$ have lower magnetic moments but higher resistivities that are well suited for high-frequency applications.

3.7.2 Garnets

Garnets have the general structure $M_3Fe_5O_{12}$, $(3M_2O_3)(2Fe_2O_3)(3Fe_2O3)$, where M is a trivalent rare-earth or yttrium ion. The crystal structure is cubic, containing eight formula units per unit cell (Fig. 3.41). The oxygen array forms 24 tetrahedral (D site), 16 octahedral (A site), and 16 dodecahedral (C site) coordination interstices per unit cell. The $Fe3^+$ ions occupying the tetrahedral are aligned antiparallel to the A and C sites. The net magnetic moment per unit cell is given by

$$\mu_m(\text{net}) = \mu_m(\text{A site}) + \mu_m\ (\text{C site}) - \mu_m\ (\text{D site}) \tag{3.32}$$

The rare-earth ions are large and therefore occupy the large dodecahedral sites. Because there are three D site Fe^{3+} for each two A site Fe^{3+} and three C site M^{3+} ions, and the moment for each Fe^{3+} ion is 5 μ_B, the equation shortens to

Downloaded from Digital Engineering Library @ McGraw-Hill (www.digitalengineeringlibrary.com)
Copyright © 2004 The McGraw-Hill Companies. All rights reserved.
Any use is subject to the Terms of Use as given at the website.

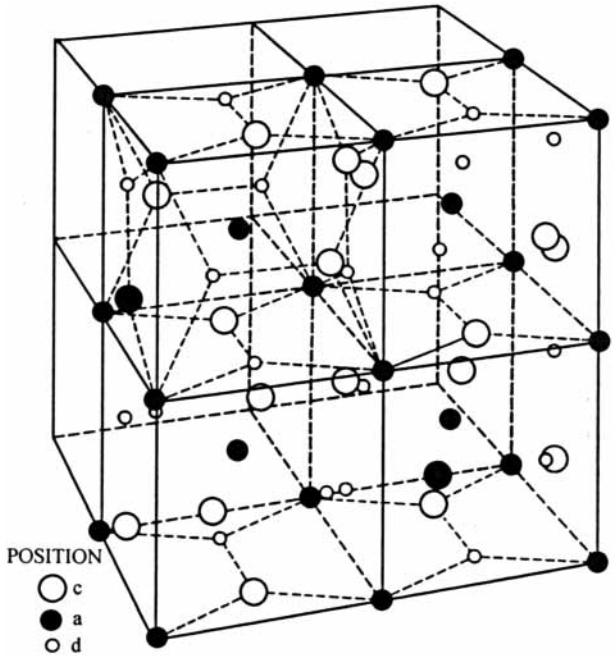

Figure 3.41 Unit cell of a rare-earth garnet.[10]

$$\mu_m \text{ (net)} = 2\mu_m(2\text{Fe}_A^{3+}) + 3\mu_m(2M_C^{3+}) - 3\mu_m(2\text{Fe}_D^{3+})$$

$$= 3\mu_m(2M_C^{3+}) - 10\ \mu_B \tag{3.33}$$

The Y^{3+} ion has no magnetic moment, because it has no unpaired spins (i.e., $4s^2 4p^6$), so the magnetic moment is due to the Fe^{3+} ions only. The rare-earth ions have unpaired 4f electrons that contribute to the magnetic moment. However, estimating the magnetic moment for garnets in this manor has some error caused by an electron spin-orbital coupling. This is the result of the 4f orbital surrounding full 5s, 5p, and 5d orbitals.

Substitutions are sometimes made for the Fe^{3+} ions to modify the properties of a garnet. Smaller ions, such as Al^{3+}, will occupy the smaller tetrahedral sites. This decreases the moment of the tetrahedral site and therefore the net moment of the garnet. Larger ions, such as In^{3+} and Sc^{3+}, occupy the larger octahedral sites. Again, these substitutions will decrease the moment for the site; however, the difference in the moment between the octahedral and tetrahedral sites is greater. These substitutions result in a higher net moment for the crystal.

3.7.3 Perovskites

The general formula for perovskite ferrites is $MFeO_3$ where M is a rare-earth or Y^{3+}, La^{3+}, Ca^{2+}, Sr^{2+}, or Ba^{2+} ion. The crystal structure is orthorhombic

Downloaded from Digital Engineering Library @ McGraw-Hill (www.digitalengineeringlibrary.com)
Copyright © 2004 The McGraw-Hill Companies. All rights reserved.
Any use is subject to the Terms of Use as given at the website.

with face-centered oxygen ions; thus the name *orthoferrites*. The A and B site moments are aligned antiparallel; however, there is a slight canting, leading to a small net magnetic moment.

3.7.4 Hexagonal ferrites

Hexagonal ferrites have the general formula $MFe_{12}O_{19}$ where M is Ba^{2+}, Sr^{2+}, or Pb^{2+}. The crystal structure for magnetoplumbite consists of a hexagonal close-packed array of oxygen ions with two formula units per unit cell. The oxygen layers contain the M^{2+} ions, which can substitute for oxygen sites. The unit cell consists of ten O^{2-} layers with M^{2+} replacing O^{2-} on every fifth layer. Two layers contain M^{2+} ions, four layers contain four O^{2-} ions (one layer of three O^{2-} with one M^{2+}), four layers containing all O^{2-} ions, and one layer containing three O^{2-} with one M^{2+}. The Fe^{3+} ions occupy two tetragonal sites, nine octahedral sites, and one five-coordination site. All of the tetragonal sites and two of the octahedral sites are aligned antiparallel to the remaining sites. The leaves four sites wherein the moment are not cancelled by antiparallel alignment. The net moment is $4 \times 5\mu_B$ (Fe^{3+}).

Hexagonal ferrite is used as a permanent magnet due to high magnetocrystalline anisotropy and high coercive fields. The easy direction of magnetization is the c axis.

3.7.5 Applications

Phase shifters are the enabling component for electronically scanned array radars (ESAs). In this application, a time delay in an RF signal is achieved by propagating through a magnetized waveguide or TEM through conductors embedded in the magnetic material. The degree of phase shift is controlled by varying the current applied to coil loops around the magnetic materials.

Magnetic garnets can be epitaxially grown in thin film form on nonmagnetic substrates. CTE differences result in a preferred magnetization direction perpendicular to the substrate. Magnetic domains form with spins up and spins down. These domains appear as bubbles in polarized light. These bubble domains provide binary inputs for digital computers (bubble memory).

3.8 Superconductive Ceramics

The phenomenon of superconductivity was discovered in 1911 by K. Onnes, in mercury metal, shortly after his development of a process for forming liquid helium. He found that resistance dropped sharply to near zero at a temperature of 4.2 K (–269°C). Later, the development of liquid helium enabled the discover of superconductivity in many compounds, because it allows the cooling of materials to near absolute zero (1 K) temperature. Meissner, in 1933, showed that superconductors exhibit not only zero electrical resistance but also diamagnetic behavior. Diamagnetic materials have electronic interactions that produce a net-zero magnetic moment. If a magnetic field is applied

Downloaded from Digital Engineering Library @ McGraw-Hill (www.digitalengineeringlibrary.com)
Copyright © 2004 The McGraw-Hill Companies. All rights reserved.
Any use is subject to the Terms of Use as given at the website.

Ceramics and Glasses

to these materials, a magnetic moment is induced that orients in opposition to the applied field. These materials, which typically have closed electron shells, have negative magnetic susceptibilities on the order of 10^5 to 10^6. The generation of the opposing magnetic field is the driving force for the high surface current (screening current) flow in the material.

When a magnetic field is applied to a superconductor below T_c, electric currents flow in the material without resistance, creating a magnetic field opposing the applied field—the Meissner effect. There is a critical current density, J_c, above which superconduction halts. The electric current density is a measure of the charge moving through an area of material over a given time.

$$J = nze\nu \tag{3.34}$$

where n = number of charged particles per unit volume
e = electronic charge
z = valence (in the case of ionic conduction)
ν = drift velocity in units of cm/s

The ratio of the drift velocity to the local electric field, ν/E, is defined as the charge mobility, μ, in units of cm^2/Vs.

Electrical conductivity, σ, is a measure of the current density, J, with an applied electric field, E.

$$\sigma = J/E = nze(\nu/E) = nze\mu$$

There is a maximum magnetic field, H_c, above which superconduction ceases. In general, as the temperature is raised to T_C, J_C, and H_C decrease as shown in Fig. 3.42 for Nb_3Sn. The desirable properties of a superconducting material are a high T_C, a high critical current density, a high critical magnetic field (H_c), low cost, reliability, and manufacturability.

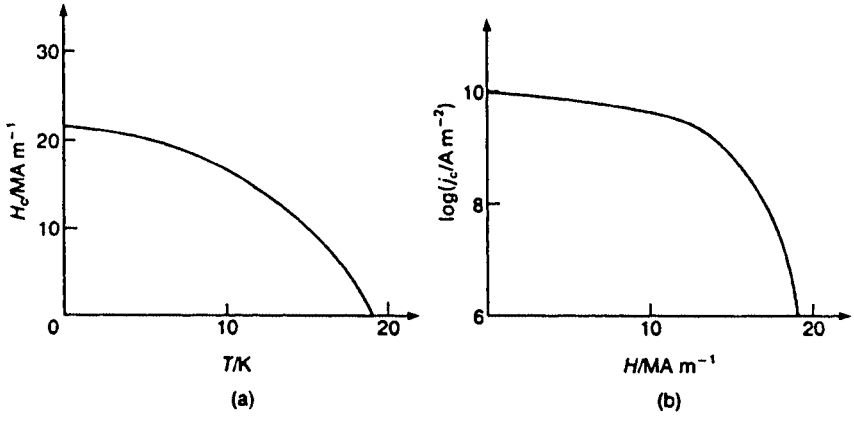

Figure 3.42 *(a)* Critical magnetic field, H_C, as a function of temperature for Nb_3Sn, and *(b)* critical current density, J_C, as a function of magnetic field at 4.2 K for Nb_3Sn.[24]

Downloaded from Digital Engineering Library @ McGraw-Hill (www.digitalengineeringlibrary.com)
Copyright © 2004 The McGraw-Hill Companies. All rights reserved.
Any use is subject to the Terms of Use as given at the website.

In Type I superconductors, all magnetic flux is contained in a surface layer of the material—the *London penetration depth*. Metallic superconductors are Type I. In Type II superconductors, magnetic flux penetrates the interior of the material at a critical magnetic field. If the flux lines are not pinned, there is resistive energy loss, and the current density at which the magnetic flux moves into the interior determines J_C. If the flux lines are pinned along controlled crystalline defects, such as impurity inclusions or second phases, higher magnetic fields can be tolerated, leading to higher current density. The high-temperature superconductor (HTS) ceramics are Type II and are capable of withstanding much higher magnetic fields.

In the 1950s, Frohlich and Bardeen theorized that superconduction is a result of electron-phonon interactions that couple electron pairs. This pairing up can occur only at low temperatures where thermally induced motions of the electrons are sufficiently reduced. Later, L.N. Cooper showed how an electron pair, a *Cooper pair,* would have an combined energy level lower than conduction electrons in the highest energy state (the *Fermi level*). In 1957, J. Bardeen, L.N. Cooper, and J.R. Schrieffer further theorized the large-scale interaction of Cooper pairs, resulting in the *BCS theory.* The BCS theory describes how electron pairs in a superconducting metal interact such that their combined momenta is unchanged. Conduction scattering mechanisms, such as phonon interactions, have equal and opposite effects on each of the paired electrons. Therefore, there is no change in momentum and no resistance to the conduction of electron pairs. In 1950, B.T. Matthias attempted to establish criteria for good superconductors. Material requirements included a high concentration of Fermi-level electrons, the presence of soft phonons, and the proximity to a metal-insulator transition.

The quest for a room-temperature superconductor has spurred the development of thousands of compounds incrementally driving the critical temperature for superconduction to higher values. Table 3.18 shows various superconducting materials with their corresponding transitions temperatures below which the resistivity falls to infinitesimal levels. At present, the highest temperature for the onset of superconductivity is ≈130 K.

In 1966, the first superconducting ceramic was discovered in the perovskite structure $SrTiO_{3-x}$ with a T_c of 0.5 K. The oxygen deficiency results in lattice vacancies that aid in the conduction—n-type conduction. Johnson et al., in 1973, documented the superconducting behavior of $Li_{1+x}Ti_{2-x}O_4$ ($0 < x < 1/3$) at ≈14 K. In 1986, J.G. Bednorz and K.A. Muller received the Nobel prize for their discovery of the superconducting behavior of perovskite-like $La_{2-x}Ba_xCuO_{4-y}$ with a T_c of 35 K. The crystal structure consists of layers of perovskite formed by Cu-O separated by layers of rock-salt crystal structure formed by La, Ba-O ions. Their data, shown in Fig. 3.43a, sparked a significant amount of research in cuprate superconductors wherein Cu^{2+} and Cu^{3+} can coexist. Soon thereafter, Wu and Chu discovered compositions of $YBa_2Cu_3O_{7-x}$, the 123-cuprate material shown in Fig. 3.43b, with a transition temperature well above the 77 K boiling point of nitrogen, at ≈93 K. Superconductors that operate above liquid nitrogen temperatures enable the fabrication of practical devices that are cooled by much cheaper liquid N_2. These 123-cuprates are of

Downloaded from Digital Engineering Library @ McGraw-Hill (www.digitalengineeringlibrary.com)
Copyright © 2004 The McGraw-Hill Companies. All rights reserved.
Any use is subject to the Terms of Use as given at the website.

TABLE 3.18 Transition Temperatures for Superconducting Materials

Element/compound	T_C (K)
$SrTiO_{3-x}$	0.5
Sn	3.7
Hg	4.2
Pb	7.2
Nb	9.2
$BaPb_{1-x}Bi_xO_3$ ($x \approx 0.25$)	13
$Li_{1+x}Ti_{2-x}O_4$ ($0 < x < 1/3$)	14
Nb_3Sn	18
$Nb_3Al_{0.5}Ge_{0.2}$	20.9
Nb_3Ge	23
$Nd_{2-x}Ce_xCuO_4$	
BaKBiO	30
$La_{2-x}Ba_xCuO_{4-y}$	35
PbSrCaLaCuO	55
$YBa_2Cu_3O_{7-x}$	93
$Bi_2Sr_2Ca_2Cu_3O_x$	110
$Bi_{1.5}Pb_{0.5}Sr_2Ca_2Cu_3O_x$	110
BiAlCaSrCuO	114
TiCaBaCuO	100–125
$HgBa_2Ca_2Cu_3O_8$	133 (150–160 pressurized)

the layered perovskite-type crystal structure shown in Fig. 3.44. Again, the superconducting behavior results from the existence of multivalence copper ions mixed with oxygen ions forming planar arrays separated by perovskite layers. The perovskite structure favors the existence of soft-mode phonons, as evident by its instability and morphotropic phase boundaries—one of the Matthias' criteria. The presence of multivalence ions and oxygen vacancies seams to favor superconductivity. The Cu-O distance is dependent on the oxidation state of the copper. Therefore, as an electron is transferred, the oxidation state of the copper changes, resulting in a lattice displacement. This is theorized to be the mechanism for the electron-phonon interaction described in the BCS theory.

Downloaded from Digital Engineering Library @ McGraw-Hill (www.digitalengineeringlibrary.com)
Copyright © 2004 The McGraw-Hill Companies. All rights reserved.
Any use is subject to the Terms of Use as given at the website.

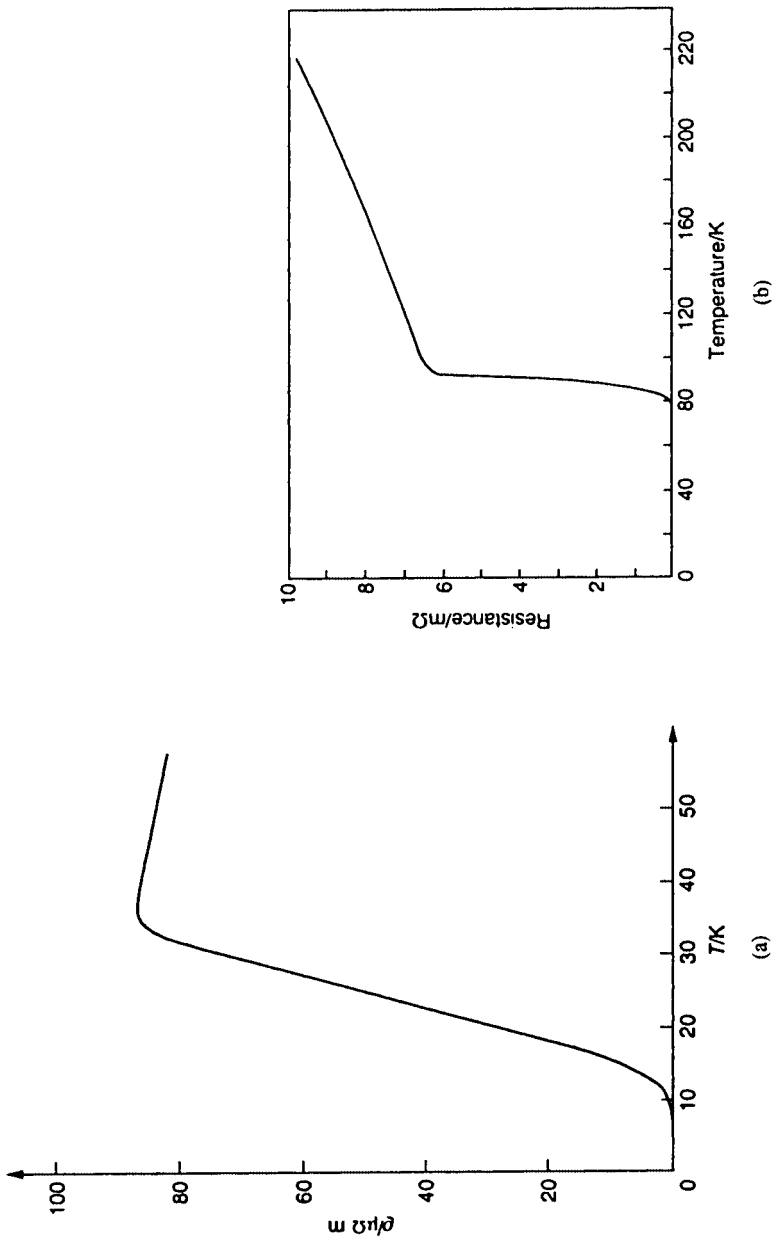

Figure 3.43 (*a*) Superconductivity in $(La,BA)_2CuO_4$ and (*b*) $YBa_2Cu3O_{7-\delta}$.[18]

Downloaded from Digital Engineering Library @ McGraw-Hill (www.digitalengineeringlibrary.com)
Copyright © 2004 The McGraw-Hill Companies. All rights reserved.
Any use is subject to the Terms of Use as given at the website.

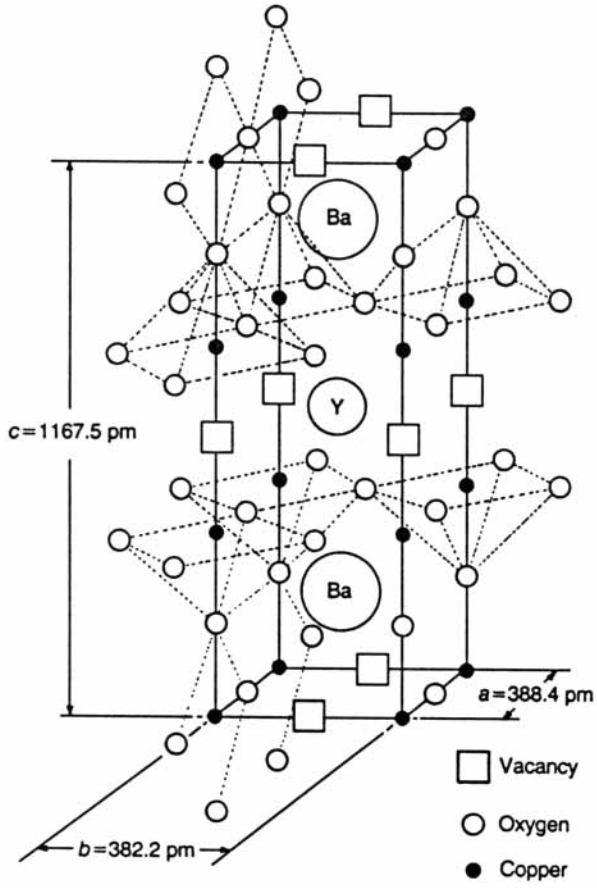

Figure 3.44 123-cuprate layered perovskite structure.[18]

In 1988, Maeda et al. discovered superconducting phases in the Bi-Sr-Ca-Cu-O system. Similarly, Sheng and Hermann discovered high T_C in the Ti-Ba-Ca-Cu-O system. The compounds contain Cu-O sheets interleaved with Ti-O or Bi-O sheets. The Bi-Sr-Ca-Cu-O system has three superconducting phases, $(BiO)_2Sr_2Ca_{n-1}$ $CunO_{2n+2}$, where n = 1, 2, 3. Their respective critical temperatures are 7 K, 80 K, and 110 K. Deficiencies on any of the cation sites, creating hole conduction, have been found to significantly increase the critical current density. Figure 3.45 shows the change in conductivity as a function of oxygen atmosphere during processing for a 123-cuprate superconductor. In 1993, a series of mercury-based compounds were discovered with high critical temperatures has sparked new level of interest. The layered structure of $HgBa_2Ca_2Cu_3O_8$ has been shown to have a T_c of approximately 130 K, or 164 K under high-pressure conditions.

Fabrication of these materials in large volumes with homogeneous phase and consistent properties has been a primary focus of superconductor research. Low critical current density, J_C, and poor mechanical properties have

Downloaded from Digital Engineering Library @ McGraw-Hill (www.digitalengineeringlibrary.com)
Copyright © 2004 The McGraw-Hill Companies. All rights reserved.
Any use is subject to the Terms of Use as given at the website.

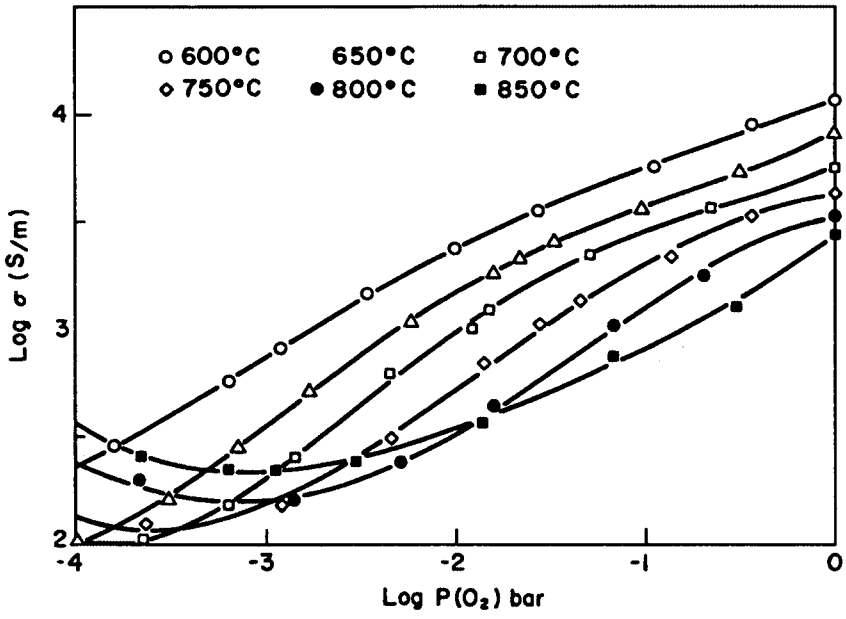

Figure 3.45 The equilibrium conductivity of $YBa_2Cu_3O_x$ as a function of oxygen activity in the temperature range of 600 to 850°C.[19]

been the key problem areas. For most superconducting applications, a J_C of 10^5 to 10^6 A/cm^2 is required. The J_C of polycrystalline ceramics is generally much lower than that single crystals as a result of high-resistivity phases, microcracks, and changes in crystal orientation at the grain boundaries. Polycrystalline materials with J_C as high as 5×10^3 A/cm^2 have been reported.

The highest-current-density materials have been fabricated in single-crystal or thin film forms. Critical current densities greater than 10^6 A/cm^2 have been achieved in single crystals and epitaxially grown thin films. Oak Ridge National Laboratory (ORNL) has demonstrated a Y-Ba-Cu-O coated conductor with the ability to produce 1 to 2 cm long, 0.3 cm wide conductors with critical current densities up to 3×10^6 A/cm^2 at 77 K. Midwest Superconductivity Inc. (MSI) has produced high J_C results using MOCVD for Y-Ba-Cu-O deposition on a substrate produced by ORNL, resulting in a short sample with J_C of 6.4×10^5 A/cm^2.

The properties of ceramic superconductors are highly dependent on the concentration of charge carriers. Therefore, the properties are determined by the phase purity, crystal structure, composition, and defect structure of the material. The final oxidation state of these oxide superconductors is critical to achieving maximum performance and maximize T_c. Most device fabrications include an anneal in oxidizing atmospheres. A significant amount of research is focused on processing methodologies, final chemistry, and phase relations so as to achieve the desirable phase stability and purity. Polycrystalline ceramic superconductors are typically prepared by solid state calcination of oxide, nitrate, or carbonate precursors. Multiple milling steps are incorporated to

Downloaded from Digital Engineering Library @ McGraw-Hill (www.digitalengineeringlibrary.com)
Copyright © 2004 The McGraw-Hill Companies. All rights reserved.
Any use is subject to the Terms of Use as given at the website.

promote homogeneity. Chemical synthesis routes using organometallic salts and metal alkoxide precursors such as sol-gel, precipitation, and decomposition processing have also been used to achieve a high degree of homogeneity. For thin film superconductors, a variety of processes have had some degree of success, including chemical vapor deposition (CVD), spin coating, plasma spraying, molecular beam epitaxy, magnetron sputtering, laser ablation, and laser evaporation.

Grain-orienting processing techniques have been used to achieve anisotropic single-crystal behavior in polycrystalline ceramics. Current flows more easily perpendicular to the C axis of the crystals; therefore, a larger J_C and low onset resistivity is observed. Hot forging is a process similar to hot pressing; however, the material is unconstrained in the plane of the platens. The material is forced to densify or deform under a constant strain. Manufacturers of superconducting devices continue to strive for practical methods of forming useful superconducting circuits. The simple fact that the high-temperature superconductors are ceramic is a significant obstacle to forming wiring. However, processes such as plastic extrusion and tape casting are being used to fabricate superconducting coils. Polycrystalline wire formed by placing 123-cuprate in silver metal tubing is used to achieve current densities in the range of 2 to 3×10^3 A/cm^2.

3.8.1 Applications of superconductors

Superconductor materials are finding an increase in the number of applications. Most applications fall into one of three categories of functions: low-loss transmission electronics, high-magnetic-field generation, or high-current-carrying conductors for power delivery. Up to 15 percent of electrical power is lost through transmission line resistance between the power source and the end user. Superconducting transmission wires have the potential to eliminate this energy loss. The high current densities attained with superconducting coils enable the generation of large magnetic fields. Large magnetic field generation is required in medical diagnostic equipment, particle accelerators in nuclear energy research, and fusion containment magnets. Nuclear magnetic resonance (NMR) and magnetic resonance imaging (MRI) equipment uses superconductors for generation of the large magnetic fields used in these imaging systems. Efficient superconducting magnets are used to create magnetic fields as high as 20T. No-loss electrical transmission and high-speed signal processing have generated interest in the area of digital processing. Because of the diamagnetic behavior of the superconducting materials, the Meissner effect, they are being used in magnetic field shielding applications. Superconductors allow fabrication of highly efficient motors and generators. Magnetic levitation for efficient high-speed trains is now a possibility.

A a superconducting quantum interference device (SQUID) is a superconducting instrument that is capable of detecting minute changes in magnetic fields. SQUID sensors can detect weak magnetic fields, as low as 10^{-15} T. SQUID sensors have medical applications whereby magnetic fields resulting from electrical currents flowing in the human brain can be detected. Other ap-

Downloaded from Digital Engineering Library @ McGraw-Hill (www.digitalengineeringlibrary.com)
Copyright © 2004 The McGraw-Hill Companies. All rights reserved.
Any use is subject to the Terms of Use as given at the website.

plications include geological research and military applications such as submarine detection.

In 1962, B.D. Josephson predicted that the Cooper pairs in superconductors could tunnel through a 10-insulating barrier with no electrical resistance—the Josephson effect. A Josephson junction allows current to flow with no resistance with no applied field. However, at a critical voltage level, the Cooper pairs split up, and normal quantum-mechanical tunneling occurs with resistive losses. This effect enables the fabrication of microelectronic switches and transistors that operate faster and with lower power loss than semiconductor devices.

An example of high current transmission lines is shown in Fig. 3.46: the high-current transmission line fabricated by American Superconductor Corporation. This power transmission cable consists of HTS wires wound around a hollow core through which liquid nitrogen flows for cooling below T_C. The conductor is surrounded by conventional dielectric insulation. The efficiency of this design reduces losses. The cryogenic dielectric is a coaxial configuration comprising an HTS conductor cooled by liquid nitrogen flowing through a flexible hollow core and an HTS return conductor, providing even greater amp capacity, further reducing losses and entirely eliminating the need for dielectric fluids.

Motors and generators using HTS windings have twice the efficiency of conventional copper wire motors. Major motor applications include pumps, fans, and compressors as well as in the handling and processing of manufactured materials. According to the Department of Energy, this energy accounts for 70 percent of all the energy consumed by the manufacturing sector and over 55 percent of the total electric energy generated in this country.

Conductus Inc. fabricates high-performance RF filters and filter subsystems based on HTS technology for the telecommunications market. The ClearSite® line of front-end receiver subsystems for cellular and PCS base stations manu-

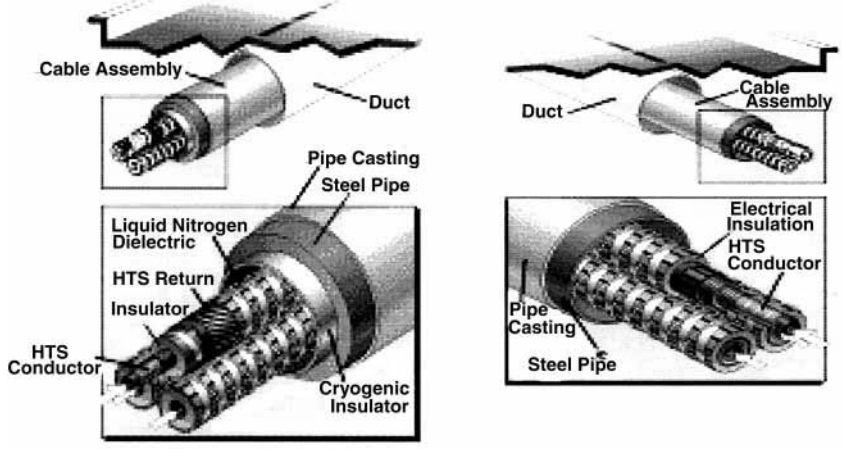

Figure 3.46 High-current transmission line from American Superconductor Corp.[1]

Downloaded from Digital Engineering Library @ McGraw-Hill (www.digitalengineeringlibrary.com)
Copyright © 2004 The McGraw-Hill Companies. All rights reserved.
Any use is subject to the Terms of Use as given at the website.

Ceramics and Glasses

factured by Conductus contains microwave filters with as many as 19 poles, made from thin film HTS superconductors. Conventional filters are significantly larger than HTS filters, more inefficient, and limited to no more than nine poles, limiting the filtering capability. Conductus products are based primarily on YBaCuO thin films synthesized through sputtering, pulsed laser deposition, and co-evaporation.

IGC-Advanced Superconductors manufactures superconductive wire, cable, and tape used in MRI diagnostic systems, high-energy physics, and fusion power research. Products are based on NbTi, Nb3Sn, BSCCO 2212/Ag, and BSCCO 2223/Ag multifilament wire and tape.

Superconductor Technologies Inc. (STI) manufactures SuperFilter® Systems based on thin film superconductor receiver filters for use in wireless base stations.

3.9 Optical Fibers

3.9.1 Optical fiber basics

Today, most long-distance telecommunication occurs through optical fibers wherein data is transmitted via light through a glass rather than electrons through a metal fiber. Optical fibers carry information at higher frequencies and, therefore, higher speed and volume without the electromagnetic interference issues associated with metal wiring. The transmission of data through the use light rather than electrons or radio waves has had a dramatic impact on the capacity of telecommunication transmissions. The higher the transmission frequency, the higher the rate of data transmission. Communication at light frequencies was enabled be the advent of high-quality silica-based fibers that are capable of transmission of data over long distances with low attenuation.

Alexander Graham Bell patented an optical telephone system, the Photophone, in 1880. Throughout the early 1900s, a variety of discoveries were based on the idea of total internal reflection to transmit light through water, quartz rods, and Plexiglas® rods. The phenomenon of total internal reflection can confine light in a material surrounded by other materials with lower refractive index, such as glass in air.

Because the fibers were bare, light could be refracted outside the fiber, and the transmission was poor. In the 1960s, researchers found that cladding the fiber core with a material of higher refractive index dramatically improved its transmission. Snell's law for the critical angle for internal reflection is

$$n_1 sin\Theta_1 = n_2 \sin Q_2$$

where n_1 and n_2 are the refractive index of the core and cladding, respectively. The critical incident angle is the minimum angle at which incident light will not be refracted into the cladding material; i.e., the refraction angle is 90°, and $\sin\Theta_2$ is 1. The critical incident angle is $\sin^{-1}(n_2/n_1)$. Pure silica glass has a refractive index of 1.46. The typical difference in refractive index between the core and cladding is ≈0.005.

Downloaded from Digital Engineering Library @ McGraw-Hill (www.digitalengineeringlibrary.com)
Copyright © 2004 The McGraw-Hill Companies. All rights reserved.
Any use is subject to the Terms of Use as given at the website.

The maximum launch angle is called the *acceptance angle*. If light enters the core at angles greater than the acceptance angle, a portion will be refracted into the cladding and result in attenuation of the signal. The *numerical aperture* (NA) is the square root of ($n_{12} - n_{22}$). Light entering at an angle greater than the NA will be refracted into the cladding. Typically, only a 0.4 percent difference in refractive indices is sufficient to achieve an adequate numerical aperture.

By 1960, the state of the art was approximately 1 dB loss per meter of fiber. This was adequate for medical applications using high-power lasers but much to lossy for consideration in communications. During the 1960s, the laser was invented, and there were significant advances in fiber technology. During this time, it was found that a substantial portion of the attenuation was the result of impurities in the glass fibers and that smaller diameter fibers allowed transmission of single-mode light. In 1970, researchers at Corning Glass designed and produced the first optical fiber with optical losses low enough to enable use in telecommunications. These early fibers had a goal of less than 20 dB loss per kilometer (<99 percent loss).

The impurity problems were solved by depositing fused quartz from the vapor phase using a cylindrical preform. In the mid 1970s, processes were refined to improve attenuation, and fibers with a refractive index gradient were developed for transmission of broader-band information—multimode fibers. The gradient is created through doping of the fiber with elements such as B, F, Er, or Ge to modify the refractive index. Multimode fibers carry multiple light rays or modes concurrently, each at a slightly different reflection angle within the optical fiber core. Multiple modes tend to disperse over long distances. Reducing the core diameter reduces multimode distortions. Single-mode fiber typically has a much smaller core (1 to 5 μm) than the multimode (≈100 μm) and is used for long-distance transmission.

The first field test for telephone communication was done in 1977 using 850-nm wavelength light. In the early 1980s, the first undersea cable was developed using 1300-nm wavelength light in single-mode fiber. The attenuation was at a level of approximately 0.5dB/km. Typically, 600- to 1600-nm wavelength (visible and far infrared) signals are launched from laser or light emitting diodes and modulated to encode information.

Repeaters receive the optical signal, remove unwanted noise, amplify the signal, and retransmits it along the next segment. A repeater consists of a photocell, an amplifier, and a light emitting diode (LED) or infrared emitting diode (IRED).

Attenuation is the result of the absorption of light and secondary reradiation in different directions—Rayleigh scattering. This may be caused by inhomogeneities in the glass fiber. Intrinsic absorption of UV is the result of strong transition bonds in silica. Absorption may also occur because of impurities, transition metal ions, and residual OH^- ions. The light is reradiated at different wavelengths, causing attenuation at those wavelengths. Absorption of IR light (>1600 nm) causes atomic vibrations and a loss of energy as heat. For Ultraviolet transmission (λ = 300 to 400 nm), pure silica cores are necessary. Silica has transmission of >90 percent from 300 to 1800 nm. However, less

Downloaded from Digital Engineering Library @ McGraw-Hill (www.digitalengineeringlibrary.com)
Copyright © 2004 The McGraw-Hill Companies. All rights reserved.
Any use is subject to the Terms of Use as given at the website.

expensive glasses may be used in visible (400 to 700 nm) and infrared (700 to 2000 nm).

Corning and Lucent control 70 percent of the $9 billion fiber market. The best fibers currently in development can handle 1.5 trillion bps. In March, 2002, Lucent Technologies' Bell Labs set a new fiber optic transmission record of 40 Gb/sec per channel transmitted over 64 channels over a distance of 4000 km. One gigabit of data is the equivalent of 1000 novels.

References

1. American Superconductor Corporation.
2. Argentina, G.M., Baba, P.D., "Microwave Lithium Ferrites: An Overview," *IEEE Transactions on Microwave Theory and Techniques,* Vol. MTT-22, No. 6, June 1974, pp. 652–658.
3. ASM International Handbook Committee, *Ceramics and Glasses,* Vol. 4, Materials Park, OH, ASM International, 1991.
4. AVX Corporation product catalog, Tantalum Capacitors, p. 6.
5. Buchanan, R.C., *Ceramic Materials for Electronics,* New York, Marcel Dekker, 1986.
6. Burdic, W.S., *Underwater Acoustic Systems Analysis,* Englewood Cliffs, NJ, Prentice Hall, 1984.
7. Clark, D.E., Wayne R. Tinga, Joseph R. Laia, Jr. (Eds.), *Microwaves: Theory and Application in Materials Processing II,* Vol. 36, The American Ceramic Society, Westerville, OH, 1993.
8. Garrou, P.E., I. Turlik, *Multichip Module Technology Handbook,* McGraw-Hill, New York, 1998.
9. Ghate, B.B., J.J. Simmons (Eds.), *Magnet Ceramics,* Vol. 47, The American Ceramic Society, Westerville, OH, 1994.
10. Goldman, A., *Modern Ferrite Technology,* Van Nostrand Reinhold, New York, 1990.
11. Harper, C.A. (Ed), *Electronic Packaging and Interconnection Handbook,* 2nd ed., McGraw-Hill, New York 1997.
12. Harper, C.A., and Ronald N. Sampson (Eds.), *Electronic Materials and Processes Handbook.* 2nd ed. McGraw-Hill, New York, 1994.
13. Jaffe, B., W.R. Cook, Jr., H. Jaffe, *Piezoelectric Ceramics,* Academic Press, New York, 1971.
14. Kingery, W.D., H.K. Bowen, D.R. Uhlmann, *Introduction to Ceramics,* 2nd ed., John Wiley & Sons, New York, 1976.
15. Kulke, R., Simon W., Gunner, C., Mollenbeck, G., Kother, D., Rittweger, M., "RF-Benchmark up to 40 GHz for various LTCC Low Loss Tapes," IMST GmbH, IMAPS-Nordic, Stockholm, 2002.
16. Levinson, L.M. (Ed.), *Electronic Ceramics: Properties, Devices and Applications,* Marcel Decker, New York, 1988.
17. The Materials Information Society, *Ceramics and Glasses,* Vol.4, Materials Park, OH, ASM International, 1991.
18. Moulson, A.J., Herbert, J. M., *Electroceramics: Materials, Properties, Applications,* Chapman & Hall, New York, 1996.
19. Nair, K.M., Giess, E.A. (Eds.), *Superconductivity and Ceramic Transducers,* Vol. 13, The American Ceramic Society, Westerville, OH, 1991.
20. Nair, K.M., R. Pohanka, R.C. Buchanan (Eds.), *Materials and Processes for MicroElectronic Systems,* Vol. 15, The American Ceramic Society, Westerville, OH, 1990.
21. Newnham, R.E., Ruschau, G.R., "Smart Materials," *Earth & Mineral Sciences,* Penn State Univ., Vol. 60, pp. 27–31.
22. Ritter, A P., Bailey, A.E., Poppe, F., and Galvagni, J., "Fabrication of Multilayer Ceramic Actuators," *Active Materials and Adaptive Structures,* IOP Publishing Ltd., 1992, pp. 693–696.

Downloaded from Digital Engineering Library @ McGraw-Hill (www.digitalengineeringlibrary.com)
Copyright © 2004 The McGraw-Hill Companies. All rights reserved.
Any use is subject to the Terms of Use as given at the website.

Downloaded from Digital Engineering Library @ McGraw-Hill (www.digitalengineeringlibrary.com)
Copyright © 2004 The McGraw-Hill Companies. All rights reserved.
Any use is subject to the Terms of Use as given at the website.